Imperial College London

Simulation of the Mechanical and Flow Behaviour of Bone Fixation Implants

Ziyu Zhang

A thesis submitted in fulfilment of requirements for the degree of Doctor of Philosophy

August 2013

Department of Materials
Imperial College London

-Dedicated to my loving parents-

Declaration

I hereby certify that the work presented in this thesis, except where otherwise stated, is the result of my own investigations carried out at Imperial College London during the period from October 2009 to April 2013.

Ziyu Zhang

August 2013

Abstract

Titanium (Ti) porous foams produced by additive manufacturing (AM) techniques are promising for fixation devices in orthopaedic applications. These implants should possess sufficient permeability to allow vascular invasion, integration with the host tissue and also satisfy the transport requirements of remodelling bone. The mechanical properties of implants should also match those of the host tissue to ensure sufficient life span in the body. Both macro and micro-structures of implants influence the mechanical and flow properties. Techniques are therefore needed to characterise the structural parameters and to evaluate their effects on the performance of the implant.

This thesis focuses on computational modelling tools based on X-ray microtomography (μCT) images to characterise the flow and mechanical properties of porous foams. The aim of the study is to develop and apply these tools on Ti implants with different structures to investigate how the design variables offered by AM technique can be used to alter the implant architecture on multiple length scales to control and tailor the flow and mechanical properties.

A computational fluid dynamics model was developed to predict permeability of the implant and how AM can be used to tailor implant flow properties by controlling surface roughness at a microstructual level (microns), and by altering the strut connectivity and density at a macroscopic level (millimetre).

A finite element (FE) model of compression test was developed to quantify mechanical properties of the porous implant based on three-dimensional (3D) μCT images and the work is validated and compared to the *in situ* experiment using μCT.

Fluid flow in bone tissue has a key role in the bone remodelling process. A 3D microscale numerical model that simulates the fluid flow-induced shear stress and time dependant bone growth was developed and showed the inter-relationship between those two dynamic factors.

Acknowledgements

First and foremost, I would like to express my utmost thanks to my supervisors Dr Julian R. Jones and Professor Peter D. Lee, for their inspiring ideas, expert advice and continuous caring support ever since my very first day in the Department of Materials at Imperial College. Their invaluable guidance and encouragement has always been the driving force for me to complete this PhD project. Their passion for work and life has been, and always will be an inspiration for me.

I would like to acknowledge my collaborators at University of Liverpool, Stryker Orthopaedics and the Manchester Imaging Facility at Rutherford Appleton Laboratory. In particular, I feel very grateful to Dr Eric Jones from Stryker, who has always been extremely supportive, for providing me the opportunity to be involved in this PhD project. I would also like to thank Drs Dan Jones and Christopher J. Sutcliffe from Liverpool for providing the samples, experiment data for this project and their professional knowledge and experiences during discussions. Also, I would like to thank Stryker Orthopaedics, EPSRC (EP/I02249X/1) and Department of Materials, Imperial College for their financial support.

I would like to express gratitude to my PhD viva examiners, Dr Ruth Wilcox and Dr Stephen Neethling, for their time and valuable comments.

It has been a great pleasure to work with the members of both Peter and Julian's research teams. I sincerely express thanks towards Dr Sheng Yue and Richard Hamilton for their kindest help on μCT scanning, image processing and quantification methods. I would especially like to thank Drs Pavel Ramirez Lopez, Farid Tariq, Sobhan Abolghasemi and Randhir Singh, for so gracefully introducing me the CFD and FEM methods at the beginning of my PhD. Special and inestimable thanks to Dr Lang Yuan, who has generously shared his knowledge to help and guide me to complete the bone ingrowth chapter. Lastly I would like to thank all my office friends, especially Chedtha, Taek Bo, Kristina, Sophia, Jine Sung, David, Gowsh, Ning and Gladys, for being wonderful friends and making memories that I will cherish for a life time.

Finally, I would like to thank my loving parents, without whom I would never be able to come this far.

Table of Contents

List of Figures

List of Tables

1 Introduction

Osteoarthritis of the knee is degeneration of cartilage caused by injury, obesity, wear and tear. It leads to pain and stiffness of the joint, restricting activities of patients. Around 8 million people in the UK are affected by it and knee joint replacement operations are often needed to improve the quality of life (Van Manen *et al.* 2012). Total knee replacement (TKR) is widely performed as a cost-effective treatment of osteoarthritis in knees. Though TKR has been well recognised as a successful surgical way to treat osteoarthritis, implant failure after TKR is a common problem, which can result in revision operation (Kurtz *et al.* 2005). Therefore, research on improving the life-span of implants in the body is continuously drawing attention in this field.

Figure 1-1 shows a schematic of a human knee joint with TKR implant. The fixation problem of artificial patella component to the patella has been considered as one of most common cases of implant failure in TKR (Ayers *et al.* 1997). The fixation method has been moved from conventional mechanical fixation (with cement and screws) to biological / morphological fixation. The latter involves the use of porous foams which are expected to provide better fixation to the host tissue by stimulating bone ingrowth.

Porous metallic implants are common choices for orthopaedic applications (Geetha *et al.* 2009). This thesis is based on a TKR component to which the project contributed to its commercialisation (FDA approval 2013). Porous titanium (Ti) foams demonstrate good mechanical properties and highly corrosion resistant materials properties in the body. However, understanding of how macro / micro-structures of the foam relates to the overall performance of the implant remains a challenge. To design the optimal structure for implant applications, optimising key structural parameters such as pore / interconnect sizes, strut connectivity and strut surface morphology are crucial, and it is very important to correlate them to the flow transport and mechanical behaviour of the implant. Therefore, characterisation of the porous structure and understanding the relationship between design parameters and implant function is of great importance.

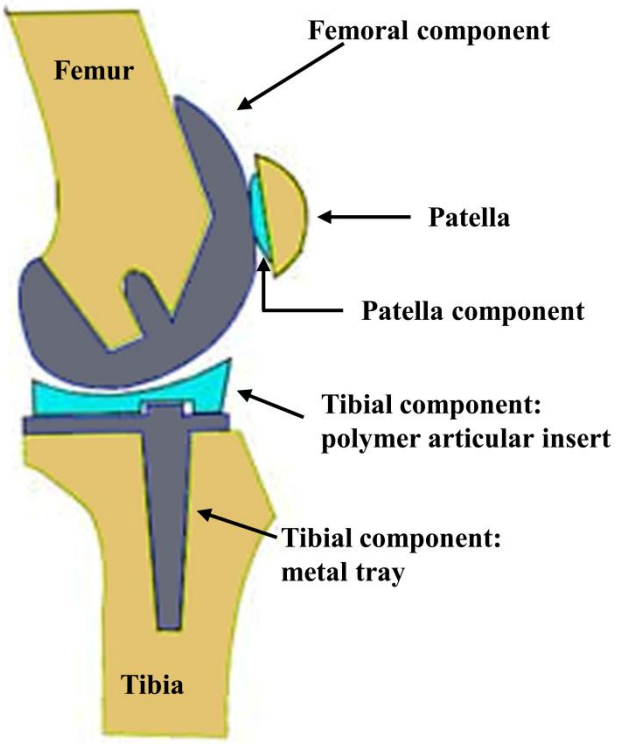

Figure 1-1 Schematic of a human knee joint (lateral view) with TKR implant. (Figure modified from http://www.orthopale.com/total-knee-arthroplasty.php (Cazenave, 2008))

The main objectives of this thesis are to:

1. Develop models based on X-ray microtomography (µCT) images to characterise the mechanical and flow behaviour of porous Ti structures.
2. Model the influence of foam macro/micro-structures on rate of bone ingrowth.

The chapters are organised as follows:

Chapter 2 describes the background and the motivation of this research. Previous literature on TKR, porous Ti foams, three-dimensional (3D) µCT imaging, studies on flow and mechanical properties and bone ingrowth models are reviewed.

Chapter 3 presents the computational fluid dynamics (CFD) based method developed to quantify the permeability of the additive manufactured (AM) Ti implants. The model is applied on various Ti structures to demonstrate its viability as a tool to evaluate the influence of design parameters such as overall porosity, strut morphology and surface roughness on the flow property of the implant. The ability to control the permeability of implants by hierarchically tailoring their structural parameters at both micro and macroscopic levels is presented.

In Chapter 4, a 3D finite element analysis (FEA) model is reported to characterise the compressive behaviour of the implant. The model is validated against *in situ* experiments performed in conjunction with μCT imaging. Direct observation of foam elastic behaviour and strut failure is presented and failure mechanism proposed. Three types of Ti foams with different structural design were used to study the relationship between foam microstructure and mechanical properties.

The importance of fluid flow inside the implant to bone remodelling is discussed in Chapter 5, with the study of how localised fluid flow-induced shear stress affects the bone ingrowth within AM Ti implants. A 3D CFD model is presented to simulate the body fluid flow within the foam structure and quantify bone ingrowth as a function of local flow shear stress. Two types of Ti foam structures are compared together with the description of the inter-relationship between flow-induced shear stress and time dependant bone ingrowth at the microscopic level.

Chapter 6 presents the final conclusions from this thesis and suggestions for future work.

2 Literature Review

Porous metal materials have been widely used in orthopaedic implant applications acting as scaffolds to augment damaged bone. The primary function of the pores is to allow bone ingrowth and integration. The scaffold's properties associated with the structural design are being continuously investigated in the research field. The focus of this thesis is to computationally model the mechanical and the flow behaviour of porous commercially pure titanium (CP-Ti) implants designed as a bone fixation component of a device for total knee replacement (TKR). In this chapter, studies in the literature relating to the TKR operation, the design criteria of implants and the choice of using Ti as the implant material are reviewed. Using non-destructive three-dimensional (3D) X-ray microtomography (μCT) imaging technique as a viable tool for modelling is also reviewed. Finally, reviews of previous studies on numerical simulations of fluid flow, bone remodelling and compression test are presented.

2.1 Bone Fixation

2.1.1 Total Knee Replacement (TKR)

Osteoarthritis is one of the common musculoskeletal diseases (Kramer *et al.* 2005). It occurs when the cartilage on the gliding surface of the knee begins to degenerate, which causes intense pain and stiffness in the knee joint as bone on bone contact occurs. Total knee replacement (TKR) is an efficacious treatment for osteoarthritis of the knee, which can substantially reduce patients' pain and restores movement (Dixon *et al.* 2004). Due to the growing size of the ageing population with many younger patients in need of surgery due to trauma, the need of TKR is continuously increasing (Grotle *et al.* 2008; Mullen *et al.* 2010).

Although TKR is recognised as a successful operation, the rate of revision operations required by patients is growing quickly (Kurtz *et al.* 2005). A large number of these revision operations are needed because of the failure of implant fixation. Common reasons for failure includes implant wear, loosening and instability problems (Sharkey *et al.* 2002). Implants used in TKR operations consist of an articular element coupled with an element that fixes the implant to the native tissue (Mullen *et al.* 2009). The knee

joint prosthesis consists of three main parts (please refer to Figure 1-1). The femoral component (usually made of metal) is fixed to the distal part of the femoral condyle. The metal tibial component (usually made of two parts: a metal tray attached directly to the bone and a polymer articular insert) is fixed to the upper part of the tibia. The patella component is to replace the articular surface of the patella.

Among the aforementioned implant failure cases, the failure of the patella component in TKR has been considered of high prevalence (Ayers *et al.* 1997). Early designs of the patella component were all-polyethylene (Huang *et al.* 1999) (Figure 2-1 (a) and (b)). Heavy body weight of some patients and the increase in activity levels brought by both young and older patients are the most severe risk factors for the deformation of the all-polyethylene patella component. Metal-backed designs which consists of a metal substrate with a dome-shaped polyethylene cap were then developed in order to decrease the patella surface strain and support the polyethylene to prevent the deformation (Ayers *et al.* 1997) (Figure 2-1 (c)). However, excessive wear and the fracture of the polyethylene component caused by the high patellofemoral contact stress leads to the dissociation of the polyethylene from the metal substrate and the dissociation / angulation of the fixation pegs. The relative motion between the bone/implant interfaces leads to the ingrowth of fibrous soft tissue, resulting the instability of the implant. Moreover, the use of metal-backed implant has inevitably caused the under-utilisation of the host bone because of the high stiffness of the metal plate, which limited the functional life of the implant and eventually led to the failure of the knee joint arthroplasty (Schmalzried and Callaghan 1999). Therefore, more sophisticated solutions are needed to improve the fixation and stability of the implant (Lee and Goodman 2008).

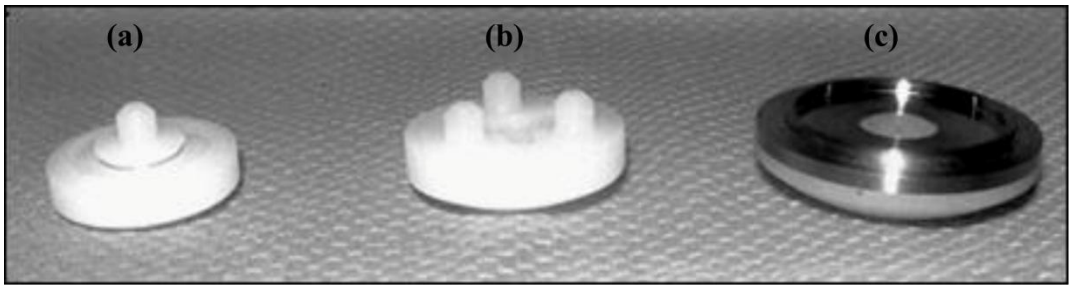

Figure 2-1 Three designs of patella implant components: (a) all-polyethylene component with a single peg; (b) all-polyethylene component with three pegs; (c) metal-backed component with a dome-shaped polyethylene cap. (After Parker *et al*. (Parker *et al.* 2003))

2.1.2 Implant Design Criteria for Bone Fixation

In order to reduce the negative effect caused by the wear and the fracture of the components, dissociation of the fixation pegs from the metal plate and the fracture of the metal plate etc., a better fixation method known as the biological fixation was introduced (Haddad *et al.* 1987; Poss *et al.* 1988; Walker *et al.* 1988). The biological fixation process involves the use of partially or fully porous materials which stimulate the bone ingrowth so that the bone and the implant will integrate (Mullen *et al.* 2009). (Note: when the tissue grows into a porous implant without forming a biological bond to the implant, the fixation method is usually termed morphological fixation.)

Biological / morphological fixation of implants depends on implant material (intrinsic properties), structural design (e.g. pore size, network), mechanical loading and motion at the implant/bone interface. Hence, an optimal implant that is considered for bone fixation should fulfil the following criteria (Alvarez and Nakajima 2009; Atwood *et al.* 2004; Freyman *et al.* 2001; Jones *et al.* 2006; Jones *et al.* 2007; Jones *et al.* 2006):

i. The implant material should be biocompatible (non-toxic) and promote cell adhesion and activity;
ii. It should act as a 3D template with an interconnected 3D pore network with pores suitable for bone ingrowth;
iii. It should have suitable surface properties (e.g. surface chemistry, surface roughness, topology, orientation of struts etc.) to facilitate cell adhesion;
iv. An optimal implant for bone fixation and augmentation purposes should exhibit mechanical properties matching those of the host bone. It should have appropriate modulus to minimise the stress shielding effect as well as to provide sufficient load-bearing ability after implantation;
v. Should be high corrosion and wear resistance to prevent excessive wear debris and loosening that occurs at the interface;
vi. The shape of implants made from the processing technique should match the bone defect area;
vii. It should be capable of being commercially produced in large quantities and sterilized to fulfil the international standards for clinical use.

It is critical that implants possess suitable 3D networks and have sufficiently large pores and interconnects. Cell attachment, nutrition migration and matrix deposition are

achieved by the efficient nutrient and oxygen transportation within the network (Botchwey *et al.* 2003). Previous work has shown that the optimum pore size for bone ingrowth is in the range of 100 – 500 μm (Freyman *et al.* 2001; Hutmacher *et al.* 2004; Okii *et al.* 2001) and interconnect size greater than 100 μm can provide sufficient space for the blood vessel access and the vascularisation (Lu *et al.* 1999; Okii *et al.* 2001). In addition, since the internal surface area is as important as the outside surface in a 3D porous structure, surface properties including struts topology, surface roughness, struts orientation etc., must be considered too (Alvarez and Nakajima 2009). The surface roughness has a direct influence on cell adhesion, osteoblasts proliferation and differentiation. Rougher surfaces are believed to exhibit better cell adhesion than smooth surfaces (Boyan *et al.* 1996; Hatano *et al.* 1999).

An ideal implant for bone fixation should exhibit similar mechanical and physical properties as the host tissue. As natural bone is a hard, load-bearing tissue, the implant should have sufficient strength to retain its structure and to provide the mechanical support for bone remodelling. Wolff's Law (Wolff 1892) states that human bone will remodel in response to the loads which it is placed under. If the load placed on the bone increases, the bone will naturally remodel itself over time to become stronger to resist the load. However, remodelling will be hindered by a permanent implant with stiffness larger than the surrounding tissue. The implant carries a substantial and disproportionate amount of the load. The bone will therefore experience a much lower level of stress and become less dense and weaker during the bone healing process. Conversely, if the implant has stiffness less than the host tissue, potential implant failure will be expected because of the stress concentration in the implant. This uneven load sharing between implant and host tissue is termed 'the stress shielding effect' (Sumner *et al.* 1998). Hence, while the implant needs to have enough strength to retain its structure (Yang *et al.* 2001) *in vivo*, the modulus of the material should not exceed a certain limit in order to avoid the host bone being stress shielded.

2.2 Titanium (Ti) Implants

2.2.1 Titanium (Ti) as Orthopaedic Implant Material

Biocompatible metallic materials such as 316 stainless steel, cobalt chromium (Cr-Co) alloys and Ti and its alloys are frequently accepted as implant materials (Alvarez and

Nakajima 2009). Amongst the available choices of surgical metallic implants, CP-Ti and Ti-based alloys have been clinically used as orthopaedic implant application materials for more than 50 years (Geetha *et al.* 2009). Ti implants are used in fields ranging from stents (Duerig *et al.* 2000), replacement dental implants (Le Guéhennec *et al.* 2007), and replacement orthopaedic devices for shoulders, hips and knees (Head *et al.* 1995), etc., as reviewed by Singh *et al*. (Singh *et al.* 2010).

Ti was found to be a nearly bio-inert and high tolerated material in the body environment (Niinomi 2003). The naturally formed stable TiO_2 layer on the surface provides high corrosion resistance and excellent biocompatibility over stainless steel and Cr-Co alloys. (Kokubo 1996; Singh *et al.* 2009; Spoerke *et al.* 2005; Wen *et al.* 2002; Xue *et al.* 2007).

Ti is relatively lightweight compared to steel. Mechanically, Ti has outstanding properties such as high compressive and tensile strength, low modulus and low density compared to other metals (Geetha *et al.* 2009). In orthopaedic applications, closely mimicking the mechanical properties of host bone is the criterion that is overlooked the most. Human cortical bone has a modulus of 3 – 30 GPa and trabecular bone has a modulus of 1 – 10 GPa (Rho *et al.* 1993). Ti and Ti-based alloys, have lower moduli varying from 55 to 110 GPa (Leyens and Peters 2003) compared with stainless steel (210 GPa (Geetha *et al.* 2009)) and cobalt alloys (220 GPa (Belteridge 1982)); this clearly indicates that the moduli for Ti and Ti-based alloys are much closer to the human bone. Ti and its alloys have high strengths ranging from 220 – 1100 MPa, which are close to stainless steel but with a high specific strength (strength per density). Together with its biocompatibility and high corrosion resistance properties, it is well understood as to why Ti and its alloys are widely used in the biomedical implant applications.

Despite the excellent biocompatibility, strength and corrosion resistance of Ti and Ti alloys, there are still problems associated with Ti implants in orthopaedic applications. The difference between the stiffness of Ti implant and the bone has been identified as a major cause for the surrounding bone experiencing the stress shielding effect (Thelen *et al.* 2004), see Figure 2-2 (a). This can lead to a rapid bone resorption rate, resulting in osteolysis (Figure 2-2 (b)). Furthermore, this mechanical property mismatch subsequently leads to abnormal, relative movement between the Ti implant and bone,

which has been shown to inhibit bone formation and ingrowth. Another critical issue associated with Ti implant is the generation of wear debris, which accumulated in the tissue, also causing the osteolytic lesion in the joint (Kalisvaart *et al.* 2012; Thelen *et al.* 2004). The formation of wear debris can result in fibrous encapsulation leading to pain and to loosening of implants due to a high coefficient of friction (Galante *et al.* 1991). The fibrous encapsulation around Ti implants significantly reduces the mechanical bonding to the surrounding bone and can result in a reduced implant lifetime. Therefore, on-going research is striving to find Ti implants with a similar structure and mechanical properties to that of natural bone, and with the ability to integrate well with the host tissue (Hollister *et al.* 2002; Ryan *et al.* 2009).

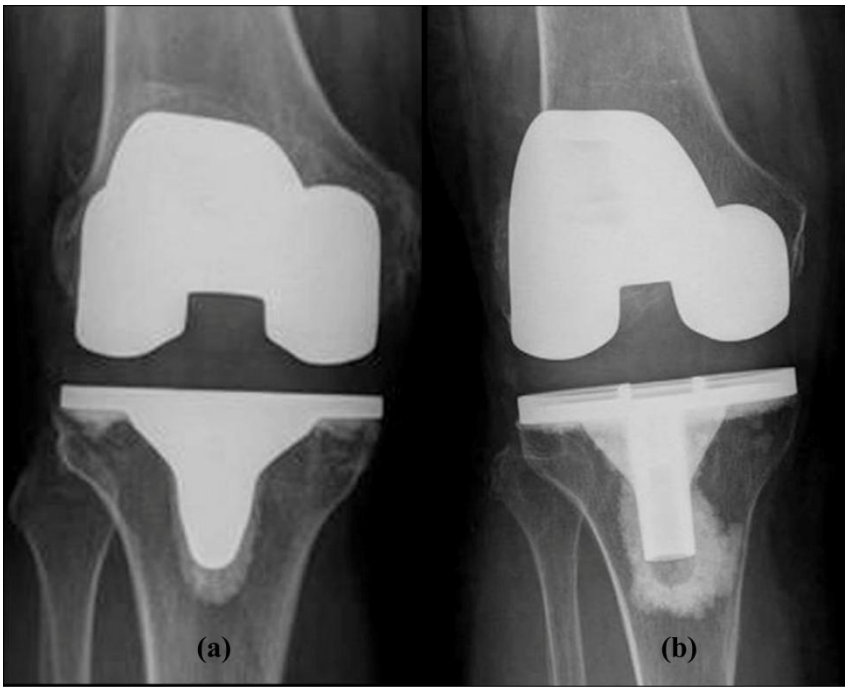

Figure 2-2 (a) 2D radiograph showing the result of stress shielding in the upper part of tibia below the implant in a knee joint after 5 years of TKR surgery. (b) 2D radiograph showing the osteolytic lesion around the tibial component. (After Kalisvaart *et al*. (Kalisvaart *et al.* 2012))

2.2.2 Porous Titanium (Ti) Implants for Bone Fixation

Initial methods used to fix the metallic implants to the bone was to use bone cement and screws (Ryan *et al.* 2006). In joint replacement surgery, liquid acrylic bone cement is injected into the defect area before inserting the implant component. After the cement polymerises, the component wedged against the host bone. Alternatively, the component is fixed rigidly to the bone by screws or interference fits (Harris and Sledge 1990). Such fixation methods have inevitably caused stiffness mismatch which

eventually leads to the need for a revision operation. Improved strategies for fixation could be biological/morphological fixation, which provides the mechanical interlocking between the implant and bone by bone ingrowth (Kienapfel *et al.* 1999; Pilliar 1987; Walker and Robertson 1988). Figure 2-3 shows a patella component that will require cement fixation (a) and the other (b) with a cementless design.

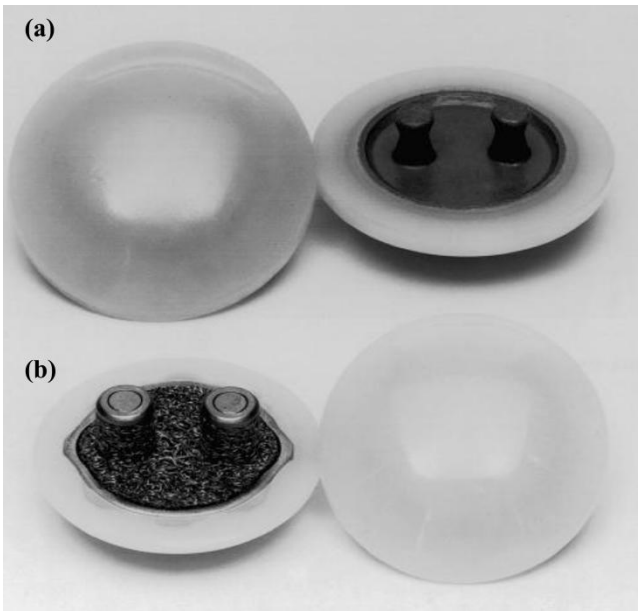

Figure 2-3 Examples of the patella component: (a) cement and (b) cementless metal-backed designs. (After Leopold *et al.* (Leopold *et al.* 2003))

Biological / morphological fixation involves the use of porous metallic implant components. In general, there are three types of porous metal implants: porous coated solid substrates, porous metal component attached to a solid part and fully porous components. Greenfield (Greenfield 1909) first invented the concept of biological fixation in 1909 by employing a metallic framework for a tooth root. The structure allowed bone to grow around and in to hold the implant in position. Since then, there has been a continuous stream of research papers describing the use of various porous coatings as well as fully porous metal scaffolds (Bauer and Schils 1999; Galante and Jacobs 1992; Kienapfel *et al.* 1999; Pilliar *et al.* 1981). Galante *et al.* (Galante *et al.* 1971) developed a Ti fibre-metal composite as a medium for ingrowth bone fixation which was used in hip and knee arthroplasty. In 1983, Pilliar *et al.* (Pilliar 1983; Pilliar *et al.* 1981) introduced an implant consisting of a metal substrate with a porous Ti coating on the surface. Recently, new highly porous metallic scaffolds have been

developed to be used in the orthopaedic applications, such as porous tantalum (Bobyn *et al.* 1999) and porous Ti foams (Mullen *et al.* 2009).

Conventional porous metals such as Ti fiber mesh and Ti plasma spray have some limitations, such as high elastic moduli, low surface roughness, and the requirement of higher porosity to facilitate bone ingrowth (Levine 2008). In order to improve the performance of metal implants, the trend of developing porous metal implants is now towards highly porous metallic structures. It has been shown that this series of implants can be designed to mimic the structure of bone, providing sufficient void space and pathways for cell migration and nutrient transport to effectively encourage the bone ingrowth (Hollister 2005). Wen *et al.* (Wen *et al.* 2001; Wen *et al.* 2002) reported their porous Ti foam fabricated by powder metallurgical process which has both macropores and micropores in the structure. The size of the relative large macropores lay in the range of 200 – 500 μm, which is thought to be optimal for bone ingrowth. The presence of the micropores in range of several micrometers were claimed to have beneficial effect on osteoconductivity. Chen *et al.* (Chen *et al.* 2009) produced porous Ti foam with open pores and interconnected network by liquid foaming method of Ti powder. Large pore sizes in the range of 100 – 400 μm, which is suitable for osteogenesis was achieved and different porosities of the structure could be controlled by changing the amount of foaming agent. Mechanically, highly porous structures effectively reduce the Young's modulus of the implant so that the mismatch of stiffness between the implant and the host bone is less pronounced (Gibson and Ashby 1999; Spriggs 1961). Gibson and Ashby (Gibson and Ashby 1999) suggested that the Young's modulus, E^*, can be approximately estimated by:

$$\frac{E^*}{E_s} = \left(\frac{\rho^*}{\rho_s}\right)^2 \qquad \textbf{2-1}$$

where E_s is the Young's modulus of the solid material and ρ^*/ρ_s is the relative density of the open cell foam.

Imwinkerlried showed that Ti foams of porosity 50 – 80% can be adjusted to have the most ideal properties matching those of the natural bone. The elastic moduli of such Ti foams with 60 – 65% porosity (9 – 14 GPa) also lie in the range of the modulus of human bone (Imwinkelried 2007). Compressive strength of porous Ti foams can be tuned to match that of the natural cortical bone (130 – 180 MPa) by changing the

porosity in the range of 35 – 42% (Krishna *et al.* 2007)). Micro and macro-structures of the Ti foams can also be tailored to achieve desired mechanical properties by altering the pore architecture and 3D network connectivity (Hollister 2005).

The ingrowth of bone in, around and through the implant can also reduce the stress shielding effect by sharing more evenly the load after the implantation (Spoerke *et al.* 2005). Furthermore, porosity of metal implants with complete porous structure can be altered to balance the compressive strength and stiffness so that the implant can retain its own structure in the defect area as well as prevent the stress shielding.

Fujibayashi *et al.* reported that porous Ti foams are found to be inert and exhibit potential bone induction in a non-osseous site when special chemical and thermal treatment was applied on the surface (Fujibayashi *et al.* 2004).

Porous Ti implants being inert, highly biocompatible, exhibiting excellent corrosion resistance and having ideal mechanical properties that match those of the natural bone are therefore a promising choice for orthopaedic implants.

In summary, to design porous Ti structures suitable for orthopaedic applications, it is important to consider the overall requirements of porosity, pore / interconnect size and the mechanical property accordingly. There are a number of methods to fabricate the porous Ti structures, such as sintering Ti powder, space holder method, creep expansion etc. (Lefebvre *et al.* 2008). However, producing such porous metallic foams with designed structural parameters presents challenges to those conventional methods. Novel manufacturing techniques have been therefore proposed to overcome the issue. In the next section, one novel technique to fabricate porous Ti foams with optimum parameters will be introduced.

2.2.3 Titanium (Ti) implants fabrication by Selective Laser Melting (SLM)

There are a number of novel manufacturing routes to produce highly porous Ti foams, as reviewed by Singh *et al.* (Singh *et al.* 2010). Rapid prototyping (RP) is one of such techniques especially for producing the open-cell porous metal foams. Components are built layer by layer.

From early 1980s, RP has been used as a powerful manufacturing technique to quickly produce 3D objects of virtually any shape. Based on computer aided design (CAD)

models and by combining with computer aided manufacturing (CAM), this technique can generate individual components with complex geometries. Since this technique makes it possible to produce object with accurate pre-designed pore size, morphology, interconnectivity and provide possibilities to hierarchically tailor the structure of the object, RP technology has been developed for fabricating orthopaedic implants with porous structures designed for bone ingrowth (Fukuda *et al.* 2011; Mullen *et al.* 2009; Ryan *et al.* 2008; Warnke *et al.* 2008).

Selective Laser Melting (SLM) is a powder-based RP technique which produces metal components based on 3D CAD volume. In a typical SLM building process, the component is built additively in *z*-axis in a layer by layer fashion by using a precise laser beam. The laser beam selectively scans over the metal powder on a substrate plate according to the cross-sections generated from the 3D CAD model. When the laser focuses on an area of powder, the powder in the beam melts, fusing the particles together. Thereafter, the substrate plate is lowered and a new layer of Ti powder is recoated on top and the process is repeated until a full 3D object is produced to replicate the CAD design (Wehmöller *et al.* 2005). Upon completion of the object the substrate plate is removed and excess unsintered powder is recycled. Figure 2-4 shows a schematic of SLM process to produce the 3D metal component using a laser beam to melt the metal powder layer by layer.

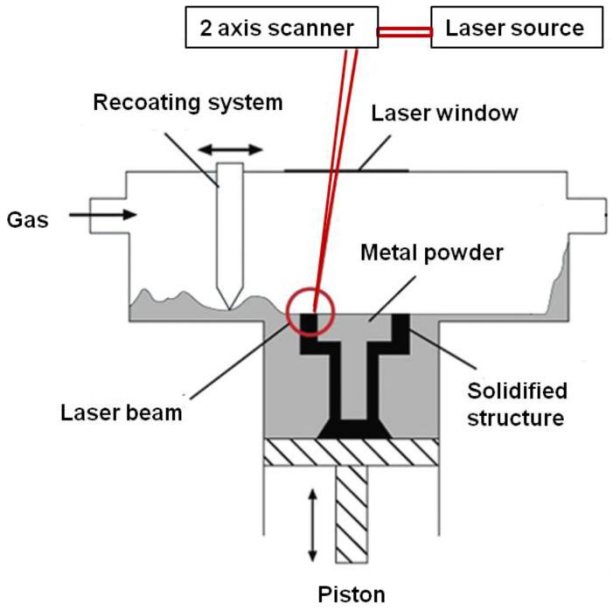

Figure 2-4 A schematic of the SLM process used to produce 3D metal structures. (After Wehmöller *et al.* (Wehmöller *et al.* 2005))

Warnke *et al.* produced porous Ti6Al4V scaffolds using SLM with pore size ranging from 450 – 1200 µm (Warnke *et al.* 2008). Scaffolds showed biocompatibility and proliferation of human osteoblasts *in vitro* in pores ranging from 500 to 600 µm. Wang *et al.* used SLM to produce porous TiH_2-Ti scaffolds with high porosity greater than 70%. The scaffold has interconnected walls and open pore structure with pore sizes in a range of 200 – 500 µm (Wang *et al.* 2010). Mullen *et al.* produced 3D porous Ti structures with both regular and randomised struts arrangements using SLM based on a unit cell approach (Mullen *et al.* 2009; Mullen *et al.* 2010). The method can be used to produce porous Ti foams with porosity ranging from 15 – 70% and unit cell sizes in the range of 600 – 1400 µm. The compressive strength of the Ti implants ranged from 15 to 350 MPa at corresponding porosities between 75 to 15%. It was observed that a 1% decrease in porosity of the scaffold resulted in a 3 MPa gain in compressive strength. And the study stated that the decrease in porosity at the high levels of randomisation was the primary cause of the high strengths observed. The study of the flow and mechanical properties described in this thesis is based on these two types (regular and randomised) of porous Ti structures, which will be discussed in details in the following sections.

2.3 X-Ray Microtomography (µCT)

As earlier discussed in section 2.2, structural parameters such as pores / interconnects size, porosity and morphologically, the shape, distributions of the pores / interconnects and the strut surface roughness have a great influence on cell attachment, proliferation, nutrition transport, vascularisation, ingrowth and mechanical performance. Characterising these properties precisely in 3D is deeply important to help optimising the implant design.

X-ray computed tomography, also termed as X-ray microtomography (µCT), has been established as a non-destructive technique which provides 3D images of the internal micro-structure of an object (Stauber and Muller 2008). The development of µCT has been lead by the medical research because of its ability to provide excellent contrast between bone and soft tissue (Feldkamp *et al.* 1989). Nowadays, µCT machines have been extensively developed for imaging porous materials in many applications. Together with the development of 3D image processing algorithms and analysis

techniques, the quantitative characterisation of the porous materials with complex 3D internal structure can be performed based on μCT images.

The basic physical principle of μCT is that an object attenuates X-rays as it passes through it. X-rays, first discovered by Röntgen (Röntgen 1895), are a form of electromagnetic radiation with a wavelength range of 0.01 – 10 nm and corresponding energies in the range of 0.1 – 100 keV (Van Grieken and Markowicz 2001). It was applied to radiological imaging, which are 2D projections of the X-ray absorption when transmitted through an object (see review by Stock (Stock 1999)). The amount of X-ray attenuation through an object is related fundamentally to the composition of the object and the energy of the X-ray source. In the energy range used for CT imaging, the photoelectric effect when the matter encounters the X-ray creates the main attenuation. The relationship between the intensity of unattenuated, monochromatic X-ray and the intensity after it traverses through an object is given by (Stock 1999):

$$I = I_0 e^{\left(-\frac{\mu}{\rho}\right)\rho x} \qquad \textbf{2-2}$$

where I_0 is the intensity of the unattenuated X-ray beam, I is the intensity of the beam after it traverses through an object with a thickness of x. The energy-dependent material constant μ is called the linear attenuation coefficient, which varies along the beam and depends on both the local mass density of the sample and the energy of incident photons (Maire *et al.* 2001). It is the amount of radiation being attenuated by the material on an infinitely small distance. For monochromatic X-ray source, the linear attenuation coefficient is proportional to the density of the material. Hence μCT images represent different densities in different intensities. Dividing the linear attenuation coefficient by the density of the material (ρ) gives the mass attenuation coefficient of the material, which describes how strongly the material attenuates the X-ray per unit mass.

Writing Equation 2-2 in differential form with respect to infinitely small thickness dx:

$$\frac{dI}{I} = -\frac{\mu}{\rho}\rho dx \qquad \textbf{2-3}$$

As dx is an infinitely small increment, (μ/ρ) ρ is treated as a constant, written as μ. Adding the increments of attenuation along the X-ray propagation direction gives the Beer-Lambert Law, a more general form of Equation 2-3:

$$I = I_0 e^{-\int \mu(s) d\boldsymbol{s}} \qquad \textbf{2-4}$$

where $\mu(s)$ is the linear absorption coefficient at position s along the ray $\boldsymbol{s}$. Therefore, an X-ray radiograph represents a map of the sum of all local attenuations along the X-ray beam (Stauber and Muller 2008).

Rewriting the above equation leads to:

$$\int \mu(s) d\boldsymbol{s} = \ln\left(\frac{I_0}{I}\right) \qquad \textbf{2-5}$$

which shows explicitly that assigning the correct value of μ to each position, s, along the ray $\boldsymbol{s}$ from a knowledge of only the values of the line integral for the various orientations of $\boldsymbol{s}$ is the essential problem of computed tomography (Stock 1999). Measuring I_0 / I for many different positions s for a given $\boldsymbol{s}$ is required, thus a series of radiographs which measure the value of I_0 / I obtained at enough directions $\boldsymbol{s}$ is collected in order to reconstruct the object volume.

In μCT, a set of 2D radiographs are collected while rotating the sample in very small steps (< 1°) around a single axis of rotation. The 3D volume image is numerically reconstructed (normally using a filtered back-projection (FBP) algorithm (Feldkamp 1984; Herman 1995) from the 2D images collected in a full 360^o set of views.

The quality of the μCT image is limited by the X-ray energy / intensity, X-ray focus size, the size of the detector and the object being scanned.

μCT systems employ two main types of X-ray sources: synchrotron parallel radiation and Micro / Nano focus X-ray tube head. Laboratory-based μCT use the Micro / Nano focus X-ray tube heads which generate polychromatic X-rays. The X-ray diverges from the source (a cone shape) and only those parts of the object which remain in the beam throughout the entire rotation can be used in the reconstruction process afterwards. A cone beam system used in lab-based μCT is illustrated in Figure 2-5.

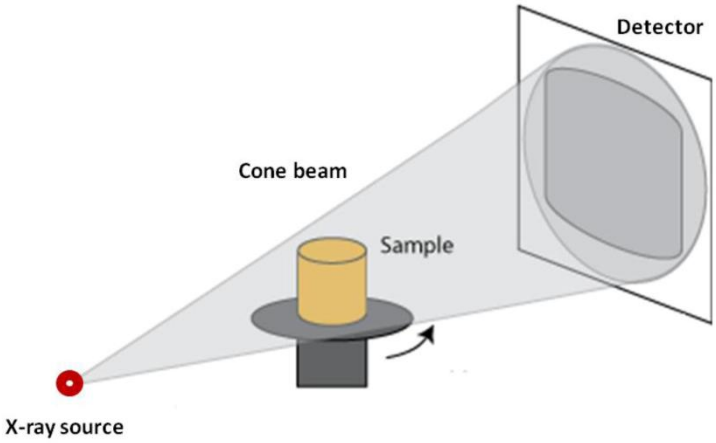

Figure 2-5 Illustration of a cone beam system used in lab-based μCT. Figure modified from http://serc.carleton.edu/research_education/geochemsheets/techniques/CT.html (Ketcham, 2012)

Polychromatic X-rays may introduce an artefact termed "beam-hardening". The beam-hardening effect occurs due to the preferential absorption of lower energy X-rays, which results in the mean value of energy shifting to higher values (beam hardens) as the X-ray traverses through the object (Stock 1999). The reconstructed image will look brighter at the edges than at the centre and streak artefacts may appear (Van de Casteele *et al.* 2002). To minimise this effect, one common way is to use a thin layer of metal filter which can pre-filter the low energy photons before the X-ray enters the material (Stauber and Muller 2008). Another common artefact that occurs in μCT imaging is the ring artefact due to individual defective pixel-elements or pieces of dust on the detector, which will cause a bright ring to superimpose onto the reconstructed image. The ring artefact can be potentially reduced by replacing the defective pixel by an average value of the neighbouring pixels.

With the cone beam μCT system, the magnification can be adjusted by changing the position of the object being scanned between the X-ray source and the detector. However, the maximum resolution is limited by the X-ray focal spot size (Maire *et al.* 2001). The smaller the spot size, the better the resolution can be achieved. The use of small spot size will limit the X-ray energy that can be applied on the target and therefore the resulting intensity. Hence when higher X-ray power is needed, it is necessary to select a larger spot size which will incur a point of blur on the image.

The size of the detector and the sample also affect the quality of the μCT image. The number of pixels in the detector determines the maximum spatial resolution. And the maximum nominal resolution that can be achieved is related to the size of the sample being scanned. For accurate reconstructed image quality, the size of the sample being scanned should not exceed the field-of-view (Stauber and Muller 2008).

Materials characterisation using μCT has emerged in a wide range of research fields, such as bone structure characterisation (Balto *et al.* 2000; Kuhn *et al.* 2005; Müller *et al.* 1998), geomaterials (Lindquist *et al.* 2000; Macedo *et al.* 1999) and metal solidification (Atwood and Lee 2003). Recently, there have been a number of studies applying μCT together with advanced image analysis techniques to characterise the structure of tissue engineering scaffolds (Jones *et al.* 2009; Maire *et al.* 2003; Moore *et al.* 2004; Otsuki *et al.* 2006; Yue *et al.* 2011). The quantification of pore and interconnect size, as well as their distributions, has been performed via μCT data. In addition to structural quantification, μCT image data can also be converted into computational fluid dynamics and finite element models for analysis (Jones *et al.* 2009; Jones *et al.* 2007; Singh *et al.* 2009). This thesis will focus on the characterisation of the flow and mechanical properties of the Ti scaffolds based on 3D images taken via μCT.

2.4 Modelling of Fluid Flow

2.4.1 Permeability of Porous Materials

Fluid flow through the porous implant is required as it significantly affects the transport of cells, nutrients and growth factors into the porous implant after implantation. The concept of permeability was first introduced in the establishment of the theory of transport phenomena in porous media (Bear 1988). Permeability is a measure of the ease at which liquid flows through a porous structure under a pressure gradient and is a convenient way to characterise the bulk flow. Permeability influences vascular invasion and the supply of nutrients required to sustain cell growth and also provides an outlet for the removal of cell debris, thereby increasing its osteoconductive potential (Yang *et al.* 2001). Hui *et al.* (Hui *et al.* 1996) highlighted the importance of implant permeability, reporting results that show high implant permeability enhances the integration of the implant with the host bone. In addition to flow, permeability can also

be related to the internal topology of foams, the porosity, and the surface roughness of the foam struts.

At low fluid velocities, the permeate flux across trabecular bone implants is found to be well predicted by Darcy's Law (Equation 2-6) (Despois and Mortensen 2005; Hui *et al.* 1996; Nauman *et al.* 1999):

$$Q = \frac{R}{A} = \frac{K}{\mu}\frac{\Delta P}{L} \qquad \textbf{2-6}$$

where R is the volumetric flow rate, A is the cross sectional area of the porous structure, Q is the permeate flux across the sample structure, K is the permeability, μ is the dynamic viscosity of the fluid and L is the length over which a pressure difference, ΔP, is measured. Typically during cell culture studies using bioreactors, flow rates through the porous structures are low and generally do not exceed 1 ml/min (Cartmell *et al.* 2003), remaining in the low Reynolds number, or creeping flow regime. However, when experimentally measuring permeability, flow rates of this order are impractically low for easy measurements and much higher flow rates are often employed, thereby creating a situation which shifts the flow from laminar flow to transitional or even turbulent flow. These regions are defined in terms of the Reynolds number (*Re*) as laminar flow ($Re < 10$), intermediate flow ($10 < Re < 300$) and turbulent flow ($Re > 300$) (Ziółkowska and Ziółkowski 1988), where *Re* for determining the flow regime of fluid in a porous media is defined as (Holdich 2002):

$$Re = \frac{\rho v}{\mu(1-\varepsilon)S_v} \qquad \textbf{2-7}$$

where ρ is the density of the fluid, v is the superficial velocity of the fluid, ε is the porosity of the object that the fluid flows through and S_v is the surface area per unit volume.

Permeability measurements have been performed by various groups of researchers on bone and other biomaterials (Chen *et al.* 1998; Kohles *et al.* 2001; Sahimi 1995; Shimko *et al.* 2005), who have demonstrated that when measuring the permeability using water, foams of nominal characteristics (porosity > 60% and pore size range 100 – 500 μm) show transitional or turbulent behaviour at flow rates greater than 10^{-2} m/s. When this is the case, the Dupuit-Forrcheimer modification of Darcy's Law must be used (Despois and Mortensen 2005):

$$-\frac{dP}{dL} = \left(\frac{\mu}{K}\right)v + \rho C v^2 \qquad \textbf{2-8}$$

where *C* is a characteristics coefficient of the fluid.

A number of research groups have performed experimental measurements of permeability of cortical and trabecular bone. The permeability of bone depends highly on its structure and density. Grimm and Williams (Grimm and Williams 1997) measured the permeability of human calcaneal trabecular bone by flowing fluid through the sample in the mediolateral direction in a tube connected to a fluid reservoir. The permeability was calculated using Darcy's Law and expressed as a function of pore volume fraction, ranging from 4×10^{-10} and 1.1×10^{-8} m^2. Li *et al.* (Li *et al.* 1987) measured the permeability of cortical bone of canine tibiae to be 2.5×10^{-13} m^2 by measuring the volume of fluid flow in a fixed time through the sample in calibrated containers connected to a pressurized tank. Kohles *et al.* (Kohles *et al.* 2001), who have worked with cubic trabecular bone samples, further confirmed the previous estimated range of the permeability values by measuring trabecular bone anisotropic permeability using direct perfusion method. The intrinsic permeabilities were found to be in the range of 2.3×10^{-10} to 4.7×10^{-10} m^2, varying with both location and direction. Ideally implant structures could be tuned to match this order of magnitude range in values.

Although prior Ti foams have not been designed explicitly for matched permeability, a number of authors have measured this property for different foam types. For example Shimko *et al.* (Shimko *et al.* 2005) found their tantalum porous structures with porosities in a range of 66-88% to have permeabilities ranging from 2.1×10^{-10} to 4.8×10^{-10} m^2. Ochoa *et al.* (Ochoa *et al.* 2009) used volumetric flow rates of water in the range of $50 - 400$ ml/min in bioglass based glass-ceramic scaffolds of $90 - 95\%$ porosity and yielded an intrinsic permeability value of 1.96×10^{-9} m^2. Despois *et al.* (Despois and Mortensen 2005) found the permeability increased from 1.23×10^{-12} to 3.56×10^{-11} m^2 as they reduced the relative density of the scaffold from 32 to 12%, keeping the average pore size constant at 75 µm. They also tried to change the average pore size from 75 to 400 µm while keeping a similar relative density, which increased the permeability from 3.56×10^{-11} to 7.64×10^{-10} m^2. Since a larger value for permeability means easier flow, reducing density (large flow passages) or having bigger pores (less surface area) should increase permeability as observed. Singh *et al.* (Singh *et al.* 2009), characterised Ti foams of 65% porosity with a modal pore size of 440 µm, and found

their structures to have permeability values in the range of 1.17×10^{-10} to 1.63×10^{-10} m^2 depending on the flow direction. In summary, common metal foams being considered for implants with porosities ranging from 50 to 95% were experimentally found to have permeability values in the range 10^{-12} to 10^{-8} m^2.

2.4.2 Computational Fluid Dynamics (CFD) Simulation - Permeability

Modern CFD analysis development began in early 1950s with the advent of the digital computer (Chung 2010). CFD is a general term for solving fluid mechanics problems using numerical methods and algorithms. The fundamental physical theory which defines fluid flow can be represented by partial differential equations (PDEs). CFD algorithms solve these PDEs using discretised methods to replace the original PDEs by discretised algebraic functions to produce numerical results.

The same basic steps are followed in all CFD approaches:

i. Pre-processing: The test geometry of the flow problem is defined. The void volume (volume occupied by fluid) is then divided into discrete elements (the mesh). The physical governing equations are defined, together with the boundary conditions specified.
ii. CFD simulation: The governing equations of the fluid motion are discretised and the solved iteratively as either steady-state or transient.
iii. Post-processing: The numerical results are analysed and graphical processor is used for visualisation of the result.

There are many CFD solution approaches to provide the numerical solution of the fluid motion PDE. The most common in commercially available CFD programs are:

- Finite volume method
- Finite element method
- Finite difference method

Performing computational modelling of fluid flow using CFD algorithms overcomes many experimental difficulties and allows direct design and tailoring of permeability.

2D numerical approaches of calculating permeability by solving the Navier-Stokes equation (N-S equation), which will be discussed later on, were reported by Nagelhout *et al.* (Nagelhout *et al.* 1995) on fluid flow through a square array of cylinders. The

author applied a finite element algorithm to compute the numerical solutions of velocity and pressure drop from the flow equation. Other authors (Papathanasiou and Lee 1997; Woods *et al.* 2003) have used the boundary element method to calculate permeabilities for both perfect square arrays of aligned cylinders and domain with randomly placed particles. They found that, for high porosity volumes (greater than 80%), the randomised structure has a slightly higher permeability than a perfect square array.

High resolution µCT imaging techniques allow the reconstruction of the 3D morphology of the structure (Feldkamp *et al.* 1989). Its advantageous non-destructive 3D imaging properties allow the direct computation of permeability from real 3D scaffold volumes. Several studies (Bernard *et al.* 2005; Fuloria *et al.* 2008; Jones *et al.* 2007; Khajeh and Maijer 2012; Singh *et al.* 2009) performed computation of permeability from real 3D microstructures. For example, Jones *et al.* (Jones *et al.* 2007) predicted the flow in a bioactive glass scaffold with complex 3D structures. Starting with µCT images, the flow velocity was predicted by numerically solving the Stoke's equation and by using the volume averaging code presented by Anguy and Bernard (Anguy *et al.* 1994) to determine the permeability. Figure 2-6 shows the flow inside the scaffold as streaklines passing through the pores and interconnects. It is clearly shown in this study that interconnects in the scaffold structure dominate the flow as the streaklines representing the flow paths all converges at those interconnects.

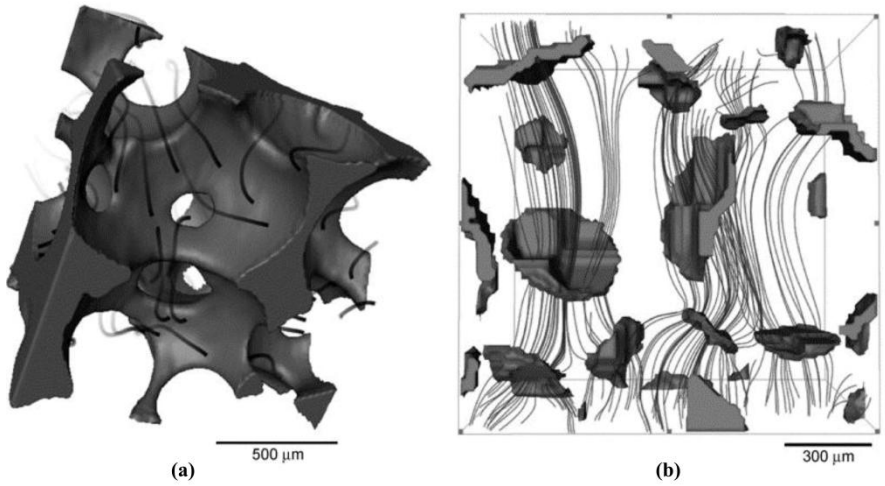

Figure 2-6 (a) 3D rendering of a bioactive glass scaffold with streak lines of resultant flow inside predicted by solving for Stokes flow (b) The scaffold volume is removed except interconnects, leaving the streaklines passing through and converging at interconnects. (After Jones *et al.* (Jones *et al.* 2007))

Singh *et al.* (Singh *et al.* 2009) studied the permeability of Ti foams produced by the space-holder technique for spinal fusion devices. The 3D structures of Ti foams with different levels of porosity were obtained using μCT. Then a finite element mesh was created to obtain a discretised model from the μCT image to calculate the permeability of the scaffold using a commercial CFD package FLUENT™. The simulation flow model was assumed to be steady state incompressible flow of a Newtonian fluid. The nonlinear N-S equation was solved numerically by the control volume method and then applying Darcy's Law to calculate the permeability. Results showed that the μCT predicted permeability values agree well with the experimental values at high porosity. And the author has also stated that for an accurate evaluation of the permeability using CFD, the least edge length of the simulation volume should be three to five times the pore size. Khajeh and Maijer (Khajeh and Maijer 2012) applied a similar CFD numerical method to evaluate the permeability change in dendritic solidification by Darcy's Law, based on the μCT imaged Al-Cu alloy microstructures. The numerical results were validated against both physical and analytical values of permeability and showed accuracy within ±30%.

The above studies have used different CFD approaches to numerically model the flow in porous media. Finite volume based CFD method will be employed to solve the fluid motion equation in both permeability and bone ingrowth models. In the latter case, the CFD code will be also combined with the finite difference method and the cellular automaton method, which will be discussed in details later on.

2.5 Modelling of Mechanical Behaviour

One other important criterion to consider when designing the optimal implant is that the structure should exhibit mechanical properties matching those of the host tissue. The human patella undergoes two types of force: during knee extension, it is loaded in tension and then during knee flexion, it is subjected to compressive stresses. Depending on the angle of knee flexion, the amount of compressive stress on the posterior side of the patella as the knee bends may be subjected to 3 - 11 MPa on either facet (lateral or medial patella-femoral facets) (Xu *et al.* 2007).

2.5.1 Mechanical properties of Ti Foams

The structural properties of metallic foams such as CP-Ti scaffolds can be investigated through the stress-strain relationship, especially under load bearing compression condition. A typical compressive stress-strain curve for elastic-plastic metallic foam is shown in Figure 2-7. There are three distinct regions in a stress-strain curve (Gibson *et al.* 2010):

i. An initial linear, elastic region, and its slope is the modulus of elasticity (Young's modulus),
ii. A plateau region beyond the elastic limit, where permanent deformation is expected to occur, and eventually
iii. A densification region where stress increases rapidly at high values of strain and the pores collapse and pore walls compress against each other.

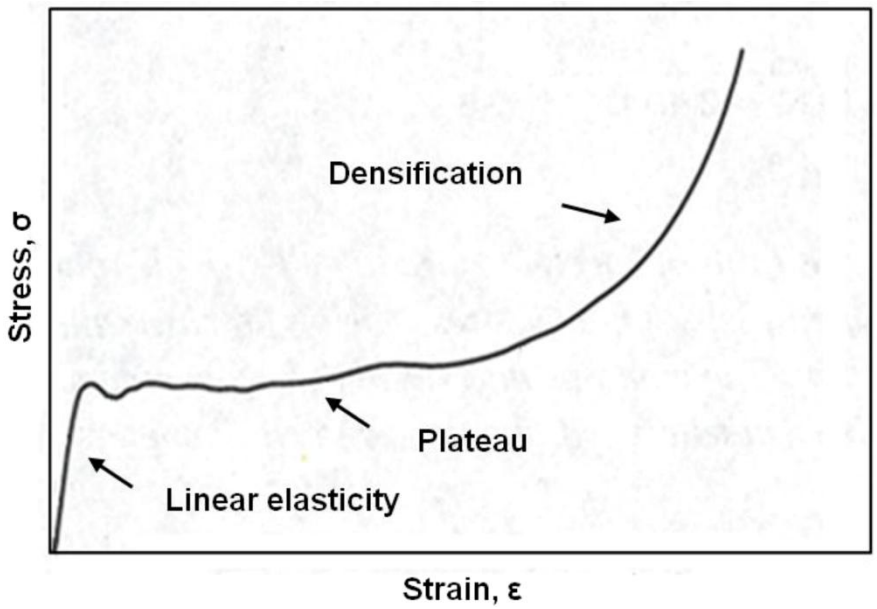

Figure 2-7 A typical schematic uniaxial stress-strain curve for elastic-plastic metal foam in compression. (After Andrews *et al.* (Andrews *et al.* 1999))

The curve describes the relationship between the stress and strain when a compressive force is applied on a deformable object. The stress, σ, is derived from the load applied on the object using

$$\sigma = \frac{F}{A} \qquad \textbf{2-9}$$

where F denotes a tensile force if it is acting outward from the plane, or in this case, a compressive force which is acting inward to the plane and A is the cross-sectional area

of the object the force is acting upon. The strain, ε, is expressed as the ratio of total deformation to the original length of the object on which the force is being applied:

$$\varepsilon = \frac{\Delta L}{L} = \frac{l - L}{L} \qquad \textbf{2-10}$$

where L is the initial length of the material and l is the final length after compression.

Gibson and Ashby (Gibson and Ashby 1999) claimed that the initial elastic regime of the curve is the result of the collective bending of foam struts oriented perpendicularly to the loading axis, known as a crush banding. The Plateau region is caused by a series of struts oriented parallel to the loading direction, leading to the collapse spread through the structure at nearly the same critical stress. At the stage where the foam struts begin to be in contact with each other, the steeply increasing stress indicates that the foam tends to exhibit a similar modulus to that of the monolithic materials it is fabricated from.

The mechanical properties of the porous scaffold, such as compressive strength and elastic modulus depend on: (1) the microstructural parameters of the scaffold, i.e. the pore size, morphology, struts thickness, etc.; (2) the macrostructual properties of the structure, i.e. the spatial distribution of the pores and the overall porosity of the structure. Traditional methods for characterising mechanical behaviour of porous metal scaffolds were experimental approaches. There have been numerous studies on measuring the mechanical properties of porous scaffolds using static compression test, in which the samples are compressed between two parallel plates (Banhart and Baumeister 1998; Davies and Zhen 1983; Eshraghi and Das 2010; Imwinkelried 2007; Zhang and Wang 2005). The results from these static compression tests showed the general trend that increasing porosity of the metal foam will decrease the elastic modulus of the foam (Oh *et al.* 2003). However, many studies highlighted the need of further investigation on the effect of not only overall porosity but also other structural properties on the mechanical properties of the foam. For example, Zhang *et al.* (Zhang and Wang 2005) suggested that the discrepancies in the pore shapes (perfect spherical vs. non-spherical shaped) might lead to the difference in the stress-strain curves of foams fabricated by different methods but with similar porosities. Balla *et al*. (Balla *et al.* 2010) showed different stress-strain curves for two Ti scaffolds with similar porosity but random and designed pores, suggesting the need of further investigation focusing on the internal microstructure effect on mechanical behaviour.

With the development of standard and high-resolution μCT imaging, studies have combined the 3D imaging technique with the mechanical test so that the investigation of how the structure micro/macro-structures affect the mechanical properties of the porous scaffold is allowed (Babout *et al.* 2003; Elliott 2002; Maire *et al.* 2003; Thurner *et al.* 2006). Elliott *et al.* (Elliott 2002) performed the compression test on open-cell polyurethane foam *in situ* at a selection of compressive strains using high resolution synchrotron tomography. By analysing the profile of the average density against the compression axis pixels from the tomographs, a displacement map of the microscopic strain in the sample was constructed to show that the deformation occurred homogeneously in the elastic region up to a compression strain of 6%. Dillard *et al*. (Dillard *et al.* 2005) used the 3D μCT combined with the *in situ* mechanical test to study the deformation behaviour of open-cell nickel foam under compression loading. They reported that the deformation of the metal foam was associated with the strain localisation due to the buckling of the free-edge struts parallel to the loading direction. Ohgaki *et al.* (Ohgaki *et al.* 2006) later discussed about high resolution μCT observations of deformation behaviour of aluminium foams being compressed in *in situ* test rig. By tracking the position of the centroid of the micropores as a function of applied strain in sequential tomographic scans, 3D local strain distribution in the foam can be estimated. They reported, in terms of microscopic effect on deformation, that the microcracks were initiated from pores with larger diameter (above 30 μm) and the cells walls were more strongly damaged compared to the pores. Balla *et al*. (Balla *et al.* 2010) performed *ex-situ* compression test on Ti foams of similar total porosity (30%) but with random and designed porosities. Analysis of μCT images taken before and after the compression test showed that the random porosity sample exhibited a uniform deformation at low strain (below 0.28) and localised deformation at relatively high strain (0.28-0.45) due to buckling of the sample. The sample with designed porosity collapsed at a lower strain of 0.18 but showed a higher modulus/strength compared to the randomised sample due to its stronger and more stabilised wall structure.

As a summary, direct observation of compression test using μCT provides better understanding of how internal structure, overall porosity, pore size and morphology of the porous scaffold affect its mechanical behaviour. The dependence of deformation on scaffold micro/macro-structural properties can be therefore analysed. In the following section, another approach, finite element modelling, which provides the computational

route to effectively study the 3D mechanical behaviour of the porous scaffold will be reviewed.

2.5.2 Finite Element (FE) Modelling – Compression Test

In order to evaluate accurately how microstructure influences the mechanical response of porous materials under compression, it is very useful to take the finite element analysis (FEA) approach as it can provide detailed microstructural changes of the scaffold under mechanical loading.

Previously, deformation and local failure in trabecular bone under load bearing condition have been studied using FEA based on μCT images (Müller and Harry van Lenthe 2006; Nagaraja *et al.* 2005; Niebur *et al.* 2000). Bayraktar *et al*. (Bayraktar *et al.* 2004) constructed 3D FEA models of human trabecular and cortical bone which simulated the mechanical loading environment. The FEA predictions of elastic modulus and compressive yield strength at bone failure were similar to experimentally measured results, indicating that the use of FEA would be a viable and accurate tool for understanding the insight of stress concentrations and failure mechanisms. Simulations based on 2D and 3D FEA previously used to study the mechanical behaviour of porous scaffolds showed advantages over experimental methods and also analytical methods such as Gibson and Ashby's model (Gibson *et al.* 2010). The computational approach effectively reduces the experiment errors and is able to analyse the model under different loading conditions. From the analytical point of view, the FEA model gives details on individual elements so that the assumption of the single unit cell representing the bulk structure is no longer in consideration. Moreover, studies using FEA have shown that this approach could provide approximate evaluation of the localised stress and strain. Thelen *et al*. (Thelen *et al.* 2004) modelled uniaxial compressive tests using 2D FEA to investigate the effect of pore morphology changes on the elastic modulus of a CP-Ti scaffold with a median porosity of 33%. Three cases with smoothed pores, elongated pores and elements representing pores assigned as bone were simulated. Results showed that the change of pore shape has increased the modulus in the elongation direction and the modulus of the model with pore filled with 'bone ingrowth' has doubled. However, the accuracy of the model was limited by the dimension of the test.

Ryan *et al*. (Ryan *et al.* 2009) applied 3D FEA on Ti scaffolds with repeating unit cell structures. Uniaxial compression tests were simulated using commercial FEA software, ABAQUS^{TM}. Three Ti scaffolds with different porosities (51.4 – 66.8%) were tested in two models which were a single unit cell and a large macroscopic volume, respectively. The results showed that increasing the porosity reduced the elastic modulus and yield strength in both the axial and transversal directions under a nominal strain of 0.02. The difference in mechanical properties between single unit cell and the macroscopic volume was found to be small due to the homogeneity of the structure. However, the failure modes of scaffolds along both the axial and transversal directions showed different plastic strain concentration locations. Eshraghi *et al*. (Eshraghi and Das 2010) also performed a 3D FEA simulation in COMSOL Multiphysics^{TM} on polycaprolactone scaffolds with porosities ranged from 51 – 81%. Uniaxial compression test in vertical direction was performed using an axial strain of 0.01. The effective modulus predicted by the computer model agreed with the experimentally data with a percentage error of 30%.

In this thesis, the 3D FEM simulation was performed to model the mechanical behaviour of the Ti foams under compression load. The model was used to study the effect of structural properties of the porous Ti foam on its compressive behaviour and the results were compared against an interrupted static compression test characterised based on μCT images.

2.6 Modelling of Bone Ingrowth

Bone is subjected to complex mechanical stimuli in the body, which induce fluid flow in the tissue. The following sections discuss the effect of the fluid flow-induced shear stress on bone remodelling and review the previous work on determining the shear stress magnitude and modelling of bone ingrowth.

2.6.1 Fluid Flow-induced Shear Stress

During the bone remodelling process, it is well established that vascularisation plays an important role in bone formation. Previous studies have found that increased vascularisation will effectively promote the osteogenic cell proliferation and activity during the healing response in bone (Pelissier *et al.* 2003; Simmons 1979; Solheim *et al.* 2001; Vezeridis *et al.* 2006). Increased vascularisation and osteogenesis in bone healing

process are related to the interstitial fluid flow in periosteum and surrounding tissues (Wray and Lynch 1959).

Mechanical loading is one important mechanism to produce interstitial fluid flow in the bone tissue (Hillsley and Frangos 1994; Knothe Tate *et al.* 1998; Weinbaum *et al.* 1994). Figure 2-8 shows a schematic of mechanical loading induced interstitial fluid flow and the mechanical movement induces the interstitial fluid flow and applies shear on cells.

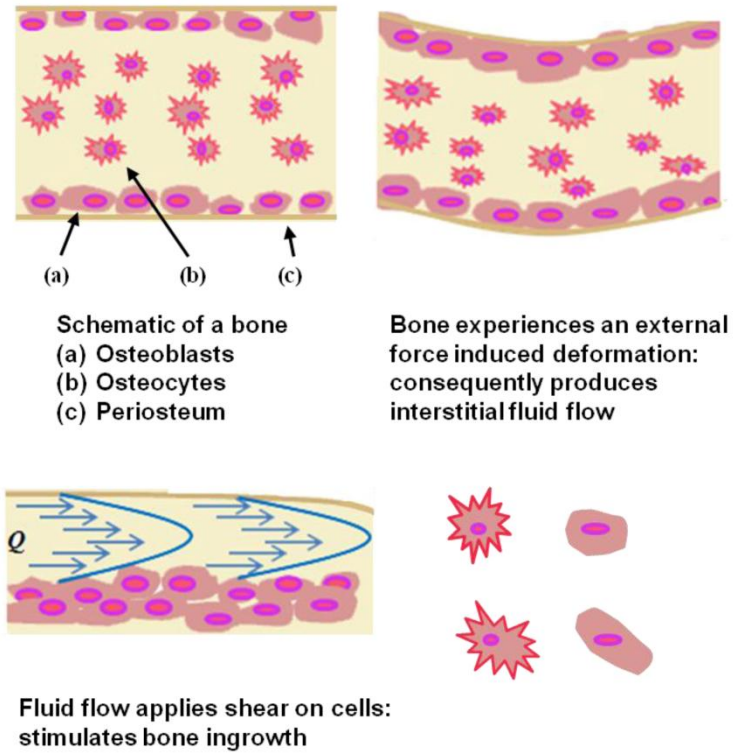

Figure 2-8 Schematic of mechanical deformation induced interstitial fluid flow. Fluid-induced shear stress comes from the mechanical movement, upregulating cell proliferation / attachment and hence the bone ingrowth. (After Carvalho *et al.* (Carvalho *et al.* 2001))

The shear stress induced by the interstitial fluid flow is believed to have an up-regulated effect on osteoblasts proliferation and vascularisation. The study by Dillaman *et al.* (Dillaman *et al.* 1991) suggested that the fluid movement is significantly involved in the growth of the bone. Johnson *et al.* (Johnson *et al.* 1996) hypothesised that fluid flow-induced shear in bone regulates continuous and rapid release of nitric oxide from osteoblasts and the vascularisation introduced by the fluid flow may stimulate bone formation. Owan *et al.* (Owan *et al.* 1997) performed osteoblast-like cell culture on collagen-coated plated plates and investigated the effect of the fluid flow and localised

mechanical stimuli on cellular response. The plate was bent by applying a 4-point loading, causing compressive strains on cells. Fluid shear and pressure were imposed on cells when the plate was pushed through the medium. They found that high magnitude of fluid forces significantly increased the osteopotin (noncollagenous bone matrix protein) expression and suggested that the osteoblasts are more responsive to the fluid flow than to mechanical deformation. Several studies have also modelled the mechanical induced flow in bone. Piekarski (Piekarski 1977) modelled the compression that occurs naturally in the Haversian network and showed that it produces interstitial fluid flow in the bone. Later Kufahl and Saha (Kufahl and Saha 1990) developed a model based on Piekarski's model of the osteon system. They predicted that mechanically induced fluid flow which transports metabolites in canaliculi (nominal diameter = 0.2 μm) can sustain a maximum velocity of 0.1 mm/s. Weinbaum *et al.* (Weinbaum *et al.* 1994) modelled a system which relates the mechanical loading on the bone to the fluid shear stress applied at the surface of the cell osteocytic process and the predicted shear stress was in a range of 0.8 – 3 Pa, which is similar to the measured fluid shear stress in osteoblasts. They suggested that osteocytes, which are fully differentiated osteoblasts embedded in the calcified matrix of bone, can be stimulated by the mechanical loading induced fluid shear stress acting on the membranes and thus promoting bone ingrowth.

Similar to the mechanical loading system, fluid flow-induced shear stress applied on the implant structure in *in vitro* 3D perfusion systems has also been found to have important stimulatory effects on cell and tissue growth (Dillaman *et al.* 1991; Kapur *et al.* 2003; Sikavitsas *et al.* 2003). Freed and Vunjak-Novakovic (Freed and Vunjak-Novakovic 2000) used a rotating cylinder bioreactor system that continuously perfuses the culture media to the construct surface. The flow at the construct surface was assumed to be laminar and a maximum shear stress in the order of 80 mPa was estimated. Raimondi *et al.* (Raimondi *et al.* 2002; Raimondi *et al.* 2004) was the first to perfuse the culture medium through the 3D internal chondrocyte-seeded scaffold structure and predicted that a wall shear stress in the range 1.5 – 13.5 mPa was required for a positive effect on seeded cell viability and proliferation *in vitro*. Botchwey *et al.* (Botchwey *et al.* 2003) used a 3D culture system under flow with velocities in the range of 0.01 to 0.1 mm/s and applied Darcy's Law to analytically estimate the flow rate in the flow. The maximum fluid shear stress acting on the exterior surface of the porous

scaffold in the order of 30 mPa was estimated by the Stoke's approximation. By assessing the MC3T3-E1 osteoblast-like cell viability qualitatively by confocal microscopy and by measuring the DNA content within the bone trabecular scaffolds perfused at flow rates 0.01 to 1 ml/min, Cartmell *et al.* (Cartmell *et al.* 2003) suggested that perfusion at flow rates less than 0.2 ml/min will enhance the transport of nutrients and stimulate the tissue growth.

In the direct-perfusion experiments, different design architectures and porosities of the construct will result in different shear stress level applied to the cells on the construct surfaces. Knowledge of how shear stress relates to cell growth in various design architectures can help optimise implant design and manufacture. An understanding of fluid flow-induced shear stress within porous structures, as well as induced cell ingrowth, is therefore crucial. In the next section, several prior numerical studies on the estimation of flow-induced shear stress in the perfused constructs and the prediction of the subsequent bone ingrowth will be reviewed.

2.6.2 Numerical Simulations - Fluid Shear Stress and Bone Ingrowth Estimation

Computational modelling of fluid flow using CFD algorithms has enabled the simulation of perfusion culture of osteoblasts through porous scaffolds. The computational models will allow the prediction and testing of various parameters which will affect the hydrodynamic environment and the tissue growth in a shorter timescale than perfusion culturing in bioreactors. There have been a number of authors who applied numerical models to evaluate the flow-induced shear stress acting on the scaffold walls at different perfusion rates and several of them have also predicted the bone ingrowth stimulated by the shear.

Raimondi *et al.* (Raimondi *et al.* 2002) developed a 2D CFD model to characterise the macroscopic flow through a scaffold made of hyaluronic fibres. The model was a first attempt to provide the correlation between the fluid shear stress and cultured cell response. The 2D domain in this model was a simplified geometry based on the light microscopic image of the fibre geometry. The fluid flow was modelled as a laminar flow with a low Reynolds number of 6.34×10^{-4}. The culture media was an incompressible, Newtonian fluid with constant density, $\rho = 1\times10^{3}\,\mathrm{kg/m^3}$ and the viscosity, $\mu = 8.2\times10^{-4}\,\mathrm{kg/ms}$. The CFD model applied a commercial finite-element code FIDAP (available in FLUENT) to solve the N-S equation. It predicted a median

shear value of 3 mPa and a maximal shear value of 8 mPa at a constant inlet velocity = 44.2 μm/s. However, the accuracy of this model was limited by the 2D domain.

With the development of μCT being applied to tissue engineering scaffold imaging and quantification (Jones *et al.* 2007; Singh *et al.* 2010), the simulation of flow in 3D constructs with real pore architectures improved dramatically (Maes *et al.* 2009; Raimondi *et al.* 2005; Raimondi *et al.* 2006). Raimondi *et al.* (Raimondi *et al.* 2006) applied a commercial finite volume CFD code (available in FLUENT) to predict the shear stress based on a partial volume of the scaffold from μCT images. The level of hydrodynamic shear stress acting on the outer surface of the internal spherical pores (nominal pore size 100 μm) was estimated at different construct inlet velocities (72-884 μm/s) and the magnitude was calculated to be in the range 4.6 – 56 mPa. These results suggested a strong correlation between the hydrodynamic shear and the invoked biosynthetic response in chondrocyte systems. Porter *et al.* (Porter *et al.* 2005) used 3D Lattice Boltzmann (LB) simulations to investigate the flow in cylindrical scaffolds as a function of flow rates. The shear stress was calculated using a finite difference formula for each fluid element in the LB model. They found an average shear stress of 0.05 mPa was required to have stimulating effect on cell proliferation, and that higher shear stress would lead to subsequent upregulation of bone growth. It was also claimed that a peak shear stress greater than 57 mPa would have detrimental effect such as cell death within the constructs.

Cioffi *et al.* (Cioffi *et al.* 2006) used the finite volume CFD model based on the work produced by Raimondi *et al.* (Raimondi *et al.* 2006) to evaluate the shear stress acting on scaffold walls based on higher resolution μCT images of a polyester urethane scaffold with spherical pores of nominal size 100 μm. Various flow rates were simulated in this model and the calculated shear stresses varied between 0 and 40 mPa over the scaffold surfaces. They found in their models that the average wall shear stress increased linearly with the flow rate. The same group then developed a combined macro-scale/micro-structured model to investigate the effect of the flow rates and scaffold microstructures on shear stress and oxygen consumption rates in the central region of the scaffold (Cioffi *et al.* 2008). Their model suggested that a flow rate of 0.3 ml/min, at which 95% of the scaffold surface area experienced shear stresses less than 6.3 mPa, would maintain the oxygen supply above the anoxic level. While μCT has allowed significant improvements in capturing geometric effects on flow, these

have yet to be coupled with time dependent simulation of the influence of cellular parameters, such as growth rate, deposition, and the resultant time dependant porosity change. All these issues are crucial to the correlation of fluid induced shear stress and cellular growth.

Some models took the cell proliferation and nutrient consumption into account when they simulated the perfusion system. Chung *et al.* (Chung *et al.* 2007) incorporated the nutrient mass transport by using an equation modelling the cell mass conservation. The flow model was based on the Brinkman's equation for porous media which has predicted a macroscopic average shear stress with a 5-fold increase in correlation to cell growth. Recently, Liu *et al.* (Liu *et al.* 2012) presented a similar model which assumed the growth of cells to be evenly distributed in space and predicted the macroscopic average shear stress at the local flow regions. The model estimated a 10-fold increase in the flow rate (0.02 to 0.2 mm/s) caused the shear stress to increase by 10 times and suggested higher flow rate would be beneficial to more cellular growth. Lesman *et al.* (Lesman *et al.* 2010) considered the effect of time dependant cellular growth inside the porous microstructure on the shear stress by adding cell-layers of constant thickness onto the pore periphery, which however in reality, greatly depends on local shear stress acting on the cells. All of the prior studies focused on macroscopic shear stress predictions.

The above-mentioned studies used various CFD approaches to numerically simulate the perfusion system and evaluated the average wall shear stress either on the surface or on the inner pore surface of the construct. However, there has not been a comprehensive study on the ***local*** shear stress effect on bone cell ingrowth which inter-relates time dependant microscopic flow simulation with flow-induced shear stress distribution on a microscopic level. This is an important aim of this thesis.

3 Simulating the Flow Properties of Additive Manufactured Titanium Implants – Influence of Strut Architecture and Permeability*

In this chapter, flow properties of Ti implants produced by the SLM technique were simulated based on 3D μCT images. Design factors such as porosity, strut ordering and surface roughness offered by the SLM technique are used to alter the implant architecture on multiple length scales to control and tailor the flow. Using experimentally validated CFD simulations, this chapter demonstrates how additive manufacturing can be used to hierarchically tailor the permeability of implants by controlling the surface roughness at a microstructual level (microns), and by altering the strut ordering and the density at a macroscopic level (millimetre).

3.1 Introduction

Porous Ti implants are a common choice for bone augmentation. As reviewed in Chapter 2, implants for joint replacement and repair of non-union fractures must encourage both body fluid and blood flow after implantation so that there is sufficient cell migration, nutrient and growth factor transport to stimulate bone ingrowth. Permeability is a measure of the ease with which liquid flows through a porous structure under a pressure gradient and is a convenient way to characterise the bulk flow. In addition to flow, permeability can also be related to the internal topology of foams, the porosity, and the surface roughness of the foam struts.

---

*Note, a large portion of this chapter is now published as:

Zhang Z., Jones, D., Yue, S., Lee P.D., Jones, J.R., Sutcliffe C.J., Jones E., Hierarchical Tailoring of Strut Architecture to Control Permeability of Additive Manufactured Titanium Implants, Materials Science and Engineering: C Materials for Biological Applications, 2013.

Additive manufacturing techniques such as SLM technique (Mullen *et al.* 2009; Mullen *et al.* 2010) can provide control over both percentage porosity and the interconnected network of the structure. In this chapter, open-cell Ti foams were produced from CP-Ti powder using SLM. Two types of the structure, regular and irregular, are investigated.

Performing computational modelling of fluid flow using CFD codes overcomes many experimental difficulties and allows direct design and tailoring of permeability. Previous literature regarding permeability (Kohles *et al.* 2001; Nauman *et al.* 1999; Ochoa *et al.* 2009; Shimko *et al.* 2005; Singh *et al.* 2009), as reviewed in section 2.4.2, does not address how the changes in the structural design influence implant permeability. Furthermore, how they may be tailored to have the desired flow properties has not been studied previously.

The aim of this study is primarily to determine how each SLM variable, such as pore structure randomness, percentage porosity and surface topography, affects permeability. The goal is to derive relationships which allow the independent tailoring of the permeability to optimise the design of implants. First, an experimentally validated computational approach for the evaluation of permeability was applied to a range of samples produced by the SLM process with structures modified during the manufacture process. Structural modifications were then made on the computer design of Ti structures at both microscopic (surface roughness) and macroscopic (strut architecture) levels. How the design factors can be used to alter to control and tailor the flow is discussed based on the CFD results.

3.2 Materials and Methods

3.2.1 Ti Foam Preparation

Samples were produced from CP-Ti (Grade 1) metal powder (Sumitomo, Japan) by SLM using an MCP Realizer 2, 250 SLM system (MTT, UK). The full manufacturing process has been detailed by Mullen *et al.* (Mullen *et al.* 2009; Mullen *et al.* 2010). The samples were constructed using the Unit Cell (UC) approach (Mullen *et al.* 2009) which comprises the following sequences:

i. A CAD model of the porous structure was built using the Manipulator© software (version 4.7) suite (University of Liverpool, UK). The 3D geometries were completely filled with cubic unit cells of a single defined

edge length. All UCs were filled with a connected lattice structure by joining sets of points and vectors in 3D space to form regular octahedra (this geometrical shape allows tessellation).

ii. To produce the 'irregular' structures, a randomisation process based upon perturbation of the Cartesian coordinates of each vertex of the UC while maintaining connectivity. The displacement of each node is generated using a random number generator and the boundary values for the range of randomisation are defined as a specific percentage of the UC size (Mullen *et al.* 2010). For example, a 30% randomisation based on a UC size of 10 mm will change the point [0, 0, 0] to [3, 0, 0] or [-3, 0, 0]. (Note that the structures produced are in fact pseudo-random as the randomness is fully reproducible.)

Both the regular and irregular structures form completely open porosity that is fully connected to the surface.

The points and vectors were trimmed to the CAD file of the cylinder, and then sliced (50 µm intervals) to produce a set of points on all layers, de-noting the firing position of the scanning laser. These locations, together with the laser properties (beam diameter, dwell time and energy), determine the strut diameter (references (Mullen *et al.* 2009) and (Mullen *et al.* 2010) provide details of the SLM process). Upon completion, the parts were removed from the argon atmosphere build chamber, wire electro-discharge machined (EDM) from the substrate plate and cleaned of all un-fused powder, after which a sintering operation was carried out under vacuum at 1400˚ C for 3 hours to heat treat the parts.

In this study, cylindrical samples of equal diameter and height of 4 mm with 4 levels of randomness were produced. Samples evaluated were nominally 65% porous, with a UC size of 600 µm (named as UC600) and were produced with 0, 10, 20 and 30% randomisation, with the sequential operation being illustrated in Figure 3-1.

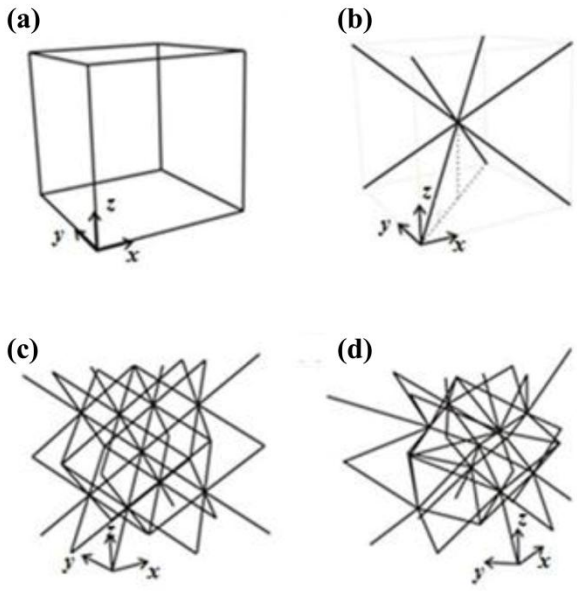

Figure 3-1 The UC approach: unit cell transformation from (a) a cube to (b) an octahedron, to (c) a tessellated octahedral wireframe structure, and finally to (d) a pseudo randomised structure.

3.2.2 µCT and Image Processing

The smaller cylindrical samples were scanned at a resolution of 9 µm per voxel using a commercial µCT unit (Phoenix v|tome|x, GE Measurement and Control, MA, USA). The X-ray tube voltage and filament current were fixed at 100 kV and 70 µA, respectively. A copper filter of 0.5 mm thickness was used to absorb low energy X-rays and reduce beam hardening (Stauber and Muller 2008). A rotation step of 0.5^{o} was set within an angular range of 360^{o}. After acquiring the 2D radiographic images, 3D volumes of 512 × 512 × 512 $voxel^{3}$ for all samples were then reconstructed using the commercial reconstruction software datos|x (GE Measurement and Control, MA, USA). Pre-processing of the 3D volume, including a 3 × 3 × 3 median filtering, and removing islands within the volume space was accomplished using a commercial image visualisation/analysis software Avizo 5 (VSG, MA, USA) and in-house developed codes (Atwood *et al.* 2004; Jones *et al.* 2007).

3.2.3 Structure Characterisation

The average strut diameter was measured to be 180 µm using SEM (JOEL JSM 700 1F (JOEL Ltd, Japan)) by Dan Jones (University of Liverpool), see Figure 3-2.

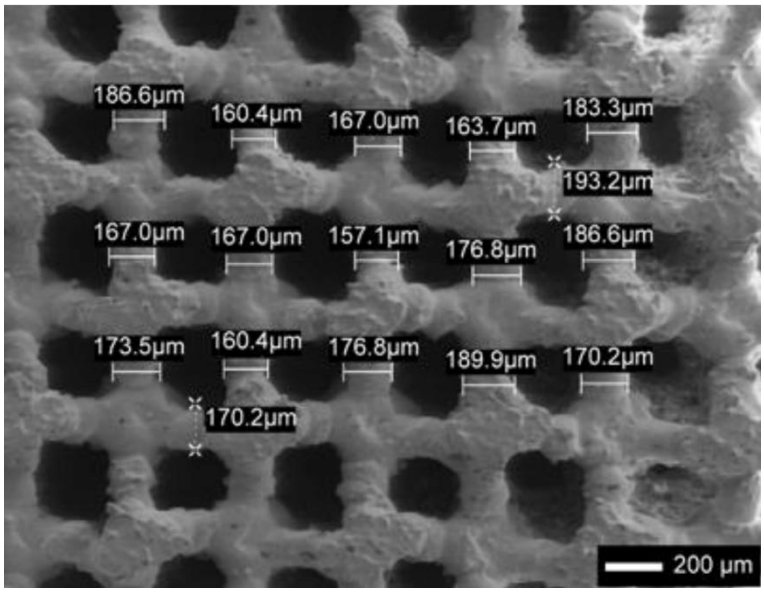

Figure 3-2 Strut diameter of UC 600 regular structure measured from SEM. (Figure courtesy of Dan Jones, University of Liverpool)

True porosity calculations and pore size distribution characterisation were carried out based on the µCT images using the 'Accessible Pore Volume' method developed in-house by Sheng Yue (Yue 2011). The general idea of this method is to mimic the Mercury Intrusion Porosimetry (MIP) method. A sphere kernel with a specific radius is pushed through connected channels from the surface and the percentage of void space within the structure that can be filled by the sphere is calculated. A range of accessible volumes corresponding to different radii is then obtained and the pore size distribution can be calculated as the differential of the area under the accessible volume percentage curve. The structural results evaluated based on the µCT images were compared to the gravimetric analysis (Adam Equipment, UK, balance accuracy ±0.01 g and digital callipers accuracy ±0. 2 mm) and MIP data (AutoPore IV 9500), respectively (Mullen *et al.* 2010).

3.2.4 Structural Modifications on the CAD Volume

Computational algorithms were developed to modify foam structures, so that strut diameter and strut surface morphology could be controlled computationally, both of which can alter the surface area per unit volume.

The SLM input file containing the coordinates of the laser melting nodes, which depict the building process of the Ti foams, was voxelised using bespoke convolving codes developed in-house. The melting nodes were first located and a perfectly spherical

kernel was then chosen to perform convolution on these nodes throughout the volume. Note that for a perfectly spherical convolving kernel, which is symmetrical in all directions in the 3D space, the convolving process can be achieved by a simple distance transform dilation process. For example, to form a strut with a diameter of 180 µm, any voxel (e.g. voxel size = 5 µm) with a distance less or equal to 18 from the melting node would be labelled as the strut voxel. This is equivalent to convolve using a spherical kernel of a radius of 90 µm to form the struts phase. By changing the dilation distance value, foams with different strut thickness were created. In this study, 4 regular Ti foams were created with strut thickness of 120, 180, 240 and 300 µm, respectively, as shown in Figure 3-3.

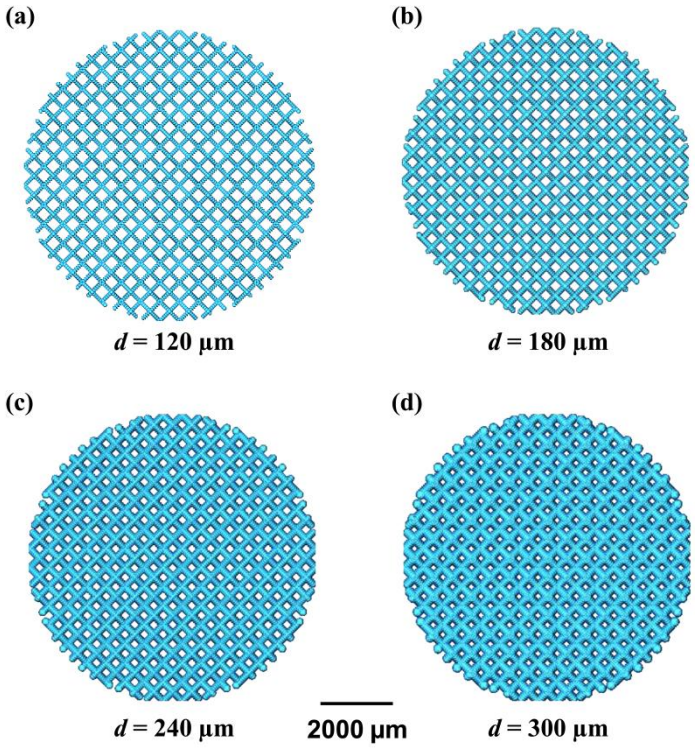

Figure 3-3 *xy*-plane view of regular foams with different strut diameters (volume rendered directly from the CAD file): (a) 120 µm; (b) 180 µm; (c) 240 µm; (d) 300 µm.

To design foams with different surface morphologies, the cubic UCs were filled using three different lattice structures to form the octahedron shapes. The shape of the lattice structure was controlled by Equation 3-1 in the cylindrical coordinates system. The strut surface morphology was controlled by changing the coefficient a in the equation:

$$r = 1 + 0.3sin(a\pi z) + 0.3sin(6\varphi) \qquad \textbf{3-1}$$

(r, z, φ) is the cylindrical coordinates of a point position, where r represents the radius of the strut, z is the length of the strut and φ is the angle between a reference direction on the cross-sectional plane of the strut and the line from the origin to the projection of a point on the plane. Figure 3-4 shows examples of voxelised struts with different surface morphology.

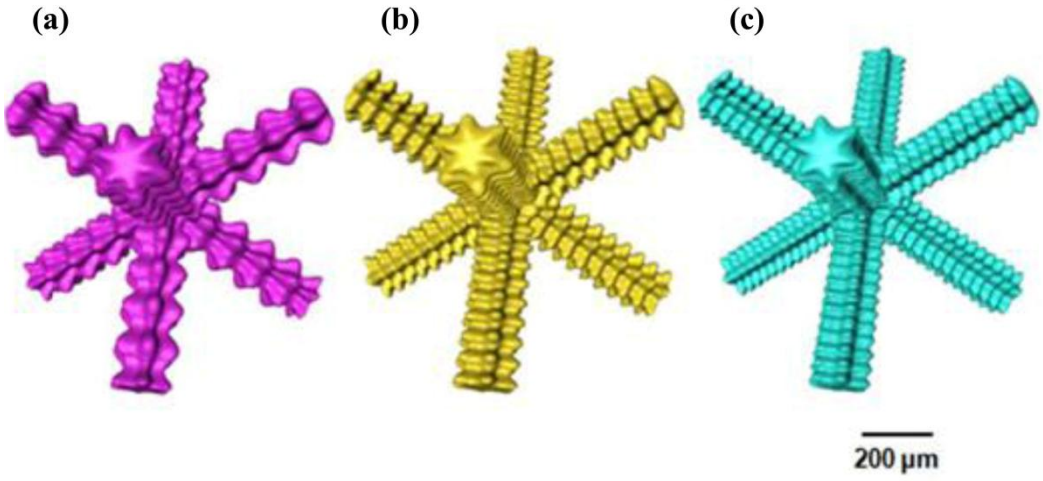

Figure 3-4 Struts designed with different levels of strut surface roughness, by setting the coefficient, *a*, to be: (a) 0.1; (b) 0.2 and (c) 0.3.

3.2.5 Permeability Measurements

The experimental assessment of permeability was performed by Dan Jones using a simple pressure head system developed at University of Liverpool, UK. Samples of cylindrical shape (diameter and length 10 mm, with a solid outer wall of thickness 0.5 mm) were used. A small pressure head (less than 60 mm) of fluid was used to produce flow rates through the structure corresponding to 0.01 m/s. Absolute methanol was used in the experiment in order to give more consistent results owing to its reduced surface tension with the Ti foam. Prior to being loaded into the experimental set-up, the foams were stored in the fluid to ensure complete wetting and removal of trapped air. A minimum of 6 readings were taken for each sample with 0 – 30% randomness along z-direction (foam building direction), with the flow being allowed to stabilise prior to commencing the experiment. The pressure head and fluid flow rates were measured using a Vernier gauge (accuracy 0.02 mm) and a stop clock (accuracy 0.2 s) respectively for periods up to 5 minutes to maintain accuracy at the low flow rates. Permeability was determined graphically using the Darcy and Dupuit-Forchheimer equations.

3.2.6 CFD Model Theory

3.2.6.1 The Governing Equations

The fundamental basis of CFD simulations is the Navier-Stokes equation (N-S equation), which is obtained based on the fundamental equations of fluid dynamics. There are three basic equations of fluid dynamics, resulting from the following universal laws of conservation (Tannehill *et al.* 1997):

i. Conservation of Mass
ii. Conservation of Momentum
iii. Conservation of Energy

These three basic equations can be expressed as PDEs based on applying the conservation laws on an infinitesimal control volume of fluid either fixed in space or moving with the flow. Since the equation which states the Conservation of Energy will only be required when it involves heat transfer or in the case where density of the fluid varies, only the first and second governing equations are discussed below.

Applying the Conservation of Mass law to an infinitesimal, fixed control volume of the fluid results the first fundamental equation called the continuity equation (Tannehill *et al.* 1997):

$$\frac{\partial \rho}{\partial t} + \nabla \cdot (\rho \boldsymbol{u}) = 0 \qquad \textbf{3-2}$$

where ρ is the fluid density, t is the time and $\boldsymbol{u}$ is the fluid velocity.

It is convenient to use the substantial derivative to change Equation 3-2 into the form

$$\frac{D\rho}{Dt} + \rho(\nabla \cdot \boldsymbol{u}) = 0 \qquad \textbf{3-3}$$

For an incompressible flow, ρ is a constant, therefore reducing Equation 3-3 to

$$\nabla \cdot \boldsymbol{u} = 0 \qquad \textbf{3-4}$$

The second governing equation of fluid dynamics, the momentum equation, is obtained by applying the Conservation of Momentum law to an infinitesimal, stationary controlled volume through which fluid flows and by Newton's Second Law (Tannehill *et al.* 1997):

$$\frac{\partial(\rho \boldsymbol{u})}{\partial t} + \nabla \cdot (\rho \boldsymbol{u}\boldsymbol{u}) = -\boldsymbol{\nabla} P + \mu \nabla^2 \boldsymbol{u} + S \qquad \textbf{3-5}$$

where P is the pressure, μ is the dynamic viscosity and S is a source term representing the external force.

Assuming the flow is incompressible, the N-S equation can be obtained:

$$\frac{\partial(\rho \boldsymbol{u})}{\partial t} + \rho \boldsymbol{u} \cdot \nabla \boldsymbol{u} = -\boldsymbol{\nabla} P + \mu \nabla^2 \boldsymbol{u} + S \qquad \textbf{3-6}$$

3.2.6.2 Finite Volume Method (FVM)

In all CFD numerical methods, it is essential that the flow governing equation (typically the N-S equation) is approximated by algebraic equations which give values at a finite number of discrete points / volumes in some domain (Anderson 1995). This process is called the 'discretisation' in CFD methods. As reviewed in section 2.4.2, the finite volume method (FVM) (also called control volume method) is one of the common approaches to discretise the N-S equation in commercial CFD software codes.

FVM consists of (1) dividing the domain of interest into small control volumes and then (2) integrating the flow governing equation about each volume, yielding a discretised equation on a control-volume basis.

The flow governing equation (Equation 3-5) can be rewritten as a generic equation for transport of an arbitrary variable φ:

$$\frac{\partial(\rho \varphi)}{\partial t} + \nabla \cdot (\rho \varphi \boldsymbol{u}) = \boldsymbol{\nabla} \cdot (\mathrm{r} \boldsymbol{\nabla} \varphi) + S_\varphi \qquad \textbf{3-7}$$

where **r** is the diffusion coefficient for φ.

Over a control volume V, the integration form of Equation 3-7 takes the form:

$$\int_V \frac{\partial(\rho \varphi)}{\partial t} dV + \int_V \nabla \cdot (\rho \varphi \boldsymbol{u}) dV = \int_V \boldsymbol{\nabla} \cdot (\mathrm{r} \boldsymbol{\nabla} \varphi) dV + \int_V S \varphi \, dV \qquad \textbf{3-8}$$

By Divergence Theorem, Equation 3-8 is:

$$\int_V \frac{\partial(\rho \varphi)}{\partial t} dV + \int_A (\rho \varphi \boldsymbol{u}) \cdot \underline{n} dA = \int_A (\mathrm{r} \boldsymbol{\nabla} \varphi) \cdot \underline{n} dA + \int_V S \varphi \, dV \qquad \textbf{3-9}$$

where V is the control volume, $\underline{n}$ is the vector normal to the surface dA (Figure 3-5).

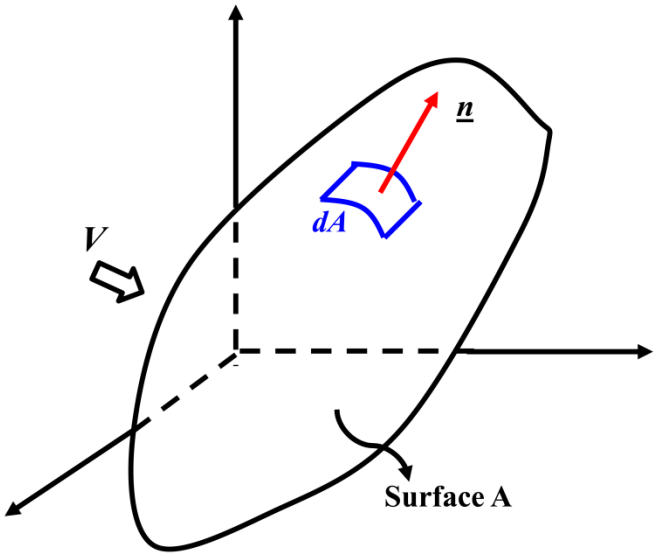

Figure 3-5 Sketch of finite volume *V*, and infinitesimal surface element *dA* with normal vector *n*.

Equation 3-9 is then applied to each finite volume in the domain and the discretisation of the equation gives:

$$\frac{\partial(\rho\varphi)}{\partial t}V + \sum_{f}^{N} \rho_f \boldsymbol{u}_f \varphi_f A_f = \sum_{f}^{N} \Gamma_f \nabla\varphi_f A_f + S_\varphi V \qquad \textbf{3-10}$$

where N is the number of faces enclosing the finite volume/cell, A_f is the area of the face f, φ_f is the value of φ convected through face f, $\nabla\varphi_f$ is the gradient of φ at face f, ρ_f $\boldsymbol{u}_f A_f$ is the mass flux through the face f.

This discretisation scheme can be applied to obtain the discretised momentum and continuity equation, which can be solved to obtain the velocity field.

3.2.7 CFD Model Theory – Permeability Simulation

Permeability was determined using the commercial CFD package FLUENT (Version 6.3.26, ANSYS, Inc., PA, USA) using the finite volume method to solve the N-S equation assuming incompressible flow.

The simulation includes the following operations:

i. Segmentation of the empty space (void region with the fluid flow) and solid Ti struts by thresholding the 3D volume based on the histogram using ScanIP software (Simpleware Ltd., Exeter, UK).

Choosing an optimum threshold value is an important step in the image-to-model process. It has direct impact on the accuracy of the porosity estimation. In this study, the thresholding is also called binarisation process as there are only two phases (solid Ti phase and void phase) that need to be separated. To binarise the image, a simple global threshold was used. The threshold value was chosen from the voxel intensity histogram of the image, equidistant between the two peaks corresponding to the Ti phase and void phase (Figure 3-6).

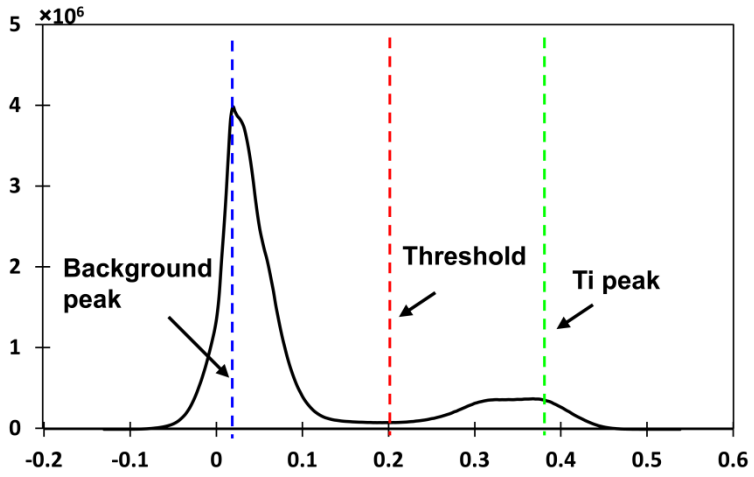

Figure 3-6 A typical histogram of the image: the threshold value is determined by finding the equidistant value between the two peaks corresponding to the Ti phase and void phase.

ii. An entirely fluid region of 720 µm in length, which is 10% of the total length of the test structure, was added both up and down stream to act as a diffuser and to allow the flow to stabilise on the upwind and downwind flow faces (procedure followed from a previous similar work done by the group (Singh *et al.* 2010)). (See Figure 3-7 Region A and B).

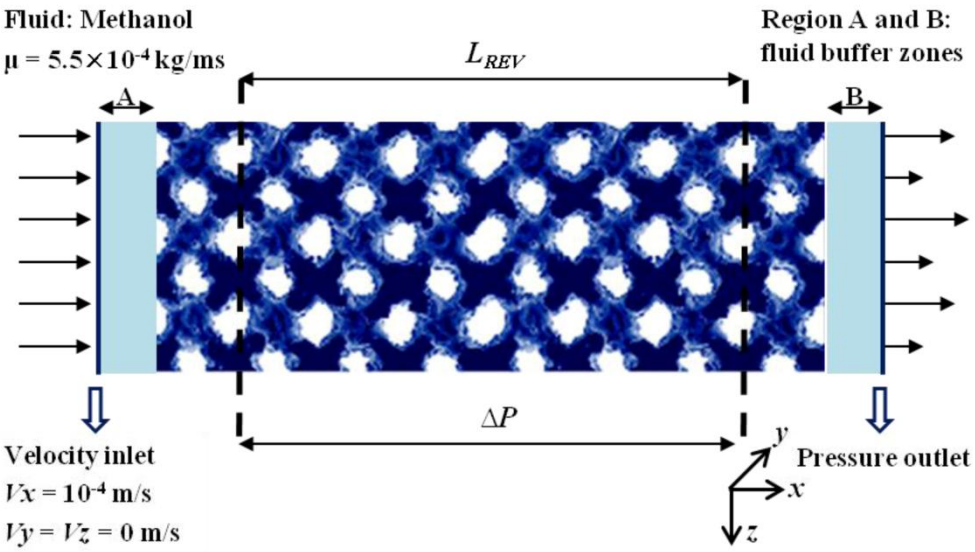

Figure 3-7 Schematic of the permeability derivation in the *x* direction, showing the boundary conditions applied.

iii. Up / down-wind end faces of the model in the desired flow direction were set as fluid inlet/outlet boundaries.

iv. The finite element tetrahedral mesh of the fluid flow regions was created using ScanFE software (Simpleware Ltd., Exeter, UK).

A mesh size of 18 μm was chosen to keep the total number of elements less than 5 million while ensuring the accuracy of the model. Change in result was within 1%. Convergence test was performed using the regular structure (0% randomness) with mesh sizes of 9, 18 and 36 μm (Figure 3-8).

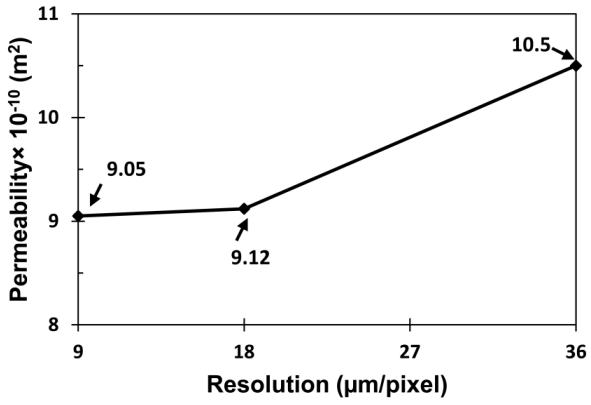

Figure 3-8 Convergence test on different mesh sizes: mesh size of 18 μm was chosen to achieve both accuracy of the model and the computational efficiency.

v. The model was then imported into FLUENT. Boundary conditions and fluid properties were set as follows (also shown in Figure 3-7):

   a. A constant inlet flow velocity of 10^{-4} m/s was applied across the entire upwind face.

   b. A zero velocity boundary condition was set on the 4 faces normal to flow.

   c. A free pressure outlet boundary condition was set on the downwind face.

   d. No-slip wall condition was set on surface of struts.

   e. The fluid properties were set to methyl alcohol liquid (CH_3OH), as used in the experiments, with a density of 7.85×10^{2} kg/m^3 and viscosity of 5.495×10^{-4} kg/ms. Note that the Reynolds number, *Re*, was << 1 (around 0.06) to ensure that the flow is in the laminar regime and it is valid to apply Darcy's Law (Despois and Mortensen 2005).

The model was then run using the conjugate gradient solver until the normalised residual was reduced to 10^{-6}. After a converged solution was reached, the following steps were performed to calculate the effective permeability:

vi. Multiple surfaces normal to the flow direction were set and the average pressure across these surfaces was then determined. The variation in pressure across the model in the flow direction was then plotted to find the pressure gradient ($\Delta P/L$) (Figure 3-9). Note that only the region in between the two dashed lines, L_{REV} shown in Figure 3-7 where the flow was stabilised was included in the calculation of the pressure gradient. For all simulations, the pressure gradient was calculated between the two surfaces located 1.4 mm from the inlet and outlet ends.

The size of the representative elementary volume (REV) was selected by growing the REV until a stable permeability was reached. The volume which gives the final stabilised result was then denoted as the smallest volume required being representative of the bulk property, or minimum REV. For more details on REV, see reference (Gitman *et al.* 2007).

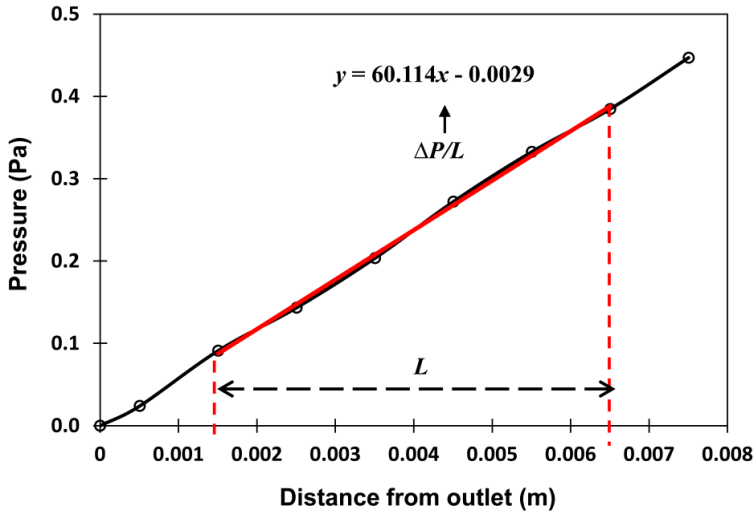

Figure 3-9 A typical curve is shown for calculating the pressure gradient in the stable flow region (marked as red line).

vii. Darcy's Law (Equation 2-5) was then applied to calculate the Darcian permeability.

3.3 Results

3.3.1 Structure Characterisation

Table 3-1 shows the porosity of Ti foams with randomisation levels of 0, 10, 20 and 30%. The estimated porosities based on µCT images show 2.3 – 10.3% higher values compared to the measured porosity by the gravimetric analysis. Note that the porosity was calculated based on µCT images with the original resolution of 9 µm per voxel and the histograms for all scans were normalised prior to choosing the threshold.

Table 3-1 Porosities of Ti foams measured by gravimetric analysis (Data provided by Dan Jones, University of Liverpool) and estimated based on the 3D µCT images.

Unit Cell Size (µm)	Randomisation (%)	Target Porosity (%)	Gravimetric Porosity (%)	Porosity based on µCT (%)
600	0	65	63.8 ± 0.2	67.4
600	10	65	63.4 ± 0.3	69.9
600	20	65	66.2 ± 1.0	67.7
600	30	65	64.7 ± 0.2	67.5

Figure 3-10 (a) shows the pore distribution of each sample estimated by the accessible volume method based on 3D µCT scans. The mode value of pore diameter increases

from 203 to 302 µm, and the distribution widens as the randomisation level increases. These are compared to Figure 3-10 (b), which shows the experimental data on the same set of samples. The mode values of measured pore diameter are in the range of 225 to 281 µm. The pore size distribution obtained from the µCT quantification matches with the experimental results.

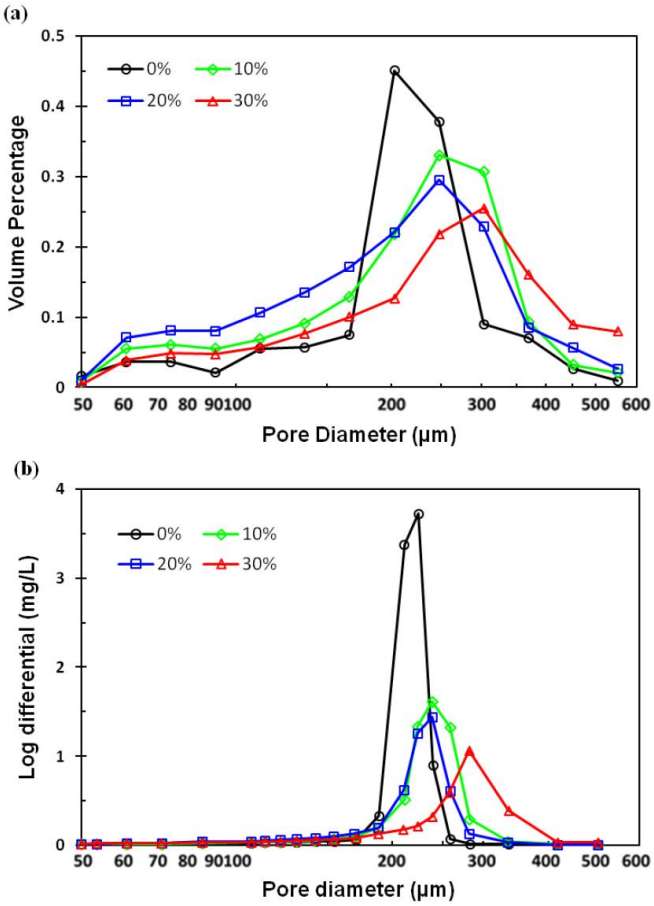

Figure 3-10 Pore size distributions of UC600 samples at 0, 10, 20 and 30% randomisation measured using (a) accessible volume method based on µCT images and (b) mercury intrusion porosimetry. (Figure (b) modified from Mullen *et al*. (Mullen *et al.* 2010))

SEM images of the UC600 with increasing randomisation of 0, 10, 20 and 30% are shown in Figure 3-11. This allows a detailed understanding of how the structures changed with randomising the regular lattice. These modifications to the structures can be seen in the longitudinal view of µCT scanned images (Figure 3-11 left). The internal pore structure can be seen to be strongly affected by the randomisation. The illustrations show that the perturbation of the strut coordinates forming the octahedral shape by the specified amounts in the *x*, *y* and *z* directions were significant in changing both the appearance and the pore characteristics of the structures.

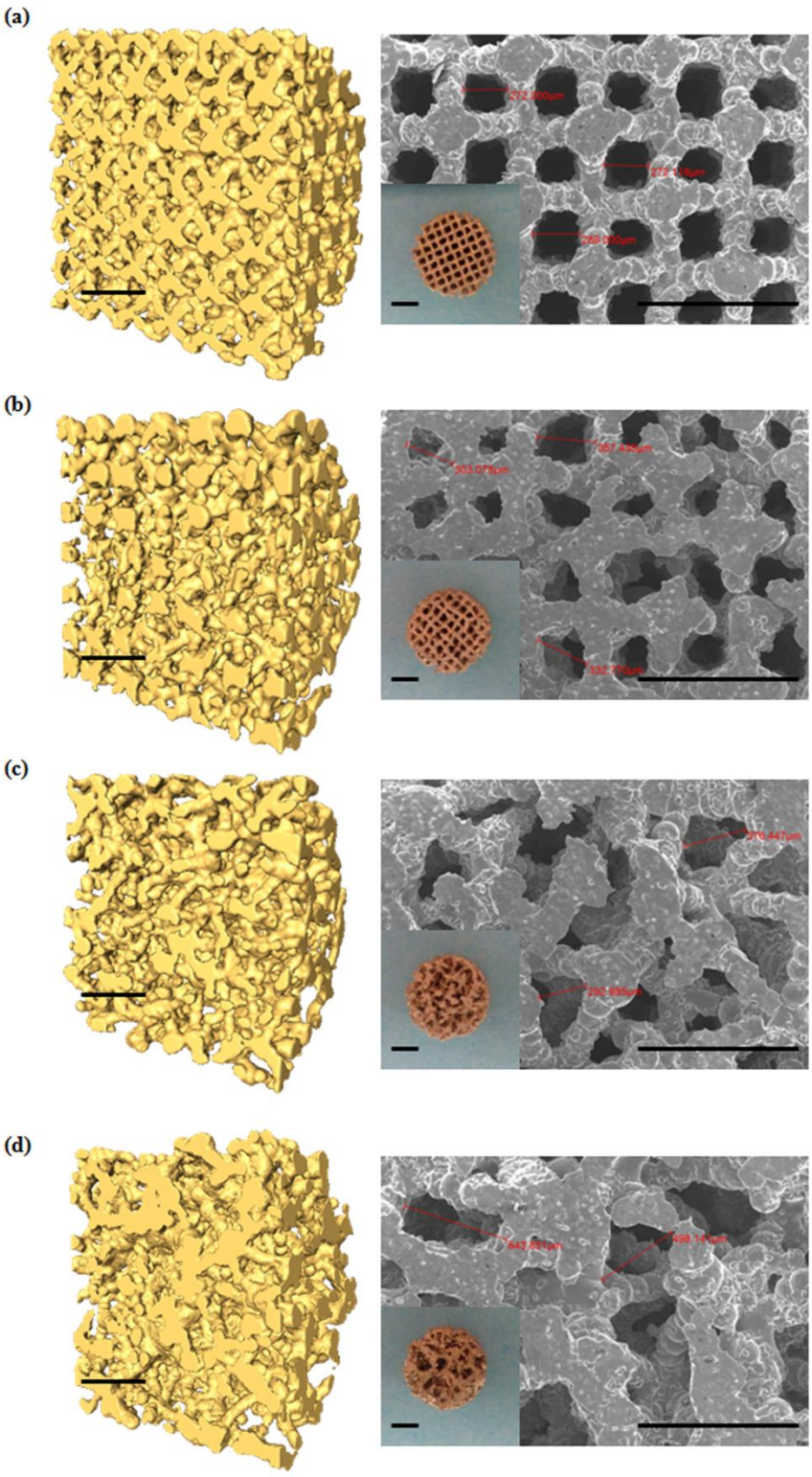

Figure 3-11 Left: Rendering of µCT volumes of unit cell size 600 µm at (a) 0%, (b) 10%, (c) 20%, and (d) 30% randomness level. Right: SEM images of Ti implants produced by SLM at (a) 0%, (b) 10%, (c) 20% and (d) 30% randomness level. (SEM images courtesy of Dan Jones, University of Liverpool) Real Ti implants produced by SLM shown on the bottom right corners of each µCT images. All scale bars represent 1000 µm.

3.3.2 Permeability Prediction

With µCT imaging, direct computation of permeability from real 3D microstructures should provide both an accurate value for permeability and a tool to tailor permeability to requirements. The CFD approach simplifies the N-S equation by assuming stationary, incompressible flow, and that the viscous drag has a linear relationship with fluid velocity. The Reynolds number has a very low value (Re << 1), which ensures the flow regime is laminar. With these assumptions, Darcy's Law is applicable for permeability calculations (Despois and Mortensen 2005). It was determined by a sensitivity study that the REV lengths were significant, and the attainment of steady state flow conditions differed with respect to the randomness of the structure. Figure 3-12 shows two such structures (0% and 30% randomised) illustrating this point, and also shows that the permeability of foams is anisotropic. For ease of calculation, a single REV length, 4.2 mm was used for all test cases.

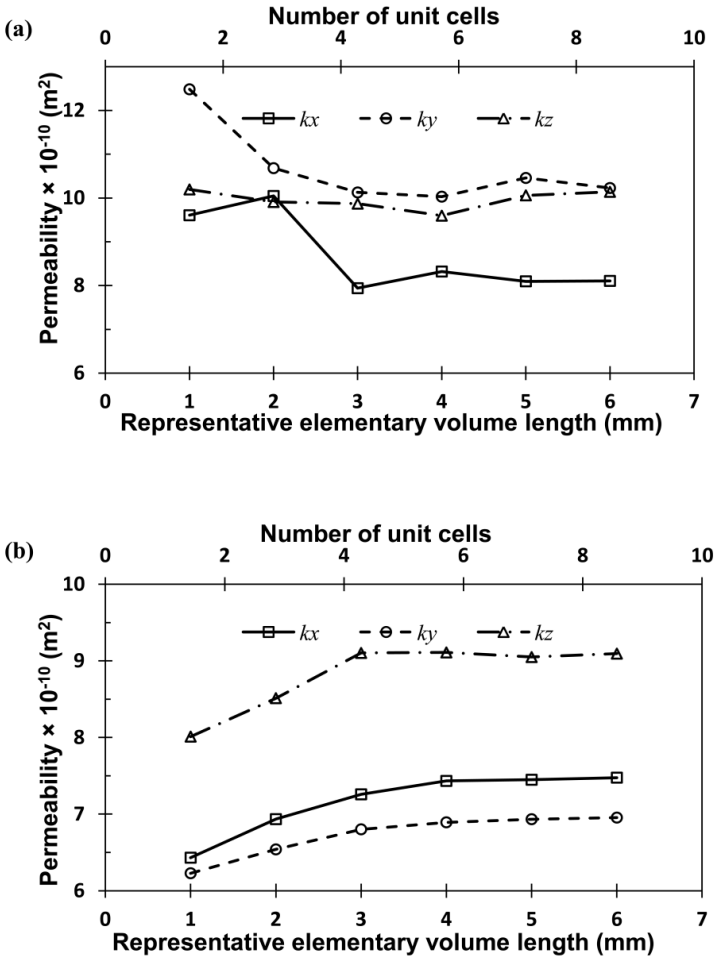

Figure 3-12 Permeability of regular (0% randomness) and 30% randomised structures versus representative elementary volume lengths of unit cells.

The permeabilities calculated for all structures are presented in Table 3-2, and show that anisotropy increases as the structure is randomised, with the regular sample showing a narrow range of change. The experimentally measured values for both the Ti foam and human cancellous bone are also shown (Kohles *et al.* 2001). Simulations were performed directly on both μCT scans of real SLM manufactured samples and the voxelised computer aided design (CAD) models (i.e. design of the foam structure to be used as the input in the SLM manufacturing process).

Table 3-2 CFD predicted permeability in *x*, *y* and *z* direction via CFD simulation using the μCT data and voxelised CAD design volume. Experimental results and measurement of permeability in bone are also shown.

Direction	CFD predicted permeability ($\times 10^{-10}$ m^2), K			
	0%	10%	20%	30%
x	7.2 ± 0.6	8.8 ± 1.3	7.7 ± 1.0	8.1 ± 0.9
y	7.0 ± 0.5	9.0 ± 1.6	6.9 ± 0.7	9.5 ± 1.2
z	9.1 ± 0.1	8.6 ± 1.3	8.5 ± 0.6	10.2 ± 0.6
Average	7.8 ± 0.4	8.8 ± 1.4	7.7 ± 0.7	9.3 ± 0.5
Experimental (*z*-direction)	9.9 ± 0.1	8.9 ± 0.1	7.1 ± 0.1	8.8 ± 0.1
CAD model	8.9 ± 0.2	7.9 ± 0.4	7.3 ± 0.3	9.2 ± 0.3
Bone	1.2 to 80.5 reviewed by Kohles *et al.* (Kohles *et al.* 2001)			

A comparative plot of results obtained by experiment and simulation techniques is shown in Figure 3-13. Average permeability value of repeated measurements for each sample is plotted with the error bar representing the standard deviation. CFD simulations were performed on 3 child volumes selected at different locations within each sample and the average value of permeability was calculated. The error bar represents the standard deviation. The plots show that generally there is a good agreement in the two approaches, in that the values are within 17%, and also demonstrate that randomness does not significantly affect the bulk flow.

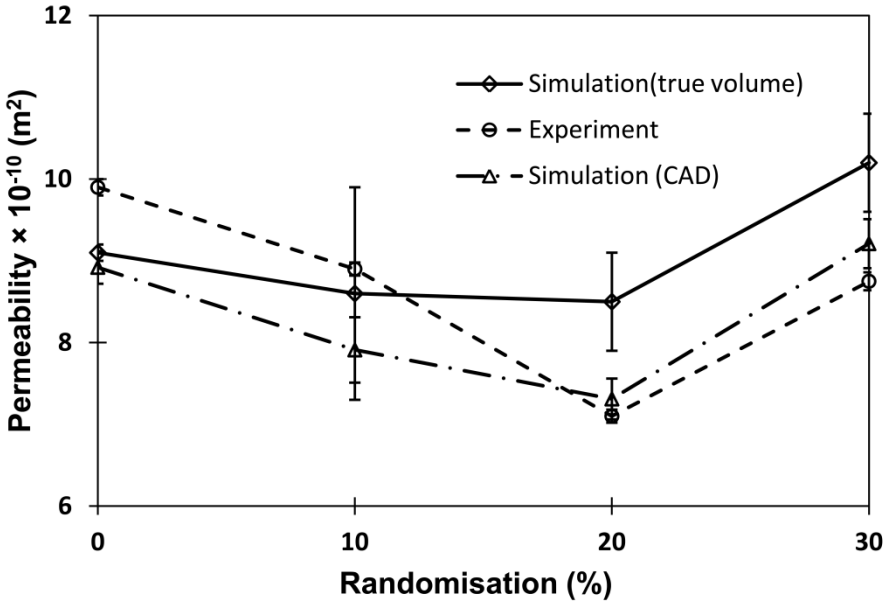

Figure 3-13 A comparative plot of permeability predicted in the *z* direction by using CFD simulation models and experimental measured values.

3.3.3 Effect of Structural Parameters on Flow Property

By running permeability simulations for both the voxelised 0% and 30% randomised foams, the localised velocity profiles of flow through implants with different internal structures can be visualised (Figure 3-14). In the 30% randomised structure compared to the 0% randomised structure, the minimum velocity was found to be 8.41×10^{-5} m/s compared to 3.74×10^{-5} m/s respectively, which was an increase of 56%. The maximum velocity of fluid in the 30% randomised structure was 1.68×10^{-3} m/s compared to 7.49×10^{-4} m/s in the 0% randomised structure, which had an increase of 50%. Preferential flow channels form much more easily in the random structure foams due to greater variations in channel width and pore size compared to the uniform channel size in the regular structure, giving a much greater range of local shear in the flow, which has been shown to stimulate tissue growth (Kapur *et al.* 2003; Sikavitsas *et al.* 2003). Detailed study of the effect of the flow shear stress on bone ingrowth will be discussed in Chapter 5.

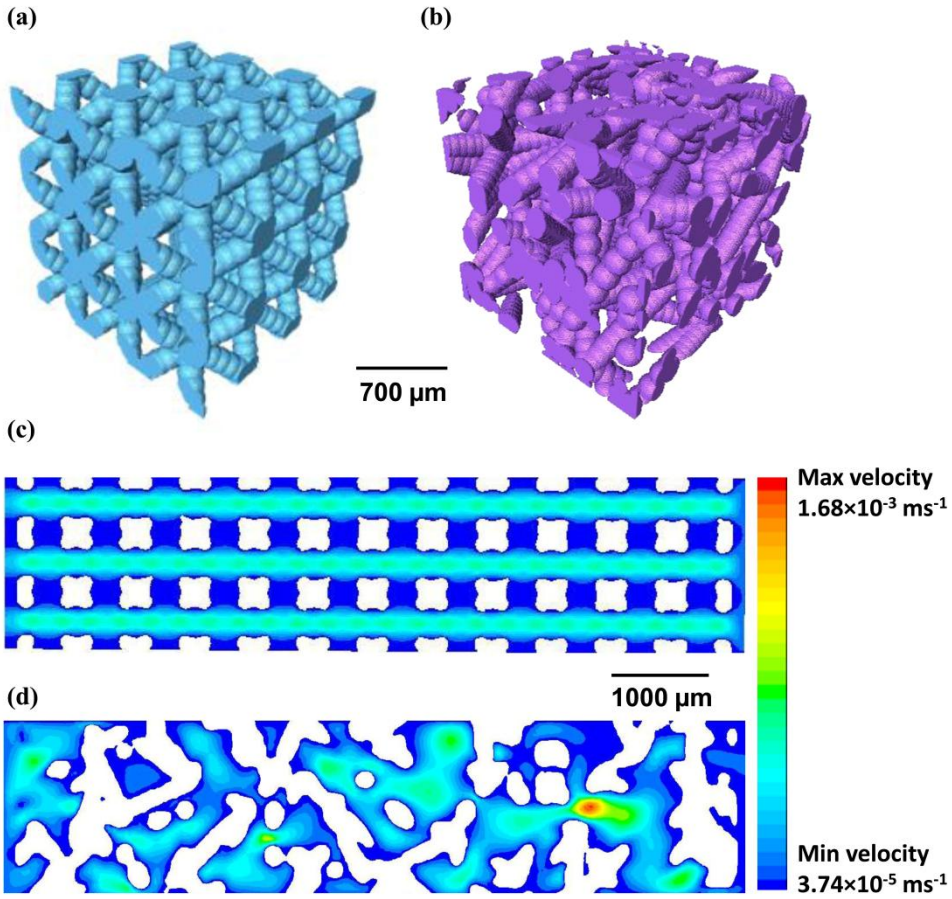

Figure 3-14 Voxelised 3D child volumes of (a) regular and (b) 30% randomised scaffold structures. Flow velocity profiles of same scale in Ti foams (regular, (c) and 30% randomised structure, (d)). Red represents the highest velocity.

Voxelisation of the 3D foam structures allows the thickness/diameter of the Ti struts to be computationally changed to compare the effect of strut thickness on permeability. The effect of altering strut thickness on permeability is shown as a function of porosity in Figure 3-15 (a). Roughness of the strut was kept constant as 1.5. The reduction in porosity caused by increasing the strut diameter gives a decreasing trend in permeability. The values of permeability decreased by an average of 46% when porosity decreased by 20%. To examine the effect of surface roughness of the strut on permeability, 4 volumes with different surface roughness were created by changing the value of coefficient *a* in Equation 3-1. The overall porosities were kept at 65 ± 1%. Permeability of foams with different strut morphologies is shown in Figure 3-15 (b). Permeability decreased from 12.5×10^{-10} to 3.9×10^{-10} m^2 as the surface roughness increased.

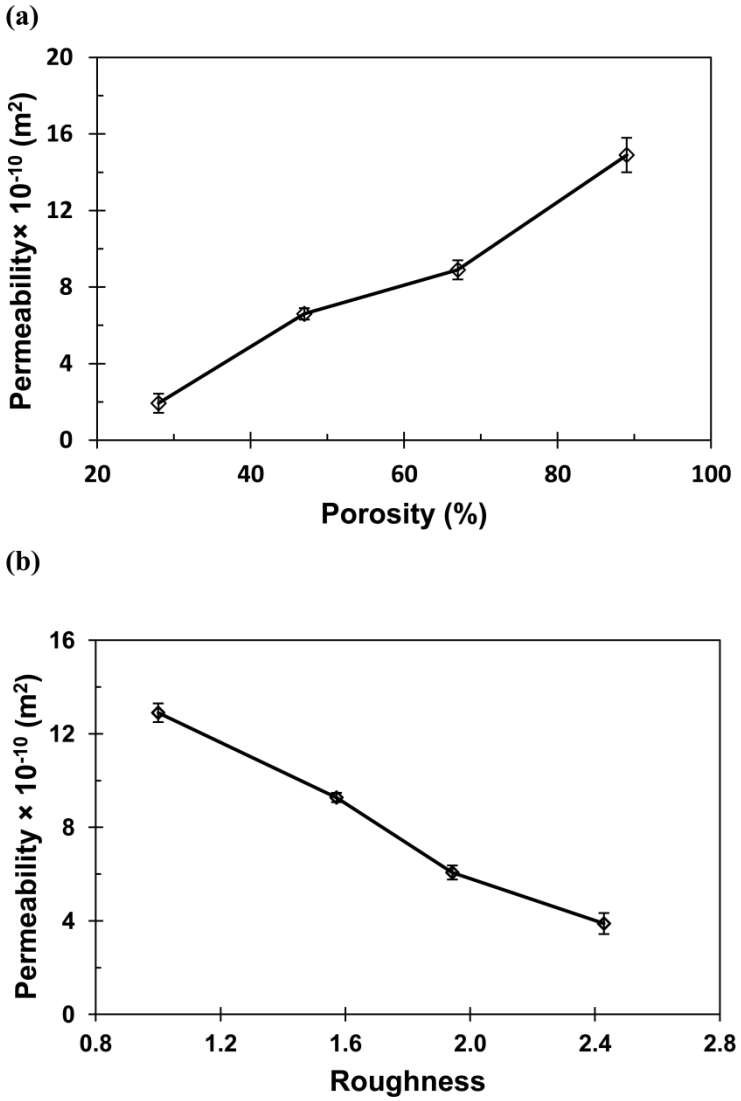

Figure 3-15 (a) Effect of strut diameter on permeability plotted as a function of porosity. (b) Permeability predicted based on foam structures with different levels of strut surface roughness. Average value of permeability was calculated for child volumes chosen. The error bar represents the standard deviation.

3.4 Discussion

SLM can be used to specify and produce new implant designs which maximise control of pore networks and their permeability. The UC approach was taken to form porous structures of 65% nominal porosity and pore size in the range 200 – 500 µm. Randomising these gridded cells by perturbation of their Cartesian coordinates allows the tortuosity and pore size distribution within the structures to be varied to modify the permeability characteristics. As already noted, these structures are not truly random, but pseudo-random, as the randomisation was based on an underlying regular structure and

the degree of randomness in any specific structure is exactly reproducible. It is important that the implants possess suitable pore networks and large enough interconnects for cell seeding and nutrition migration to stimulate expected bone ingrowth and vascularisation. Since permeability is one of the standard measures of a porous material's ability to transport fluid (Wang *et al.* 2005), we took permeability as a quantity reflecting the performance of implants, which depends on the structure's intrinsic pore size and internal network topology (Hui *et al.* 1996). The CFD prediction of permeability via 3D structure quantification data together with the practical measurements is discussed below.

3.4.1 Ti Foam Structure Quantification

Prior to undertaking permeability studies, preliminary characterisation of the porous microstructures was carried out to confirm that they lay within the acceptable range of pore characteristics. There is a discrepancy of $2.3 - 10.3\%$ between the estimated porosities based on μCT images and the measured porosities by the gravimetric analysis. Though an optimum threshold value was chosen upon normalisation of the greyscale histograms in order to keep the estimation unbiased, the resolution of the μCT scan affects the accuracy of the porosity estimation. Higher resolution images will be ideal in this case. The mode value of pore diameter for the structures increases as the randomisation level increases. It is particularly apparent in the 30% randomised structures that large pores with diameters ≥ 302 μm have been formed. This illustrates that the use of the SLM additive manufacturing technique is viable for producing Ti implant with controlled pore size, and structure morphology, by designing the lattice structure in the CAD model. The results from both the computational quantification and mercury porosimetry experiments showed that the pore size distribution widened as a result of randomisation, with the distribution changing from a narrow, tightly controlled band for regular structure, to a much broader band for the 30% randomised structures, as shown in Figure 3-10. The volume percentage of large pores greater than 302 μm in the 30% randomised structure is almost twice as much as the value in the regular structure. This is the result of changing the coordinates of the octahedron vertices that causes larger pores and wider channel spaces in the internal structure. Confirmation of this data can also be appreciated from the visualisations displayed in Figure 3-11. The difference between the quantification results and experimental data is in the range of

6.0 – 9.8%, demonstrating the ability of the μCT technique for porous structure quantification.

3.4.2 Ti Foam Structure Modification

The voxelisation of the CAD model allows the hierarchical design of the foam structure. As noted previously (Kohles *et al.* 2001; Nauman *et al.* 1999; Ochoa *et al.* 2009; Shimko *et al.* 2005; Singh *et al.* 2009), the studies on calculating permeability of the porous foams does not address how small changes in internal structure influence flow. The algorithm developed in this study provides a useful tool to evaluate the effect of changing porosity, strut ordering and strut surface morphology on permeability. The direct modification in the CAD volume allows cost-effective pre-evaluation of the influence of designing factors on the implant performance before the real foam is manufactured and provides the tool to alter the microstructure locally with bespoke design to achieve optimal properties. In this study, strut diameter was changed to alter the overall porosity of the foam from 28 to 89%, increasing in steps of 19 – 22% each time. The strut surface roughness was changed while keeping the overall porosity constant, to alter the permeability at a different scale from percentage porosity. The roughness was calculated (also non-dimensionlised) as the product of the surface area per unit volume and the characteristic length of the system. The latter term was chosen as the inverse of the specific surface area of the structure with smooth struts.

3.4.3 Permeability

From a practical perspective, the underlying principle for permeability is based on Darcy's law, which assumes that the pressure drop of the fluid passing through the porous structure is linear. Darcy's Law, however, breaks down when Reynolds number is greater than 10. That is when the flow becomes turbulent and, consequentially, inertial effects are no longer insignificant. Methanol was used as the fluid in the experiment to minimise surface tension and wetting effects, and also correcting for higher resultant flow by incorporating the Dupuit-Forchheimer correction factor. The data also show how randomising the structure has changed the permeability properties. It can be seen from the graphs (Figure 3-13) that the changes followed a consistent trend. The most permeable structure was the regular (0%) structure. On a macro scale, this structure had the smallest pores, and at first instance this would appear to be at variance to the results. However, by visualising the 3D structure offered by μCT, the

computational quantification algorithms (see Figure 3-11 and Figure 3-14) shows that the randomised structures are much more tortuous, and have a wider distribution of pore sizes, both increasing the path length that the fluid has to take, and presenting occasional narrow constrictions. As randomisation increased, the tortuosity increases and localised microscopic flow dominates. The permeability level drops from 0, to 10% and then 20% randomisation, despite the increase in pore size (Figure 3-10). There was, however, a reversal in this trend at the 30% randomised level, and it is postulated that the further pore size increase starts dominating more. It should be noted that these variations are all very small when compared to the 2 to 4 orders of magnitude change in the permeability of foams and bone.

Table 3-2 gives the three main components (*x*, *y*, and *z*) of CFD predicted permeability values for structures of 4 different levels of randomness. The 30% randomised structure was found to have the largest permeability amongst all the structures modelled. The mean permeability of this structure (30% randomised) revealed an increase of 5 – 17% compared to other structures. This increase in ease of flow (larger permeability) in the most randomised structure was due to the formation of preferential flow channels that formed in regions where the nodes were moved outwards. This also causes the formation of more tortuous channels, however, since the ease of flow is proportional to the square of the channel diameter (assuming Hagen-Pouiseuille flow (Park and Bronzino 2003)), the formation of the large diameter channels caused a net gain. This was considered to have the greatest effect at allowing fluid to pass through more easily in the 30% randomised structure since more randomised structures exhibited large connected void spaces. Additionally, in the aspect of localised microscopic flow, preferential flow channels in the 30% randomised structure create areas of increased flow shear stresses (More detailed study regarding the shear stress will be discussed in Chapter 5).

Previous studies showed that L_{REV} of at least 4-6 interconnects in the flow direction are required to determine the bulk representative permeability in materials ranging from fibres to bioactive glass scaffolds (Jones *et al.* 2007; Papathanasiou and Lee 1997). Figure 3-12 shows the study of L_{REV} used in the simulation. For the regular structure, it was found that a minimum edge length of 5 UCs was needed to reach a stable permeability independent of the volume chosen in the simulation. When it comes to the

most randomised structure, the L_{REV} required a minimum of 7 UCs because of the uneven distribution of pore spaces.

Figure 3-15 shows the effect of changes in the internal structure on permeability. From Figure 3-15 (a), it is clear that higher porosity gave more void space for the fluid to go through. An alteration of 20% in porosity results in an average permeability change of 46%, illustrating a strong effect of porosity change on the bulk flow properties. This suggests that the higher porosity will provide more spaces for flow/nutrition transport and bone ingrowth. However, the porosity will also interact with the strut ordering locally. From an implant's performance point of view, the regular structure with high porosity may result in a lower flow shear stress locally which may affect the ability of cell attachment and subsequent proliferation.

The strut surface roughness again has a significant effect on the flow property. There is a 68% difference in permeability between the smooth cylindrical strut and the roughest model. The localized roughness can therefore be adjusted to reach designated localized shear stress so that it allows bone ingrowth into certain areas when different density region design is wanted.

3.4.4 Sources of Errors

Figure 3-13 shows a comparison of the measured and modelled permeability in the *z* direction along which the Ti porous structure was stacked by layers of Ti powder in the SLM system. The permeability predicted by CFD simulations agreed well with the experimentally measured results (less than one order of magnitude). The main reasons that can potentially lead to the deviation of the three sets of results are considered:

First, there is an inevitable scan resolution versus sample size limitation when using the μCT. The resolution of the μCT scans of true volume was restricted to 9 μm per voxel due to the field of view. In order to achieve a large enough volume scan to represent the bulk structure the magnification was decreased which resulted in insufficient voxel size to represent the true surface roughness. Clearly, a rougher surface causes more resistance to flow. An underestimation of surface roughness will lead to a higher permeability value compared to the predicted permeability results for CAD models which were designed to have an intrinsic resolution of 5 μm per voxel. Higher resolution scans are required to represent the true structure so that the computational

modelling technique can be further refined. Secondly, there is a trade-off between the levels of down-sampling and the time needed for the simulation process. A very fine mesh model will certainly illustrate the surface roughness and true internal morphology of the structure better than the actual element size that was applied in this simulation. Thirdly, in the experimental methods used to measure the permeability, it is difficult to control the fluid flow rate at sufficiently low levels in order to achieve the same Reynold's number (*Re*) as applied in the simulation, owing to surface tension issues between fluid and porous structure. In CFD simulations, *Re* numbers were kept << 1 to ensure the laminar flow, while in experimental situations, *Re* numbers > 10 were employed. Finally, regarding the threshold value chosen for image processing, the misidentification of struts and pore space will lead to inaccurate determination of the interconnect size. This was considered to have a large effect on the overestimation of the permeability in the randomised structures due to the complex internal strut morphology.

Moreover, this CFD model assumes that the fluid passing through the porous structure is strictly Newtonian fluid. In reality, body fluids such as blood exhibit non-Newtonian behaviour, the viscosity depends on the shear stress and strain rate in the fluid flow. When the stress increases, corpuscles in blood deform and become preferentially oriented to facilitate flow. The viscosity therefore decreases with an increasing rate of shear stress, in which case there will be changes in the permeability microscopically. Advanced model can be developed to incorporate the shear thinning property of the blood so that the real biological situation can be modelled.

In summary, this study suggests that structure porosity, strut surface roughness and internal structure perturbation can be used for designing hierarchical additive manufactured implants with tailored properties. Each of the structural factors can be tuned to get designated flow properties independent of others. In particular, altering the surface roughness was demonstrated to vary the permeability by over 300% (reduced from 12.5×10^{-10} m^2 to 3.9×10^{-10} m^2 as roughness increased), but such changes are unlikely to have more than a small influence on static mechanical properties (e.g. Mullen *et al*. (Mullen *et al.* 2010) (Mullen *et al.* 2010) showed a 15% change in strength with a major change in strut arrangement). These variations in roughness could be implemented in the additive manufacturing process by varying laser spot size, power, and Ti powder size. There is good agreement between the computationally predicted

permeability and the experimentally determined values, which was validated by the simulation approach. Furthermore, the CFD predicted values in this study compare well with the measured human trabecular bone permeability in previous studies ranges between 1.2×10^{-10} and 8.05×10^{-9} m^2 as reviewed by Kohles *et al.* (Kohles *et al.* 2001).

3.5 Conclusions

This chapter investigated the effect of various input variables for the SLM additive manufacturing technique on the flow properties of Ti foams. The study demonstrated a computational approach to predict permeability in order to improve design of hierarchical implants using 3D μCT data quantification. Furthermore, a computational tool has been developed to allow scaffold designers to independently vary the porosity, strut surface roughness, each having a separate effect on the permeability. This approach, combined with additive manufacturing, allows an engineered hierarchical design, tailored for producing desired flows in implants.

4 Characterisation of the Mechanical Behaviour of Additive Manufactured Titanium Implants – *in situ* Compression Test and FE Modelling

In the previous chapter, the influence of AM Ti implant structures on flow properties was investigated. It is equally important to characterise the mechanical properties of the implant under load bearing environments. In this chapter, interrupted *in situ* compression tests were performed on an AM Ti implant with a designated structure. The results were compared to the FEA study and the influence of internal strut architecture on the mechanical behaviour of the implant was discussed.

4.1 Introduction

Porous foams such as polymers, ceramics, metals etc. have been widely accepted as implant materials in the field of orthopaedic industry (Ryan *et al.* 2009). Although the implant should provide sufficient void space and interconnected networks to support cell migration, nutrient transport and ingrowth, the mechanical performance of the implant is equally important for effective integration with the surrounding bone tissue (Freyman *et al.* 2001). Metallic foams such as porous Ti structures have increasingly drawn attention in orthopaedic applications due to their excellent strength-to-weight ratio, toughness and corrosion resistance (Müller *et al.* 2006; Singh *et al.* 2010; Wen *et al.* 2002).

Implant structural factors including macroscopic porosity, open or closed pores and microscopic strut morphology affect the mechanical properties of implants. As discussed in the previous chapters, novel RP technology such as SLM allows both macro and micro-structures of the implant to be controlled and therefore provides the opportunity to tailor implant design to match desired mechanical properties of the porous scaffolds (Ryan *et al.* 2006).

As reviewed in Chapter 2, there have been a number of studies focusing on the static compression test of the porous foams (Banhart and Baumeister 1998; Davies and Zhen

1983; Eshraghi and Das 2010; Imwinkelried 2007; Zhang and Wang 2005). Later the combination of μCT and *in situ* loading experiment takes advantage of being able to provide direct visualisation of how the spatial distribution and internal microstructure affect the global mechanical behaviour (Babout *et al.* 2003; Elliott 2002; Maire *et al.* 2003; Thurner *et al.* 2006). Analytically, Gibson and Ashby's model (Gibson and Ashby 1999) evaluates the mechanical properties of porous foams by assuming uniformity in the foam porosity and ignoring any axial or shear displacement of the strut during compression. The accuracy of the model is therefore largely affected by the nature of the porous structure. To obtain more accurate prediction of mechanical properties, FEA models based on μCT images have been developed (Eshraghi and Das 2010; Gorny *et al.* 2011; Ryan *et al.* 2009; Thelen *et al.* 2004). This modelling approach can not only overcome the simplification problem associated with the analytical model but also provide an insight into the stress concentrations in the structure.

In this chapter, three types of porous CP-Ti foam with different structural design (regular, randomised and combination of regular and randomised internal structure) were used to study the relationship between mechanical properties and foam microstructure. The implant is designed to be used in the surgical treatment of replacing the patella component in TKR (see Figure 4-1), where the implant functions as a fixation device between the artificial knee-cap and the native bone tissue. Therefore, the implant must firstly withstand the loading environment in the knee, and allow long-term biomechanical movements of the joint when the patient moves.

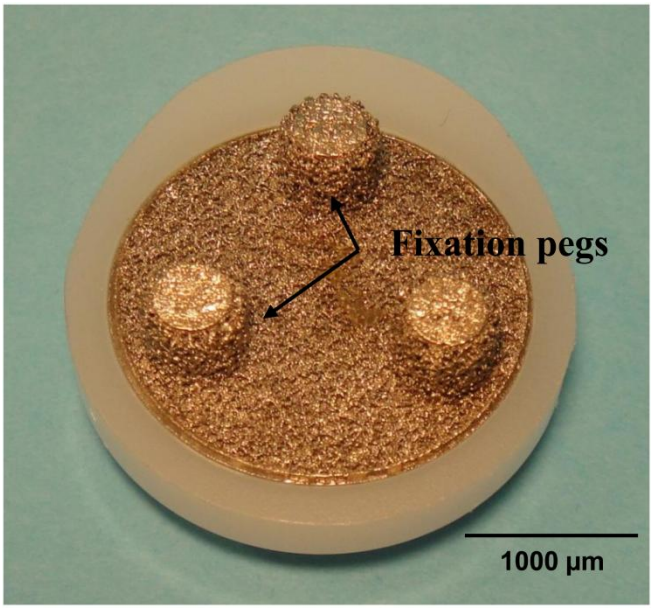

Figure 4-1 Porous CP-Ti implants designed for TKR with three fixation pegs.

An interrupted *in situ* compression test was performed on the implant structure and the mechanical data was then used as input material properties in the 3D FEA model. The failure mechanism was simulated by FEA and compared to the experimental observation in µCT. By modelling the mechanical performance of different implant structures computationally, the approach can be used as a guideline to tailor the porous foam design before manufacture to match mechanical properties locally within the structure.

4.2 Materials and Methods

4.2.1 Ti Foam and Sample Preparation

In this study, three different porous Ti implant structures designed by Mullen *et al.* (Mullen *et al.* 2010) using the UC approach were used to illustrate the effect of internal strut architecture on the mechanical performance. Details of the UC approach to make both regular and randomised structures were introduced in section 3.2.1. For the *in situ* compression test, the implant with a combined design of both regular and irregular structure was used (Figure 4-2). The implant consists of the regular (0% randomisation) structure of height 2 mm on the top and inside a 'U'-shape solid metal plate of 0.5 mm in thickness; the 30% randomised structure of height 3.5 mm was built below the solid metal plate. The implant has a diameter of 5 mm. The foam has a nominal porosity of 65% and all pores are open and connected. For the FEA simulations, pure regular and

30% randomised structures of size 4 mm in diameter and 4 mm in height were also included to further test the link between the internal strut microstructure and the mechanical behaviour of the foam under compression.

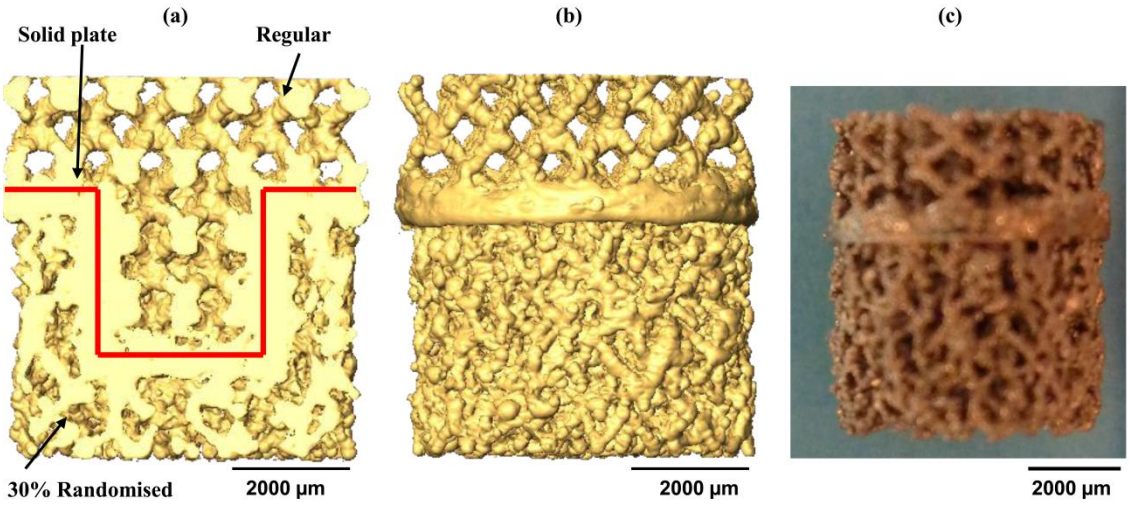

Figure 4-2 (a) & (b): 3D µCT images of the implant with a combined design of both regular and 30% randomised strut architecture. The red line indicates the position of the solid metal plate in the structure. (c): An image of the real implant.

4.2.2 Compression Tests

Two types of tests were performed to characterise the mechanical properties of the porous Ti implant: (1) static compression test to obtain the mechanical properties of the foam and (2) interrupted compression test along with µCT to provide a direct link between the foam microstructure and compressive behaviour.

The static compression test was performed using a 100 kN load cell servo-hydraulic universal testing machine (Zwick, GmbH, Germany). The tests were carried out up to a strain of 0.5 with a constant test speed of 0.001 m/s. The Young's modulus of the foam was calculated as the gradient of the regression line corresponding to the linear elastic region of the stress-strain curve. The yield strength was taken as the stress at the intersection of the regression lines corresponding to the linear elastic region and the plateau region.

The interrupted compression test was performed with *in situ* µCT. A screw-driven 10 kN compression rig (Figure 4-3) was designed for the test. The interrupted compression test was performed using a nominal strain of 0.05 each time. A µCT scan was performed after each compression at a resolution of 15 µm per voxel using a

commercial µCT unit (Phoenix v|tome|x, GE Measurement and Control, MA, USA). The X-ray tube voltage and filament current were fixed at 100 kV and 70 µA, respectively. 720 projections were collected on a 512 × 1024 detector at a rotation step of 0.5^{o}. Images were then reconstructed using the commercial reconstruction software datos|x (GE Measurement and Control, MA, USA). Pre-processing of the 3D volume, including a 3 × 3 × 3 median filtering and removing islands within the volume space was accomplished using a commercial image visualisation/analysis software Avizo 6.3 (VSG, MA, USA) and an in-house developed codes (Atwood *et al.* 2004; Jones *et al.* 2007).

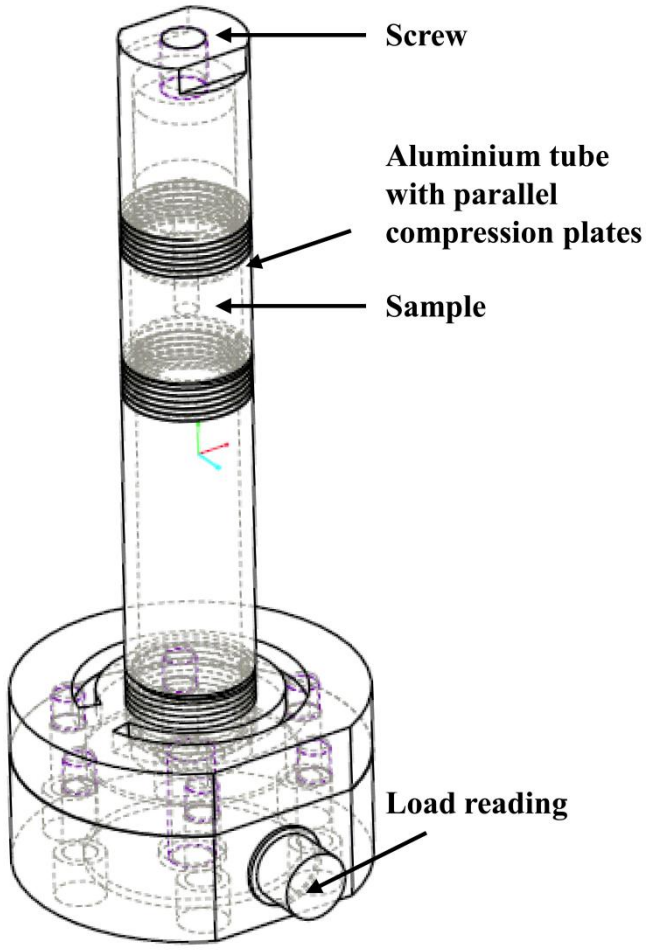

Figure 4-3 Compression rig used in the *in situ* mechanical test with a 10 kN load cell. (Design provided by Mr R. Hamilton, Imperial College London, UK)

For each step of the deformation, two load readings were recorded at the beginning and the end of the scan respectively and the arithmetic average value of the load readings

was used as the averaged load in the stress-strain analysis. Vertical displacement and the cross-sectional area of the sample after each compression test was calculated based on the 2D tomography images in a public domain image processing programme ImageJ (NIH, USA).

4.2.3 Model Theory

4.2.3.1 FEA Method

FEA is an effective method to solve for the approximate solution of governing differential equations in the mechanics of deformable solids. The ODEs or PDEs are converted into a linear combination of a finite set of algebraic functions and solved. The process starts with discretisation of the region of interest into a number of 2D or 3D elements (meshing). The meshing elements are connected by sharing common points (nodes) and each node is associated with the unknowns (e.g. displacement, temperature) to be solved.

The basis of the FEA method is known as the 'principle of virtual work'. The principle can be expressed in terms of an equilibrium equation of loads, where the work done by external loads for a virtual displacement should equal to the internal virtual work absorbed by the element during that displacement. Mathematically, it can be written as:

$$\delta\vec{v}^T\boldsymbol{f} = \int_V \boldsymbol{\varepsilon}^T\boldsymbol{\sigma}\, dV \qquad \textbf{4-1}$$

where $\boldsymbol{\sigma}$ is a set of internal stresses, $\boldsymbol{\varepsilon}$ is the expression for internal strains, $\boldsymbol{f}$ is a set of external forces and $\delta\vec{v}$ is the virtual displacement.

The strain can be expressed in terms of the virtual displacement:

$$\boldsymbol{\varepsilon} = [B]\delta\vec{v} \qquad \textbf{4-2}$$

where $[B]$ is the strain-displacement matrix.

The stress can then be written as:

$$\boldsymbol{\sigma} = [D][B]\delta\vec{v} \qquad \textbf{4-3}$$

where $[D]$ is the matrix of elasticity.

Hence Equation 4-1 becomes:

$$\delta\vec{v}^T\boldsymbol{f} = \int_V \delta\vec{v}^T[B]^T[D][B]\delta\vec{v}\, dV \qquad \textbf{4-4}$$

Rearrange to obtain:

$$\delta\vec{v}^T\boldsymbol{f} = \delta\vec{v}^T \int_V [B]^T[D][B]\, dV\delta\vec{v} \qquad \textbf{4-5}$$

Let the integral in Equation 4-5 be a matrix, [k], which denotes the stiff matrix.

The above equation can be written as:

$$\boldsymbol{f} = [k]\delta\vec{v} \qquad \textbf{4-6}$$

Now the governing equation becomes a system of matrix equations, which contains *n* equations for *n* choices of $\delta\vec{v}$ to solve.

4.2.3.2 Compression Test Simulation

µCT images of three porous Ti structures (regular, 30% randomised and combination of the regular and 30% randomised design) were segmented using the same thresholding method described in section 3.2.7 (i) (Figure 3-6). Tetrahedral elements were chosen as they generate a smoother surface which enables a more accurate calculation of loading at the surface of the structure (Ulrich *et al.* 1998). Images were resampled to 30 µm per voxel. Meshes were generated using commercial FEM meshing package, ScanIP (Simpleware Ltd., UK). A convergence test was run using two regular models with resolutions 15 µm and 30 µm respectively to validate the mesh refinement. Each model was meshed using element sizes of both 15 µm and 30 µm. FEM analysis software Abaqus/CAE-Standard v6.10-1(Dassault Systemes Simulia Corp., USA) was used to perform the simulations. All cases were run on the Imperial College High Performance Computing system using 2 nodes, each of which has 4 cores.

Figure 4-4 shows the schematic of the 3D FEA model and the boundary conditions applied in the simulation. To match the *in-situ* compression test, the top surface node set was assigned a displacement equivalent to a maximum strain of 0.05 along the *z*-direction in each compression step; the bottom surface was restricted from moving in the *z*-direction. To prevent the structure slipping, 4 equidistant nodes on the edge of the bottom surface were constrained from moving in both *x*-direction and *y*-direction. No boundary contact surfaces condition was set for the densification region. The elastic modulus was calculated as the gradient of the elastic region of the stress-strain curve

and the compressive strength was estimated by using the same procedure described in section 4.2.2. Other materials properties used in the simulation are listed in Table 4-1.

Though the whole sample was used in the simulation, a sensitivity test was performed on both regular and randomised structures with increasing size in the compression direction (*z*-axis) to check if the volume used is appropriate to represent the REV for the FEA analysis. All the volumes were made to have similar overall porosity (63 – 65%).

Table 4-1 Parameters used as input materials properties in FEA simulations:

Property	Value	Unit	References
Density (ρ)	4500	kg/m^3	Mullen *et al*. (Mullen *et al.* 2010)
Young's modulus (E)	116	GPa	Singh *et al*. (Singh *et al.* 2010)
Poisson ratio (ν)	0.3	--	Singh *et al*. (Singh *et al.* 2010)
Yield Stress (σ)	45.6	MPa	Mullen *et al*. (Mullen *et al.* 2010)

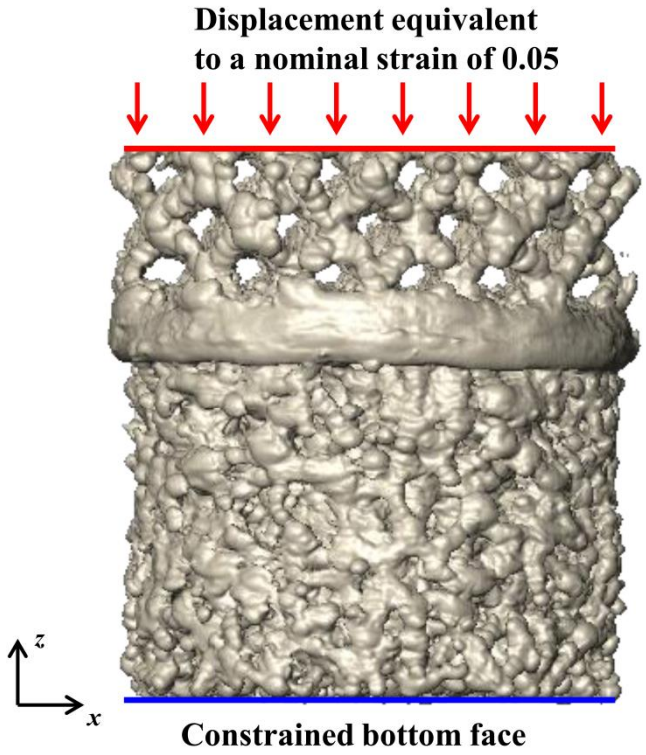

Figure 4-4 Schematic of the 3D FEA simulation: the model has a top node set which was assigned a displacement equivalent to a maximum strain of 0.03 along *z*-direction in each deformation step and a constrained bottom node set.

4.3 Results

4.3.1 *In-situ* Interrupted Compression Test

Figure 4-5 shows the *xz*-plane view of each deformation step obtained by µCT. The displacement in *z*-direction and the cross-sectional area of the sample were measured directly from µCT images. Plastic deformation started to occur after a strain level of 0.086, indicated by the collapse of the struts. Figure 4-6 shows a clearer 3D view of local strut deformation. The red ellipsoids in Figure 4-6 (a) & (b) indicate a single unit cell before and after the elastic deformation. The cell wall collapsed in the next deformation step, as seen in Figure 4-6 (c).

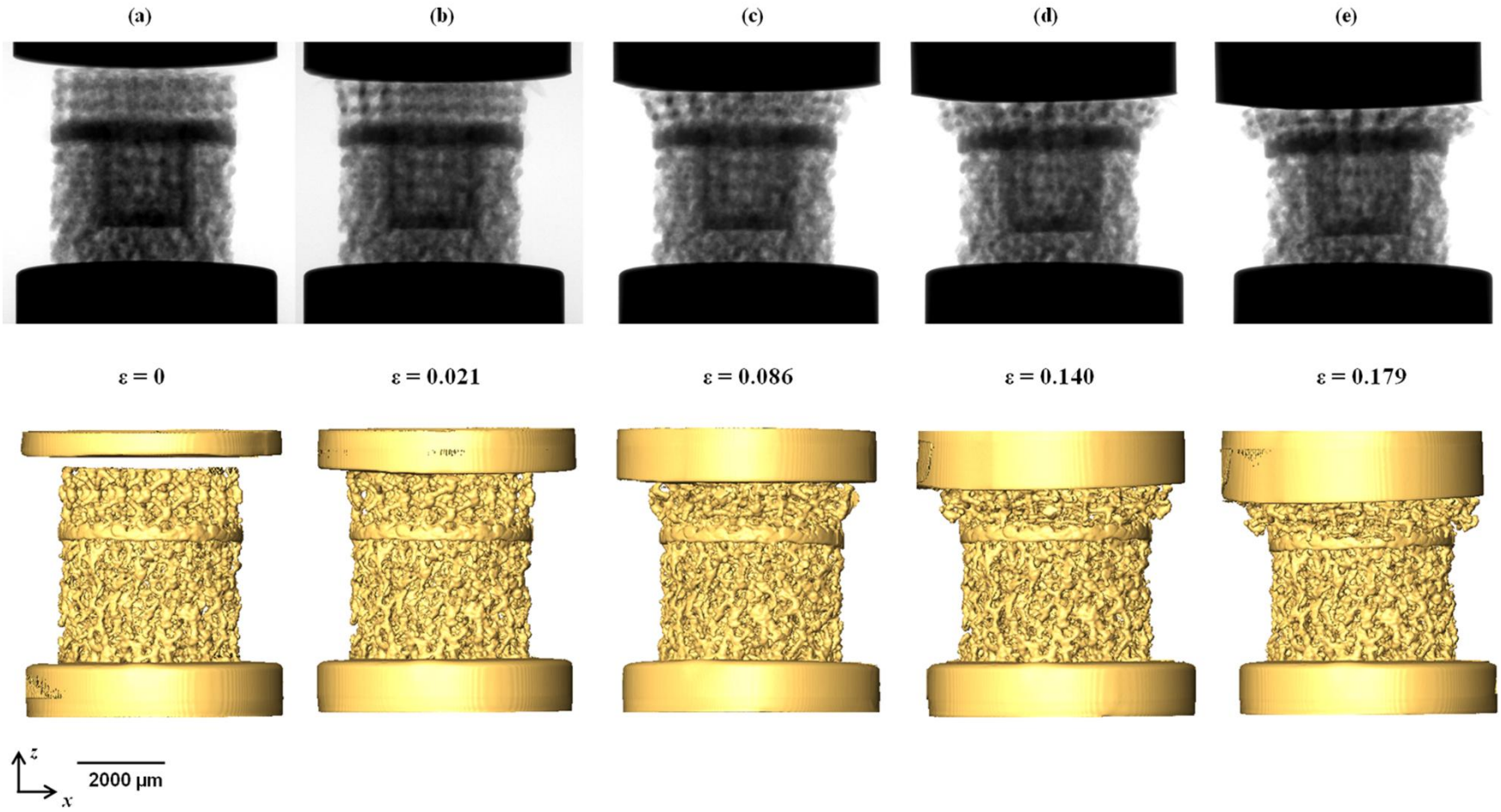

Figure 4-5 (a)-(e): 2D and 3D *xz*-plane views of deformation steps obtained from µCT datasets. True strain of each deformation step was calculated based on the tomography images.

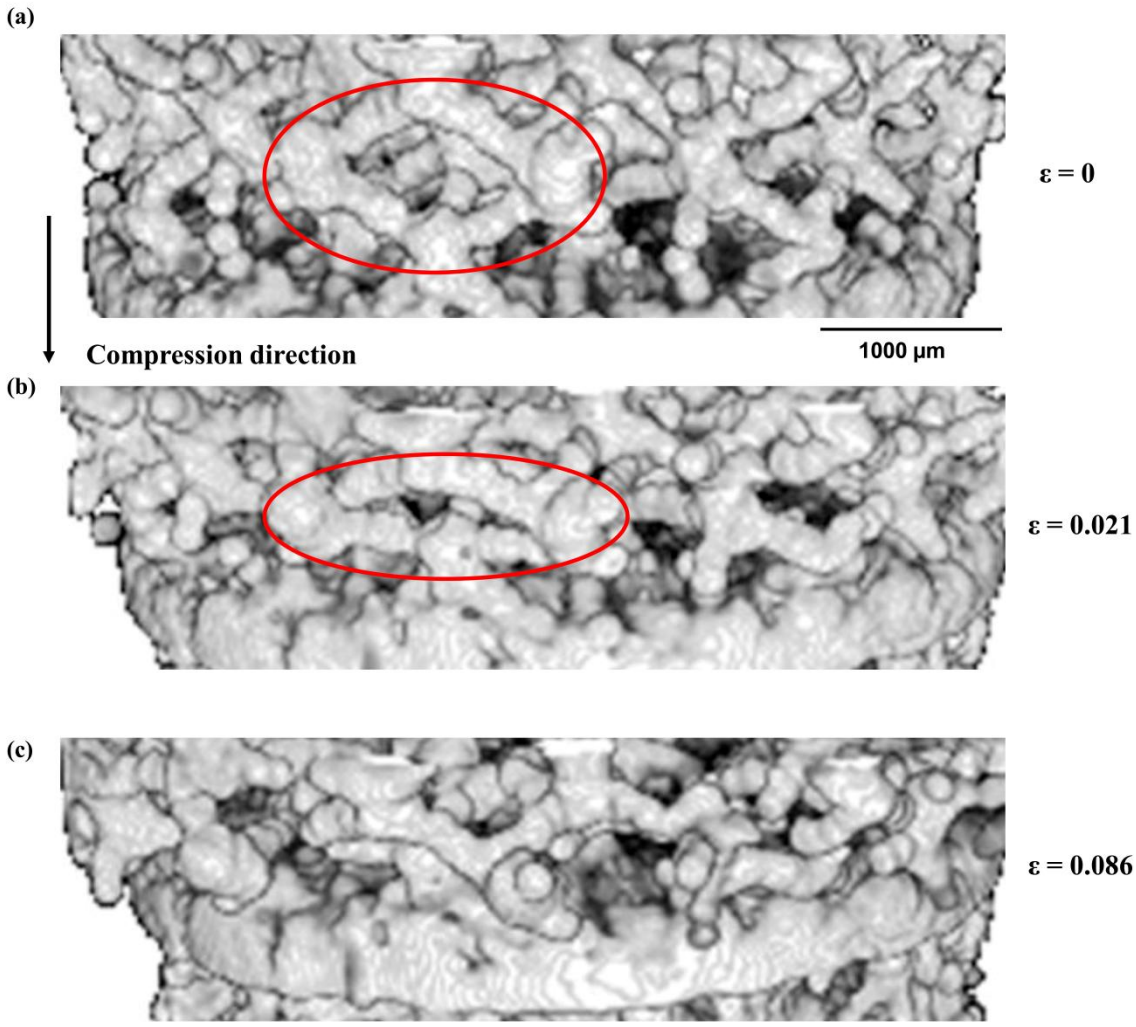

Figure 4-6 Localised collapse of the regular strut at low strain levels (shown in red ellipsoids): (a) undeformed implant structure before loading, (b) implant structure after the first deformation step, (c) collapse of the struts occurs at the second deformation step.

4.3.2 FEA Simulation

Table 4-2 shows the convergence test result to validate the mesh refinement. The resulting yield strength obtained from the two tests showed trivial differences of approximately 4%. A mesh size of 30 µm changed the results by 4.1% when the resolution was doubled. Hence, to accommodate both the mesh accuracy and the computational cost, the element size was chosen to be 30 µm for all models.

Table 4-2 Convergence test results showing numerical yield strengths predicted using different mesh refinements.

	Model 1	**Model 2**	**Model 3**	**Model 4**
Image resolution (µm)	15	15	30	30
Mesh size (µm)	15	30	15	30
Yield Strength (MPa)	28.5	27.1	27.3	28.2

In Figure 4-7 (a) and (b), results from the REV study of the FEA model are shown. It was found that for the regular structure, an REV length along the compression direction of at least three unit cells was needed to stabilise the mechanical parameters obtained from the model. The REV length required by the randomised foam was found to be greater than the regular foam because of the in-homogeneous nature of the structure. All sample volumes used in simulations were confirmed as appropriate because the dimensions are much greater than the REV length.

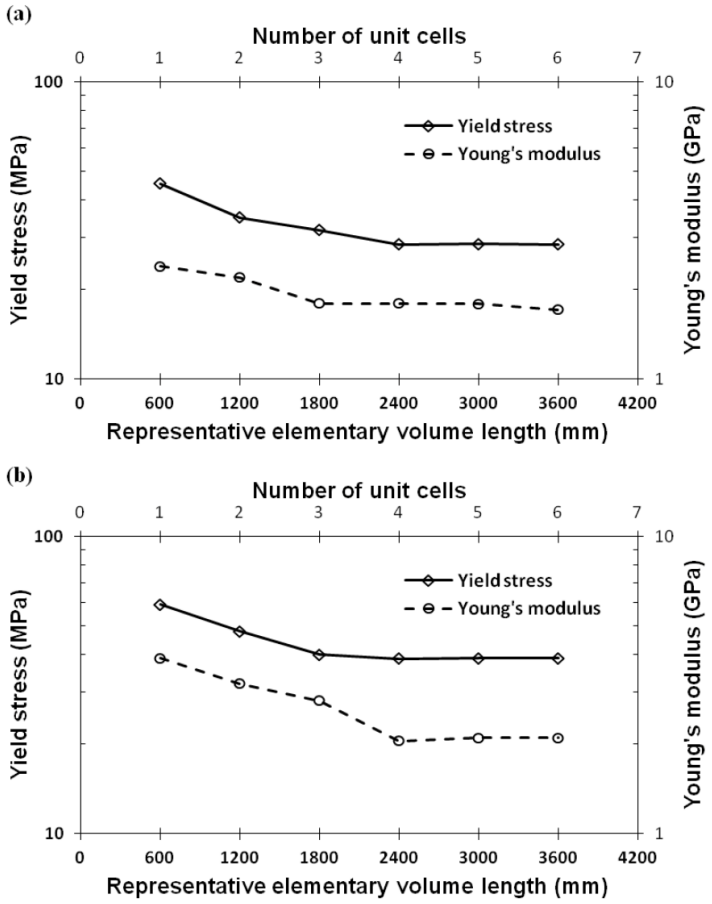

Figure 4-7 (a) & (b) REV study: FEA simulation results of modulus and yield stress values of the regular and 30% randomised foams as a function of the REV length along the compression direction.

Figure 4-8 shows a zoomed-in part of the stress-strain curve obtained from the FEA simulation on the implant with the mix regular / randomised structure, in particular, showing the behaviour of the implant at initial low strain levels. The curve shows elasto-plastic behaviour from a strain level of 1% on this curve, indicating that there were local plasticity changes occurring during early stages of the deformation.

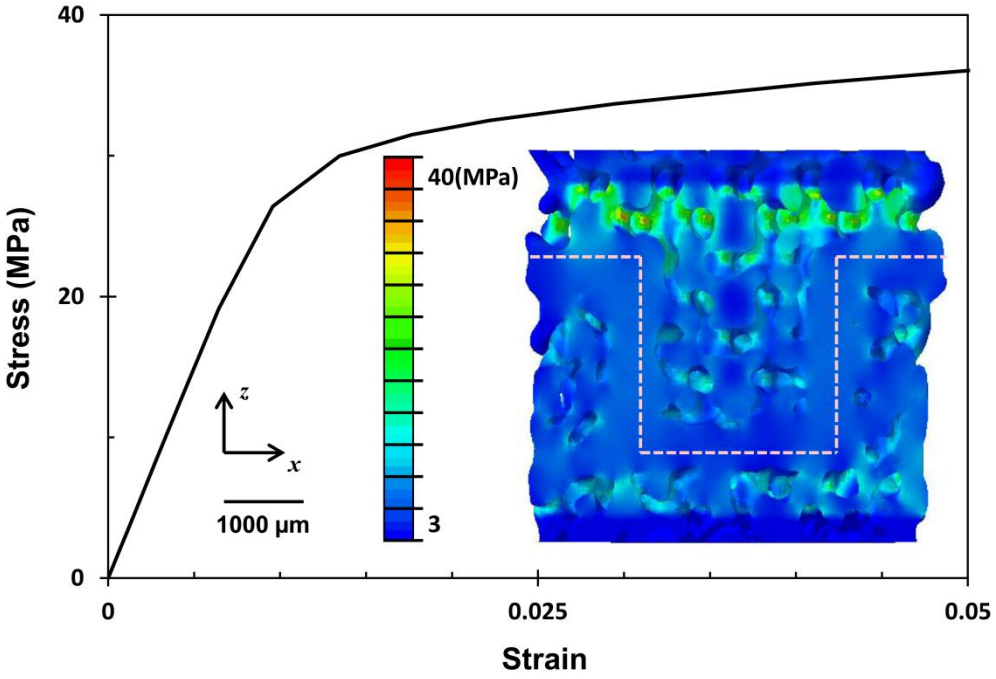

Figure 4-8 Compression test via the FEA simulation: stress-strain curve of the implant with the combined regular-randomised design. Inset: *xz*-plane view of the stress distribution inside the implant structure during its elastic deformation step.

To further examine the influence of the structure design on the mechanical performance of the implant, FEA simulations were performed on Ti implant with regular and 30% randomised design. Figure 4-9 shows a comparison plot of the stress-strain curves of both regular and the 30% randomised structures. The effective yield stress for the regular and the 30% randomised structures were 28 MPa and 39 MPa respectively and the effective Young's modulus for the regular and the 30% randomised structures were calculated as 1.7 GPa and 2.1 GPa respectively. The local stress distributions of both structures at the same strain level are compared in Figure 4-10. More areas of yield can be seen from the regular structure as compared to the 30% randomised. Furthermore, the distributions of stress during the deformation in the two different structures suggest that the stress is more uniformly distributed in the regular structure while more localised distribution of stress is found in the 30% randomised design.

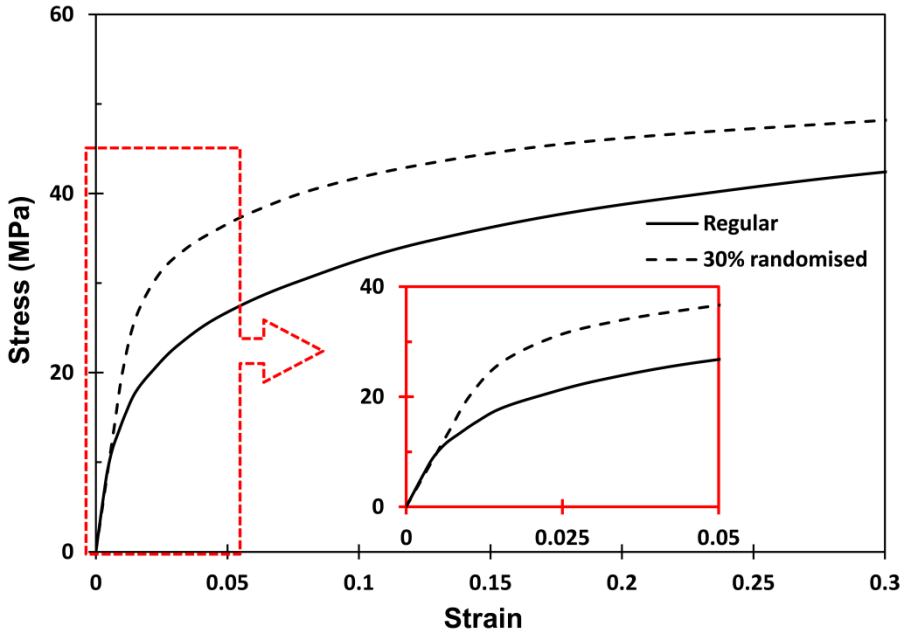

Figure 4-9 Comparison plot of the compression stress-strain curves of both regular and 30% randomised structures, data obtained from the FEA simulation.

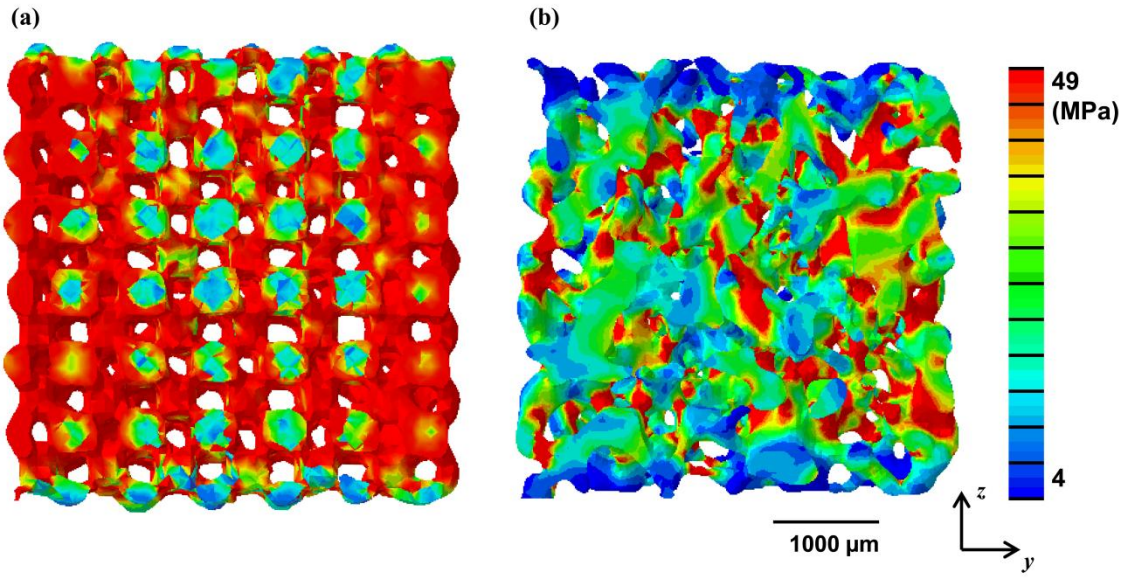

Figure 4-10 2D *yz*-plane views of local stress distributions in (a) the regular and (b) the 30% randomised structures.

4.3.3 Comparison

From the average load readings and the sample cross-sectional area obtained in the interrupted compression test, the compressive stress was calculated and from the displacement and the initial sample height, the strain was calculated. The stress-strain

curve is shown in Figure 4-11. This curve shows the typical mechanical behaviour of porous metals under compression. The initial linear regime shows the elastic deformation of the structure up to a strain of 0.02, followed by a plateau regime which corresponding to the collapse of the struts and finally a densification regime. The elastic modulus calculated based on this curve was 1.5 GPa, which falls within the range of stiffness of human trabecular bone (1 – 10 GPa) (Mullen *et al.* 2010). The yield strength was 32 MPa, which was taken as the stress at the intersection of the linear regression lines corresponding to the elastic and the plateau regions. The stress-strain curve obtained from the static compression test is shown in the same figure for comparison. The Young's modulus and the yield strength estimated from the static compression test were 0.4 GPa and 33 MPa, respectively. A corrected stress-strain curve was plotted when the sample is in full contact with the compression platform to eliminate the contact surface effect. This was done by subtracting the stress and strain in the initial non-linear region. The stress-strain curve from the FEA uniaxial compression test simulation of the implant with the same design is also shown in Figure 4-11. The effective Young's modulus and the yield strength predicted in this case were 2.2 GPa and 30 MPa, respectively.

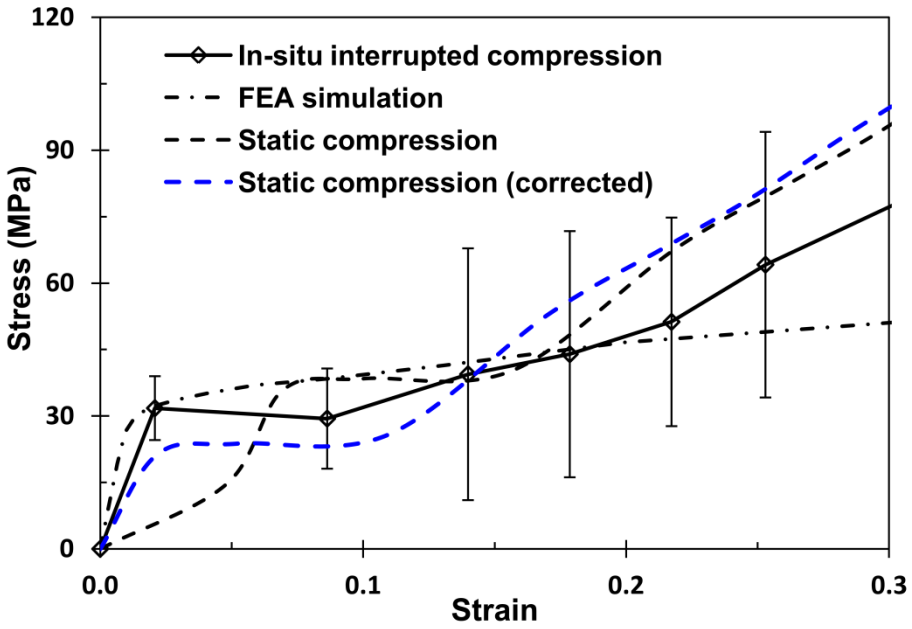

Figure 4-11 Comparison of the static, *in situ* interrupted mechanical tests and the FEA simulation: compression stress-strain curves of the porous Ti implant with the mixed regular and randomised design.

4.4 Discussion

Both experimental and computational modelling approaches have been employed in the study to investigate the mechanical behaviour of the Ti implants under compression loading. μCT imaging technique was coupled with the interrupted compression test to provide a direct observation of the deformation and the failure mechanism of the structure. The FEA compression model based on μCT images of real Ti structures further revealed a more detailed examination of how the foam internal microstructure affects the mechanical performance of the implant during the elastic deformation.

4.4.1 Compression Tests and mechanical behaviour of the implants

The mechanical properties experimentally measured by both static and interrupted compression tests were compared in Figure 4-11. The stress-strain curves obtained by both approaches showed the typical compressive behaviour of porous metal foam. The yield strength calculated from both methods agreed well with each other. However, there exists a significant difference in elastic moduli of the implant. The static compression test measured the elastic modulus of the sample to be less than a third of the value measured by the interrupted test. The low value of modulus measured in the static compression test was mainly due to the non-planar surfaces of the sample and the contact compliance between the test sample and the two metal compression plates. (Note that in both the interrupted compression test and the FEM, the top and bottom surfaces were made planar.) These caused the non-linear behaviour of the implant before the yield strength was reached on the stress-strain curve, which indicates that some inelastic phenomena were present during the initial compression stage (Müllner *et al.* 2008). The other cause of the non-linearity in the stress-strain relationship was that there might be changes in the orientation of the struts which will change the apparent elastic modulus at moderate strain levels. The corrected stress-strain relationship which eliminates the initial non-linear region gave a closer match of elastic modulus (1.0 GPa). This, however, affected the estimate of the yield stress. To further assess if an early stage compressive behaviour of the foam is elastic of plastic, a loading-unloading cycle can be applied to the structure to check the reversibility of the stress-strain relationship. A hysteresis loop in this relationship can then be attributed to plasticity.

Compared to the static compression test, FEA simulation provided a closer match to the interrupted compression test results for both elastic modulus and the yield stress. However, the elastic modulus of the implant derived from the FEA study is 1.5 times greater than the value obtained from the interrupted test. The deviation may be explained by the torque in the strain-locking process when the compression load was applied manually by turning the screw at the top of the compression rig. The sample slipped on the rig platform and was slightly rotated. A reliable correlation of the FEA model to experiment requires a close match of the FE boundary conditions to the experimental conditions (Jacobs *et al.* 1999). Hence, modification for the parallel plate compression test is needed to overcome the error due to the contact boundary behaviour. For example, sample can be fixed to the end-caps of the compression rig so that slip condition at the bottom surface can be prevented.

To compare with the literature, Mullen *et al*. (Mullen *et al.* 2010) experimentally measured mechanical properties of the same regular and 30% randomised structures and reported higher Young's moduli (3.5 – 6.5 GPa) and yield strengths (49 MPa for the regular and 56 MPa for the randomised) than those predicted in FEA simulations. Apart from the difficulties associated the mechanical tests as discussed earlier; there are also potential reasons that may cause the inaccuracy of the FEA prediction, which will be discussed in the next section.

To compare with the analytical model of open cell foam with homogeneous structure developed by Gibson and Ashby (Gibson and Ashby 1999), the Young's modulus, E^*, and the yield strength, σ^* of the regular structure were calculated by:

$$\frac{E^*}{E_s} = \left(\frac{\rho^*}{\rho_s}\right)^2 \qquad \textbf{4-7}$$

$$\frac{\sigma^*}{\sigma_s} = 0.2\left(\frac{\rho^*}{\rho_s}\right)^{1.5} \qquad \textbf{4-8}$$

where E_s and σ_s are the Young's modulus and the yield strength of the solid material and ρ^*/ρ_s is the relative density of the open cell foam. The analytical model predicts the Young's modulus and yield strength of the regular structure to be 37 MPa and 15.9 GPa, respectively. The analytical model predicts significantly higher modulus than both experiment and FEA model (5 – 10 times). For yield strength, the analytical prediction is 32% higher than FEA but 24% lower than experimental measurement. The

overestimation is due to the inability of the model to account for the interconnectivity of the struts phase, which is indeed considered in the FEA analysis.

Overall, the elastic modulus of the porous Ti implant tested falls within the range of the human trabecular bone (1 – 10 GPa). The yield strength of the structure also satisfies the typical requirement for structures suitable for orthopaedic applications (~40 MPa) (Mullen *et al.* 2009). This indicates that these Ti structures are suitable for implant applications.

4.4.2 Limitations of the FEA model

The machine contact compliance problem associated with the static compression test and the difficulty of obtaining low strain level deformation in the stepwise compression test can be avoided in the FEA simulation, so that a linear elastic behaviour of the foam at low strain levels can be obtained (Figure 4-9). Although the FEA model gave the closest match to the literature values for both elastic modulus and the yield strength, there were still several limitations associated with the current model which can be improved to obtain more accurate results.

First of all, the original resolution of the µCT images has a significant effect on the accuracy of the image based FEA model (Yeni *et al.* 2005). Due to the size limit of the field of view in the µCT, the resolution was set at 15 µm per voxel. The fine micropores and surface roughness inside and on the surface of the strut might not be fully captured. Furthermore, for the best computational efficiency, the µCT images were resampled to 30 µm. This may lead to the inaccuracy in predicting the strength of the material as it smoothes fine strut surface roughness on struts so that the thickness of the strut was either reduced or enlarged depending on the neighboring voxels. The accuracy of the FEA stress analysis also depends on the threshold value chosen in image processing. Hara *et al*. (Hara *et al.* 2002) found that a variation of 0.5% in threshold resulted a difference of 9% in stiffness of the trabecular bone (porosity > 85%) and 3% when porosity is less than 80%. Thus it is important to use an optimum threshold for accurate estimation of the mechanical properties in FEA analysis. Advance thresholding technique other than the plain threshold method will be more ideal in processing images with low resolution (Homminga *et al.* 2001).

Secondly, the mesh quality of the FEA model is also of great importance in assuring the accuracy of the simulation (Moazen *et al.* 2011). The influence of the element size on the FEA model accuracy was discussed in several studies (Cahill *et al.* 2009; Depalle *et al.* 2013; Jones and Wilcox 2008; Lacroix *et al.* 2006; Migliavacca *et al.* 2002). Both Cahill *et al.* (Cahill *et al.* 2009) and Depalle *et al.* (Depalle *et al.* 2013) suggested in their studies that at least 3 - 4 elements across the strut thickness (diameter) are needed for accurate stress field prediction. Jones and Wilcox (Jones and Wilcox 2008) suggested in their study of vertebral body FE model that a choice of mesh resolution is considered as refined when the change in the result is less than 5% when the resolution is increased. In addition to the mesh resolution, choice of element type also has an impact on the FEA modelling accuracy. Depalle *et al.* (Depalle *et al.* 2013) compared the results obtained using different types of FEA meshing elements for stress evaluation for human trabecular bone. It was found that for low resolution images, the use of linear elements or reduced integration leads to inaccurate prediction of the stress distribution due to stiffening errors and severe smoothing. Quadratic elements are preferred for stress field estimation in low resolution models. However, this type of element will have high computational cost.

4.4.3 Influence of the Strut Architecture on Mechanical Properties

Although the *in situ* interrupted compression test provided a visualisation of the deformation of the struts, the initial elastic behaviour at very low strain level and the stress concentration within the structure could not be easily obtained. The FEA simulation instead, was able to predict not only the mechanical properties of the implant but also the initial elastic deformation and the localised stress distribution inside the structure.

Figure 4-8 shows the compressive stress-strain curve during the deformation of the implant at low strain levels. The structure showed elastic deformation behaviour up to a strain of 1% and local plasticity changes occur afterwards. The regular structure on top of the solid plate took more load during the compression and struts broke more quickly than in the bottom randomised part. This was confirmed in Figure 4-9 where the comparison of the strength and modulus properties of the regular and the 30% randomised structures shows the same trend. Furthermore, the regular struts inside the ‘U’-shape solid plate also showed less concentration of stress. In this case, the solid

metal plate is believed to act as a load bearing feature to retain the overall structure of the implant under the loading. The failure mechanism of the top part of the implant was consistent with the homogeneous model suggested by Gibson and Ashby (Gibson *et al.* 2010) where the collapse of the first pore is followed by the collapse of its neighbour pores normal to the loading direction. Hence the local plasticity deformation progressed layer by layer along the compression direction.

FEA models created for pure regular and randomised foams showed clearer comparison of stress distributions between the two structures. The stress was more uniformly distributed in the regular structure while more localised distribution of stress was found in the randomised design (Figure 4-10). The load is more easily transformed axially in the regular foam due to its highly oriented design so the failure involves the entire cross section in contrast to the randomised structure. For the 30% randomised structure, high stress concentration regions were found where random initiation of the strut failure occurs. Due to the in-homogeneity of the structure, load propagates locally so that the collapse of struts was more isolated compared to entire failure of the load bearing plane in the regular structure.

4.5 Conclusions

This chapter presents both experimental and the direct 3D FEA approaches to determine the mechanical properties of the porous Ti foams and to characterise the elastic and post-yield deformation behaviour under compression.

The FEA simulation provided the closest predictions of both the strength and modulus properties to the ones experimentally measured and the literature values. This indicates the viability of the computational approach to characterise the highly porous Ti structure used for the orthopaedic implants. The results showed that the randomised bone-like structure has better mechanical performance as compared to the regular structure. The FEA study provided an improved understanding of the mechanical performance of the foams at their earlier deformation stage; in particular, the different stress distributions throughout implants with different internal strut architecture were observed. Therefore, the current model can provide useful information in understanding the failure mechanisms in porous metallic foams used as implants in the loading environment inside the body.

5 Modelling of Time Dependant Localised Flow Shear Stress and Its Impact on Bone Ingrowth within Additive Manufactured Titanium Implants*

In this chapter, a 3D transient model of bone ingrowth based on the N-S equations will be presented. The model simulates the body fluid flow and stimulation of bone growth as a function of local flow shear stress. The model's effectiveness is demonstrated for two AM Ti scaffolds, with regular and randomised strut architectures as described in section 3.2.1, respectively. Applying CFD methods at a microscopic level taking into account the detailed scaffold structures, this study demonstrates the potential new insights that can be gained via the modelling tool, and how the model can be used to perform what-if simulations to design AM structures to function.

5.1 Introduction

As reviewed in Chapter 2, implants for bone augmentation are expected to stimulate bone ingrowth to enable fixation to the host bone. Vascularisation and osteogenic cell proliferation are promoted in bone healing process due to the interstitial fluid flow in periosteum and surrounding tissues (Wray and Lynch 1959). Moreover, flow through porous foams with different internal structures will result in tortuous paths (Fourie *et al.* 2007). This will impact the fluid shear distribution which can stimulate cell growth (Holtorf *et al.* 2005; Kapur *et al.* 2003; Reich *et al.* 1990; Sikavitsas *et al.* 2003) and the motion of cells along preferential routes.

---

*Note, a large portion of this chapter is submitted for publication:

Zhang Z., Yuan, L., Lee P.D., Jones E., Jones, J.R., Modelling of Time Dependant Localised Flow Shear Stress and Its Impact on Bone Ingrowth within Additive Manufactured Titanium Implants, Journal of Biomedical Materials Research Part B: Applied Biomaterials, 2013

Previous studies regarding flow-induced shear stress occurring in *in-vitro* perfusion systems (Dillaman *et al.* 1991; Freed and Vunjak-Novakovic 2000; Kapur *et al.* 2003; Sikavitsas *et al.* 2003), reviewed in section 2.6.1, showed the important influence of fluid flow-induced shear on cell land tissue growth. Prior studies (Chung *et al.* 2007; Cioffi *et al.* 2006; Coletti *et al.* 2006; Lesman *et al.* 2010; Liu *et al.* 2012; Porter *et al.* 2005; Raimondi *et al.* 2011; Raimondi *et al.* 2004; Raimondi *et al.* 2006) focused on macroscopic average shear stress predictions; however, these have yet to be coupled with time dependent simulation of the influence of cellular parameters, such as growth rate, deposition, and the resultant time dependant porosity change. All these issues are crucial to the correlation of fluid-induced shear stress and cellular growth. A comprehensive study on the local shear stress effect on bone cell ingrowth which inter-relates time dependant microscopic flow simulation with flow-induced shear stress distribution on a microscopic level is therefore of great usefulness.

Two of the porous open cellular Ti foams (regular and 30% randomised) designed using the UC approach described earlier will be investigated in this chapter. The CFD model is applied directly on the voxelised CAD designs as a demonstration of the applicability of the simulations to help analyse real designs.

The aim of this chapter is to provide a better understanding of the complex coupling of how flow and porous scaffold struts architecture impact osteointegration. The goal is to quantify local flow shear stress to predict bone ingrowth at microscopic level, and then feed the results bone growth back into flow simulations to interrelate the resultant porosity change to shear distribution. A 3D microscale CFD model based on finite volume method has been developed to simulate the flow system first. The fluid flow-induced shear stress was then calculated with a finite difference method and the time dependant cell growth and the inter-relationship between the two dynamic factors was estimated by the cellular automaton (CA) method. The model was applied to study the influence of strut architecture design in AM Ti implants, with the inter-relationship between the flow-induced shear stress and the time dependant cell growth at the microscopic level.

5.2 Materials and Methods

5.2.1 Ti Foam Microstructures

Two different porous Ti implant structures designed via the UC approach by Mullen *et al.* (Mullen *et al.* 2010) were selected as the input structures for this study. The regular (0% randomisation) and 30% randomised designs were chosen as the illustration of how different internal strut architecture influence the bone ingrowth. Details of the design of these two structures were introduced in section 3.2.1. The grid mesh is based on the voxelised CAD volume, which has been discussed in section 3.2.4.

Note that the variability has been quantified both by Mullen *et al*. (Mullen *et al.* 2010), and also in terms of baseline flow properties in Zhang *et al*. (Zhang *et al.* 2013), therefore only one example of each design type will be studied, and only as a virtual model. The overall porosities of the two test volumes are similar at 67.5% and 69.2%, respectively. The effects of randomising the regular lattice are that the mode value of the pore size increases from 203 to 302 μm and the overall distribution is shifted to a wider range. This has brought about a difference of 3.4% in their intrinsic permeability property as investigated in Chapter 3.

5.2.2 Model Theory

5.2.2.1 Projection Method – CFD Model

N-S equations (Equation 5-1) together with the continuity equation (Equation 5-2) are used to fully describe the fluid flow system within the Ti structure. They are repeated here for convenience:

$$\frac{\partial(\rho \boldsymbol{u})}{\partial t} + \nabla \cdot (\rho \boldsymbol{u}\boldsymbol{u}) = -\boldsymbol{\nabla} P + \mu \nabla^2 \boldsymbol{u} + S \qquad \textbf{5-1}$$

$$\frac{\partial \rho}{\partial t} + \nabla \cdot (\rho \boldsymbol{u}) = 0 \qquad \textbf{5-2}$$

where ρ is the fluid density and $\boldsymbol{u}$ is the fluid velocity, P is the pressure, μ is the dynamic viscosity of the fluid and S is the source term.

The N-S equations were solved using a projection method (Kim and Moin 1985) based on a finite volume defined on a staggered grid, which was modified from Chorin (Chorin 1968). Assuming incompressible Newtonian fluid with laminar flow in the

bone ingrowth system, the continuous equations are discretised using a first order explicit method as:

$$\frac{\boldsymbol{u}^{n+1}-\boldsymbol{u}^{n}}{\Delta t}+H(\boldsymbol{u}^{n})=-\frac{G(p^{n})}{\rho}+\frac{\mu L(\boldsymbol{u}^{\boldsymbol{n}})}{\rho}+S^{n} \qquad \textbf{5-3}$$

with

$$D(\boldsymbol{u}^{n+1})=0 \qquad \textbf{5-4}$$

where $\boldsymbol{u}$ is the discrete velocity, P is the discrete pressure, H is the discrete convective operator, G is the discrete gradient, L is the discrete Laplace operator and D is the discrete divergence operator.

The momentum equation (Equation 5-3) is first solved for an intermediate velocity, $\boldsymbol{u}^*$, which is an approximation of $\boldsymbol{u}^{n+1}$:

$$\frac{\boldsymbol{u}^{*}-\boldsymbol{u}^{n}}{\Delta t}+H(\boldsymbol{u}^{n})=-\frac{G(P^{n})}{\rho}+\frac{\mu L(\boldsymbol{u}^{\boldsymbol{n}})}{\rho}+S^{n} \qquad \textbf{5-5}$$

Note that this velocity, $\boldsymbol{u}^*$, will not satisfy the continuity equation (Equation 5-4). A velocity correction must be applied:

$$\boldsymbol{u}^{n+1}=\boldsymbol{u}^{*}-\frac{G\varphi}{\rho}\Delta t \qquad \textbf{5-6}$$

where φ is a pressure correction, such that the LHS of Equation 5-6 satisfies continuity.

Substituting Equation 5-6 into Equation 5-4:

$$D(\boldsymbol{u}^{*})-D\left(\frac{G\varphi}{\rho}\Delta t\right)=0 \qquad \textbf{5-7}$$

By rewriting Equation 5-8, a Poisson equation (Equation 5-8) for the pressure correction term, φ, is obtained by

$$L(\varphi)=D(G\varphi)=\frac{\rho D(\boldsymbol{u}^{*})}{\Delta t} \qquad \textbf{5-8}$$

The pressure correction term is then solved and the pressure is updated as:

$$P^{n+1}=P^{*}+\varphi \qquad \textbf{5-9}$$

where P^* is the intermediate pressure.

Equation 5-5 is then solved again using new pressure to obtain a new corrected velocity at the n+1 time, and the new approximated velocity is again corrected with a

pressure correction term to enforce the continuity. The process is repeated until the solution to Equation 5-5 is converged.

5.2.2.2 Finite Difference (FD) Model - Shear Stress Estimation

A finite difference (FD) technique is employed in the shear stress estimation (Atwood and Lee 2003; Lee *et al.* 2004). The FDM employed in this model runs on the same staggered grid mesh as the flow simulation. A simple 2D illustration of the grid is shown in Figure 5-1.

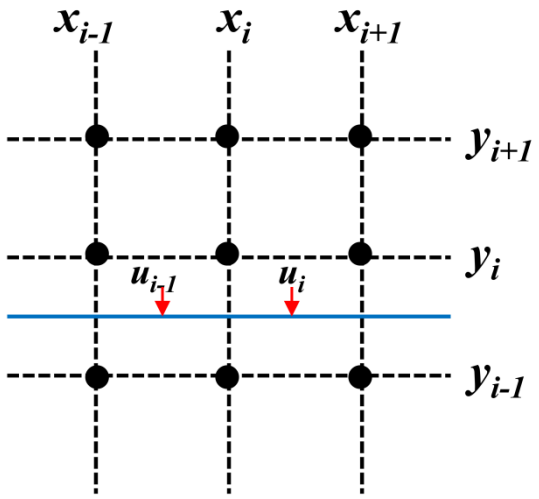

Figure 5-1 2D illustration of the staggered grid to show the concept of the model: the solid black circles indicate the pressure locations, the velocity components are defined at the centre of each cell, dotted lines represent the boundary faces of the cell.

Velocity components are specified at the centre of each cell, and gradients were evaluated linearly along velocity nodes to the cell boundary face. The estimation of velocity gradient used a forward difference based on a first order linear estimation:

$$\Delta \boldsymbol{u} = \frac{\boldsymbol{u}_{i+1} - \boldsymbol{u}_i}{\Delta x} \qquad \textbf{5-10}$$

where Δx is the grid size.

5.2.2.3 Cellular Automata (CA) Method – Bone Ingrowth Simulation

A cellular automaton (CA) is an array of discrete variables such as space, time, velocities etc. that follow local interaction rules (Wolfram 1986). Initially in the CA model at time step *t*, each meshed cell is assigned a 'state' to represent for example, a liquid or a solid status. For each cell, a set of neighbourhood cells is defined to be relative to the specified cell. A new array is created at time step *t*+1 according to some

fixed rule (e.g. a mathematical function) that determines the new state of each cell which is a function of the current state of the cell and the states of its neighbourhood cells. Generally, every cell has the same rule for updating the status. Each time the rule is applied to the whole grid simultaneously and a new array is created.

The CA concept has been widely used for modelling physical systems in materials science (Wolfram 1998). The bone ingrowth simulation illustrated here is a similar concept to the growth of dendritic crystal model developed by Atwood *et al*. (Atwood and Lee 2003) and Wang *et al*. (Wang *et al.* 2003). The model was successfully extended by Yuan *et al*. (Yuan and Lee 2010; Yuan *et al.* 2009) to model the interdendritic fluid flow effect on the dendritic growth. The model has been adapted as a point model with a specific ODE describing the change in a quantity, which the status of the cell will then depend on. Each cell in the bone ingrowth model has one of the three possible statuses: liquid, solid or growing interface. The propagation of state of the cells from 'fully liquid' to 'growing interface' to 'fully solid' is determined by the amount of cellular growth, which depends on the ingrowth rule incorporated with the flow induced-shear stress. In the next section, details of the cellular growth simulation will be discussed.

5.2.3 Model Theory - Simulation

5.2.3.1 Momentum and Mass Transport

A microscale model was developed to study the flow-induced shear stress and the bone ingrowth that solves the N-S equations interactively with the growth of the bone. The CFD model employed here was based on a prior 3D open-source microscale solidification model, μMatIC, which incorporated momentum and mass transport in liquid-solid phases (Wang *et al.* 2003; Yuan and Lee 2010). Therefore, only a summary of how the mass transport was simulated in the model is given below (for details see (Dong and Lee 2005; Lee *et al.* 2002; Lee *et al.* 2004; Wang *et al.* 2003; Yuan and Lee 2012; Yuan *et al.* 2009)) with details of the development of fluid shear stress evaluation and henceforth bone ingrowth prediction.

The flow occurring through porous media materials was assumed to be laminar and the fluid was incompressible and Newtonian. Based on the control volume fixed in space, the conservation of momentum takes the form (Patankar 1980):

$$\frac{\partial \boldsymbol{u}_l}{\partial t} + \nabla \cdot (\boldsymbol{u}_l \boldsymbol{u}_l) - \frac{\mu}{\rho} \Delta \boldsymbol{u}_l = -\frac{1}{\rho} \nabla P \qquad \textbf{5-11}$$

where $\boldsymbol{u}_l$ is the velocity vector in fluid, t is the time step, P is the pressure, ρ is the fluid media density and μ is the fluid media viscosity. In order to unify the equation in the entire domain including fluid, bone and growing cells, the velocity field was defined as

$$\boldsymbol{u} = f \boldsymbol{u}_l \qquad \textbf{5-12}$$

where f is the fraction of fluid in a single controlled volume. Note that the change in f was assumed to be slow compared to changes in the flow velocity. When f = 1, the volume represents pure fluid in the porous space; when f = 0, it represents the bone structure itself, which ensures $\boldsymbol{u}$ = 0 in the bone; and when 0 < f < 1, it represents the growing cell at the surface. Therefore, this transition from fully liquid (f = 1) to fully dense bone (f = 0) can represent the deposition of osteoblasts and their subsequent densification.

The conservation of mass equation, therefore, applied:

$$\nabla \cdot \boldsymbol{u} = 0 \qquad \textbf{5-13}$$

The flow governing equations above were solved by a projection method described above based on the regular orthogonal grid mesh using a control volume method. The pressure Poisson equation deduced in the projection method was solved using the preconditioned conjugate gradient solver. In order to take into account the momentum sink at the bone/fluid interface, the standard projection method was modified in the following way. The intermediate velocity, $\boldsymbol{u}$*, explicitly evaluated from the previous time step and the pressure gradient ∇P were multiplied by the liquid fraction to obtain the new velocity, $\boldsymbol{u}^{n+1}$.

$$\boldsymbol{u}^* = f\left(\boldsymbol{u}^{\mathrm{n}} + \Delta t F(\boldsymbol{u}^{\mathrm{n}})\right) \qquad \textbf{5-14}$$

$$\boldsymbol{u}^{\mathrm{n+1}} = \boldsymbol{u}^* - f \Delta t \nabla P \qquad \textbf{5-15}$$

where F is the discrete convection and diffusion term in the N-S equations. The method has been validated against analytical solutions (Al-Rawahi and Tryggvason 2002). This modification does not introduce extra computational effort but provides a dynamic solution to the transient growth of the bone.

5.2.3.2 Shear Stress and Bone Ingrowth Model

This part of the model was developed within this study and implemented in the existing μMatIC code. Shear stress on the bone surface was calculated through the velocity gradients neighbouring the growing cells. Based on the definition of fluid shear being the components of stress coplanar with the cross section of a control volume (Granger 1995), the shear stress component in *x* direction was defined as:

$$\boldsymbol{\tau}_x = 2\mu\sqrt{\left(\frac{d\boldsymbol{v}}{dz}\right)^2 + \left(\frac{d\boldsymbol{w}}{dy}\right)^2} \qquad \textbf{5-16}$$

where $\boldsymbol{v}$ and $\boldsymbol{w}$ are the velocity tensors on the tangential plane of the fluid flow. A similar definition is then applied to $\boldsymbol{\tau}_y$ and $\boldsymbol{\tau}_z$.

The local shear stress magnitude was calculated as:

$$\tau = \sqrt{\boldsymbol{\tau}_x{}^2 + \boldsymbol{\tau}_y{}^2 + \boldsymbol{\tau}_z{}^2} \qquad \textbf{5-17}$$

For a simpler calculation and less intensive computational requirement, the subsequent cell growth rule was set to be a simplified linear relationship with the shear stress (original reference of the concept in (Liu *et al.* 2012)) . The absolute growth (%) on each cell, i.e. the fraction of solid that are taking into account as the growing bone is defined as:

$$g_i = f(\tau, t) = A\tau\Delta t \qquad \textbf{5-18}$$

where *A* is a constant, termed as the growth factor; Δt is the time step. The value of the growth factor, *A*, was chosen so that the maximum growth rate matches previous recorded value in literature (Chung *et al.* 2007; Freed *et al.* 1994).

5.2.3.3 Parameters and Initial / Boundary Conditions

Figure 5-2 shows the schematic of the boundary and initial conditions used in the simulations. A fully liquid region is placed up- and down-stream to act as a fluid buffering zone and to allow the flow to stablise on the upwind and downwind flow faces. Up / down-stream end faces of the buffer zone in the desired flow direction were set as fluid inlet/outlet boundaries. Four different constant inflow velocities, 0.02, 0.05, 0.1 and 0.2 mm/s were simulated (note all producing laminar, low Reynolds number flows). A pressure outlet was imposed on the outlet boundary. A no-slip condition was used on the pre-defined bone-fluid interface and zero-flux on other bounderies.

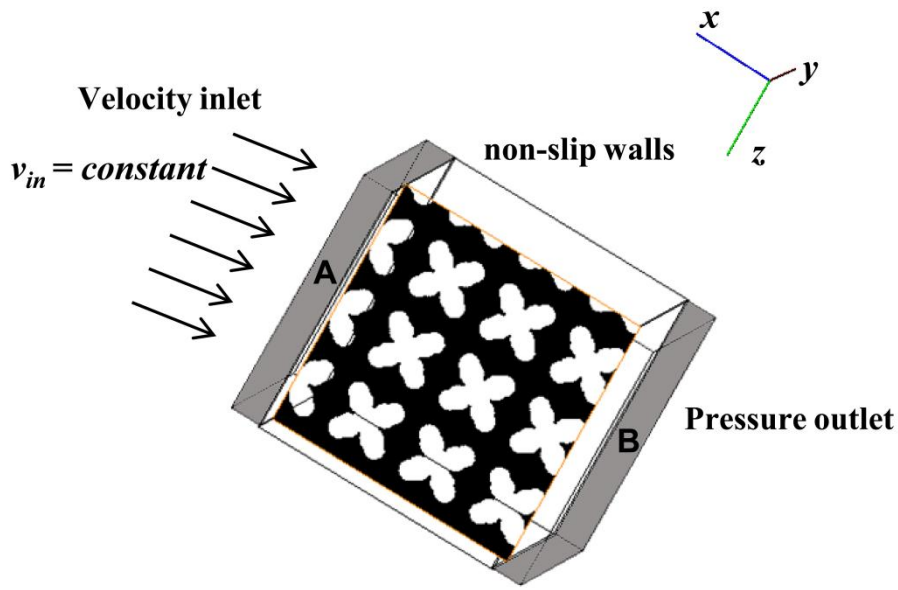

Figure 5-2 Schematic of the flow system used for the bone ingrowth simulation: regions A&B are fluid buffer zones; boundary and initial conditions are labelled.

The other simulations parameters are given in Table 5-1. The inflow velocities were chosen based on values used in similar numerical studies in literature for ease of comparison. A mesh grid size of 36 µm was chosen for better simulation efficiency. The dimension of the sample was kept the same as the previous CFD study on permeability to ensure that the REV of the structure was included in the simulation.

It should also be noted that, as previously reported by Cartmell *et al.* (Cartmell *et al.* 2003) and Raimondi *et al.* (Raimondi *et al.* 2006), shear stress greater than 0.05 mPa will promote the cell proliferation/stimulation while a shear stress exceeding 56 mPa causes cells to be washed out and therefore slows down the cellular growth rate. A minimum and a maximum shear stress constraint were incorporated in the model. In this case, the growth vanishes when the calculated shear stress magnitude is less than 0.05 mPa or greater than 56 mPa (i.e. the growth factor is set to be zero when the shear is out of range). The ingrowth simulation was run both with and without the upper constraint 56 mPa so that the effect of high shear stress on decreasing the cell growth can be quantified.

Table 5-1 List of simulation parameters used in the numerical model:

Property	Value	Unit	References
Initial inflow velocity (v_{in})	2×10^{-5} 5×10^{-5} 1×10^{-4} 2×10^{-4}	m/s	Liu *et al*. (Liu *et al.* 2012) Raimondi et al. (Raimondi *et al.* 2011)
Medium density (ρ)	1009	kg/m^3	Coletti *et al.* (Coletti *et al.* 2006)
Medium viscosity (μ)	8.4×10^{-4}	kg/ms	Coletti *et al.* (Coletti *et al.* 2006)
Growth factor (A)	1.5×10^{-4}	---	Based on Liu *et al*. (Liu *et al.* 2012)
Max growth rate	1.5×10^{-5}	s^{-1}	Coletti *et al.* (Coletti *et al.* 2006)
Min (critical) shear stress (τ)	0.05	mPa	Cartmell *et al*. (Cartmell *et al.* 2003)
Max shear stress (τ)	56	mPa	Raimondi *et al*. (Raimondi *et al.* 2006)
Grid size	36	μm	

5.3 Results

The model is applied to calculate the bone ingrowth in the regular and 30% randomised structures with similar porosities characterised based on the 3D CAD design. For each sample, the velocity profiles, the shear stress magnitude and distribution, the pressure drop, the growth rate and corresponding volume fraction of bone ingrowth over 120 hours at each inflow velocity were calculated.

The overall pressure drop in both implant structures at inflow velocity of 0.02 mm/s are shown in Figure 5-3. Pressure in the 3D volume of the regular design (0% randomisation) varies from 0 to 1.5 mPa. Simulation in the 30% randomised structure reveals a maximum pressure variation 2.4 times greater than the regular due to the uneven distribution of velocities of fluid passing through more torturous channels. 2D slices of *yz*-planes are selected at the centre to show the velocity and shear stress distributions in Figure 5-4.

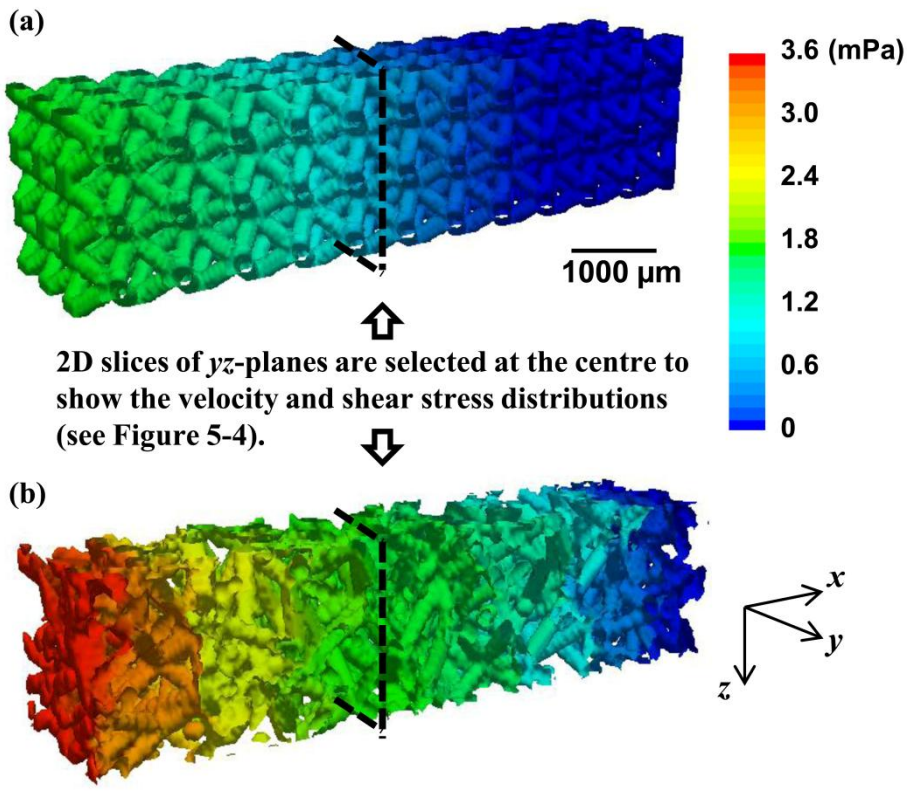

Figure 5-3 3D volume images showing the overall pressure changes in (a) the regular and (b) the randomised structures. (Inflow velocity: 0.02 mm/s, time point: 0hrs)

Figure 5-4 shows the 2D cross-sectional view of velocity and shear stress distributions at the centre of both (a) regular and (b) 30% randomised structures when the inflow velocity is 0.02 mm/s. In the regularly ordered implant structure, higher velocity flow occurs in the narrow channels with weak flow in the open channel (labelled as region '**(N)**' in Figure 5-4 (a)). The shear stress is almost zero in '(N)' regions. The maximum values of velocity along the flow direction within the regular (0.13 mm/s) and randomised structures (0.16 mm/s) exhibit a difference of 23.1%. The average velocity throughout the entire structure is also compared: the 30% randomised structure has a higher average velocity value of 22.7% greater than that of the regular structure at the final stage of growth. Higher shear stress values are seen at the locations where the changing in velocity is significant. The maximum value of shear applied on the solid in the randomised structure is 3.4 times greater than the regular one. Note that CFD simulation in FLUENT on same structures without bone ingrowth were performed to validate the initial stage results, and the overall pressure changes and velocities agreed with each other within same order of magnitude.

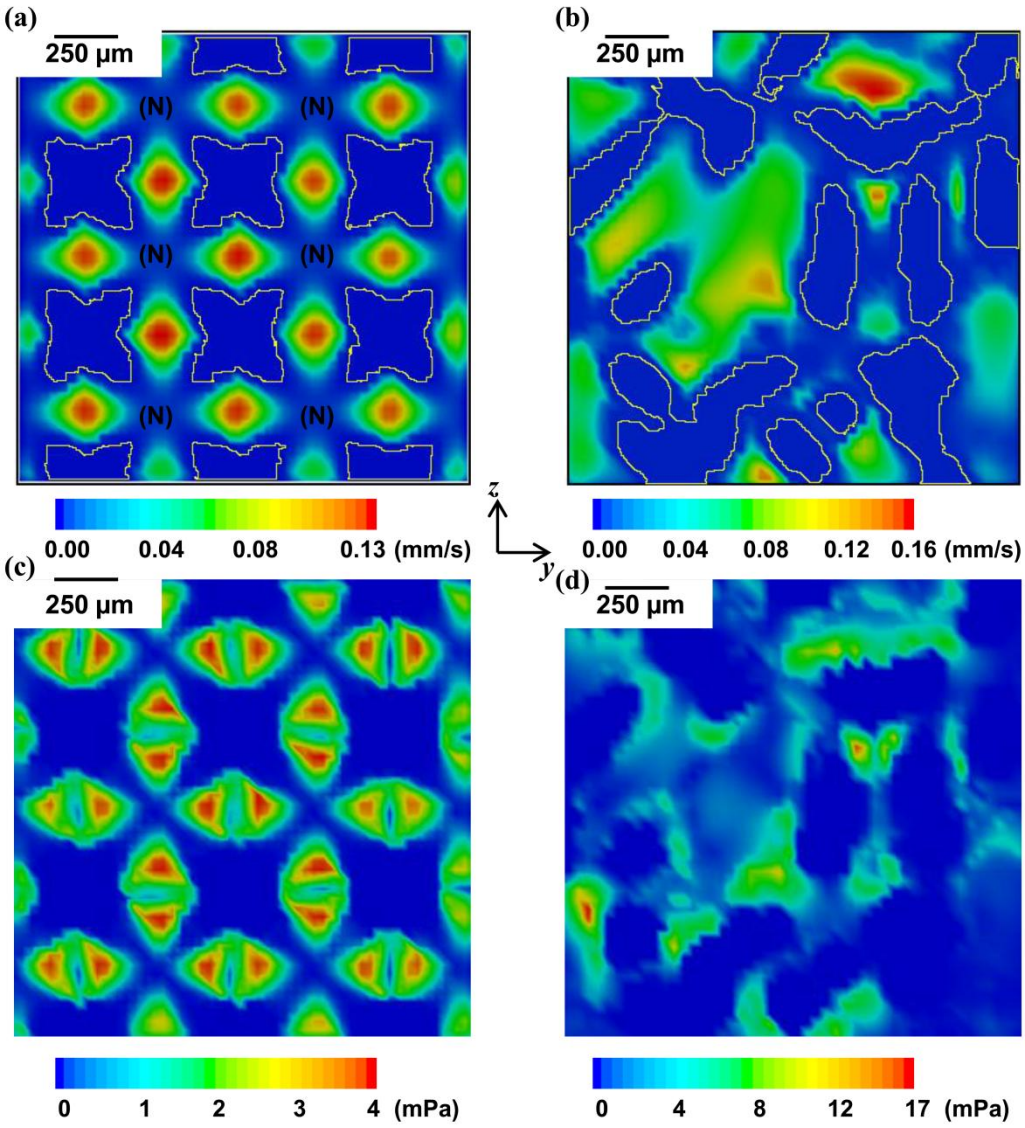

Figure 5-4 (a) & (b):2D cross-sectional views of local velocity distributions in the regular and 30% randomised structures. (c) & (d): 2D cross-sectional views of local shear distributions in the two structures. (Inflow velocity: 0.02 mm/s, time point: 0hrs)

The distributions of local shear stress throughout the regular and randomised implants are shown in Figure 5-5 as fluid volume normalised histograms. Shear stress values corresponding to all the interfacial cells are counted and normalised by the total fluid volume. Five key parameters are extracted in Table 5-2: the mean, standard deviation of shear stress and the mode, skew and kurtosis of the distribution at both early and final growth stages. The strong influence of inflow velocity and strut structure on local shear stress is clearly shown. In the regular structure, more local cells have higher shear stress with the increase of inlet velocity. This trend is also shown for the randomised structure. However, in the 30% randomised structure, both the shifts in modal values of the shear stress from 2.6 to 71.1 mPa at early stage and 5.8 to 71.1 mPa at final stage, which is

revealed to be greater ranges than those in the regular structure ((Figure 5-5 (b)). Skewness measures the concentration of the shear stress in the distribution. In both regular and randomised structures, lower inflow velocity cases showed moderate changes from approximately symmetric to slightly positively skewed distributions. For higher inflow velocity, the shear distribution became highly skewed (skewness greater than +1) towards the higher stress region as the time increases, indicating high shear stress concentration due to larger amount of deposited bone cells compared to the low velocity cases. Kurtosis gives information on how the height and sharpness of the peak of the distribution compare to the shape of a normal distribution. The range of shear in the regular structure narrowed more significantly compared to the randomised structure, suggesting constrictions in open channels causing localised stress concentration.

Table 5-2 List of key parameters obtained from shear stress distribution at final growth stage.

	Inflow velocity (mm/s)	**Regular**		**Randomised**	
		16.7 hrs	**120 hrs**	**16.7 hrs**	**120 hrs**
Mean shear stress (mPa)	0.02	4.3	6.7	3.9	6.4
	0.05	13.1	18.5	12.2	19.0
	0.1	30.3	50.1	29.3	48.0
	0.2	66.9	105.2	66.9	90.4
Mode shear stress (mPa)	0.02	5.3	10.2	2.6	5.8
	0.05	11.3	24.5	12.3	12.3
	0.1	35.3	35.3	20.2	54.9
	0.2	60.6	60.6	71.1	71.1
Standard deviation ($\times 10^{-3}$)	0.02	4.6	6.9	4.8	7.6
	0.05	14.6	20.9	15.9	28.3
	0.1	34.1	86.6	39.3	85.1
	0.2	75.7	304.1	90.9	162.3
Skew	0.02	0.3	0.5	0.7	0.8
	0.05	0.5	0.5	0.8	1.0
	0.1	0.8	1.2	0.9	1.3
	0.2	0.8	1.4	0.9	1.3
Kurtosis	0.02	-1.5	-0.6	-1.1	-0.9
	0.05	-1.4	-0.8	-0.9	-0.4
	0.1	-0.5	1.4	-0.7	0.4
	0.2	-0.5	0.9	-0.8	0.6

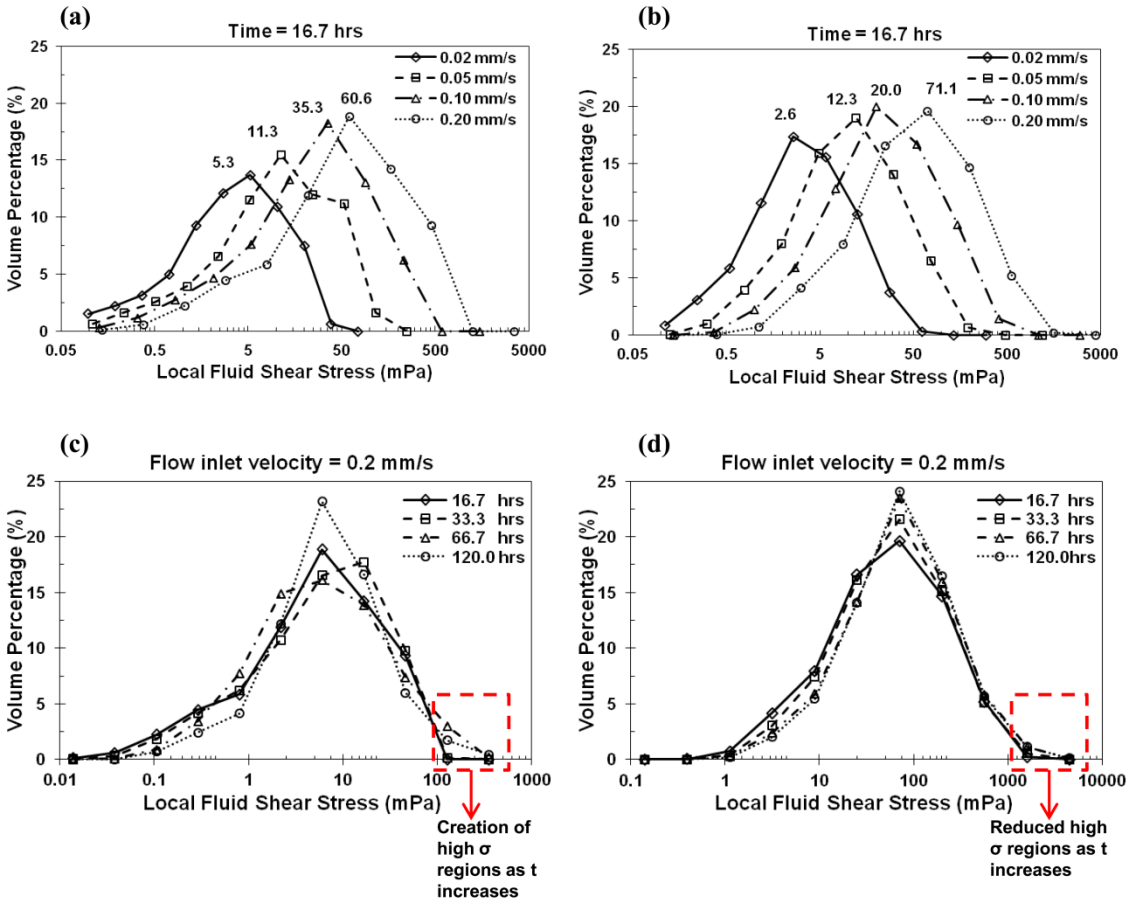

Figure 5-5 Local shear stress histogram distributions at different time points with the vertical axis showing the frequency density with a given shear range (log-based bin range). (a) & (b) At time point 16.7 hrs, shear distributions at four different inflow velocities in the regular and 30% randomised structures. (c) & (d) At inflow velocity 0.2 mm/s, shear distributions at four different time points in the regular and 30% randomised structures.

In the regular structure, at earlier time points up to 16.7 hours (Figure 5-5 (a)), a factor of 10 increase of the inflow velocity (0.02 to 0.2 mm/s) causes a 11.4 times increase in the mode of the shear stress (5.3 to 60.6 mPa). Although shear stress distributions at later time points, especially in the regular structure, show a less steep increase in the mode of the shear, there is a large difference in distributions between the regular and randomised structures at higher inflow velocities. For example, in Figure 5-5 (c) and (d), significant reduction in regions with high shear stress values (> 1500 mPa) is found in the randomised structures as time increases. And the randomised structure has a broader distribution of shear with a maximum shear stress of 1.7 times larger than the regular structure.

A comparative plot of volume fraction of bone ingrowth over time in the two structures is shown in Figure 5-6 (a). A 10-fold increase in inflow velocities causes a 9 times

increase in bone ingrowth (1.9 to 17.5%) in the regular structure after 120 hours while in the randomised structure, bone growth is initially similar for all inflow velocities, but after 60 hours, it shows a faster bone ingrowth with a 11.5 times increase in bone volume (1.7 to 19.5%).

Several prior experimental studies suggested that there is also a maximum shear stress beyond which osteoblasts will not attach and there will be no bone formation. This is simulated by applying the upper shear constraint for bone ingrowth. Results in Figure 5-6 (b) show significant decreases in bone growth by 80.1% and 81.0% in the regular and 30% randomised structures with the constraint of maximum shear value, 56 mPa, respectively. Furthermore, by comparing the two structures, it is found that an 8.8% more decrease of bone ingrowth volume fraction is found in the randomised structure.

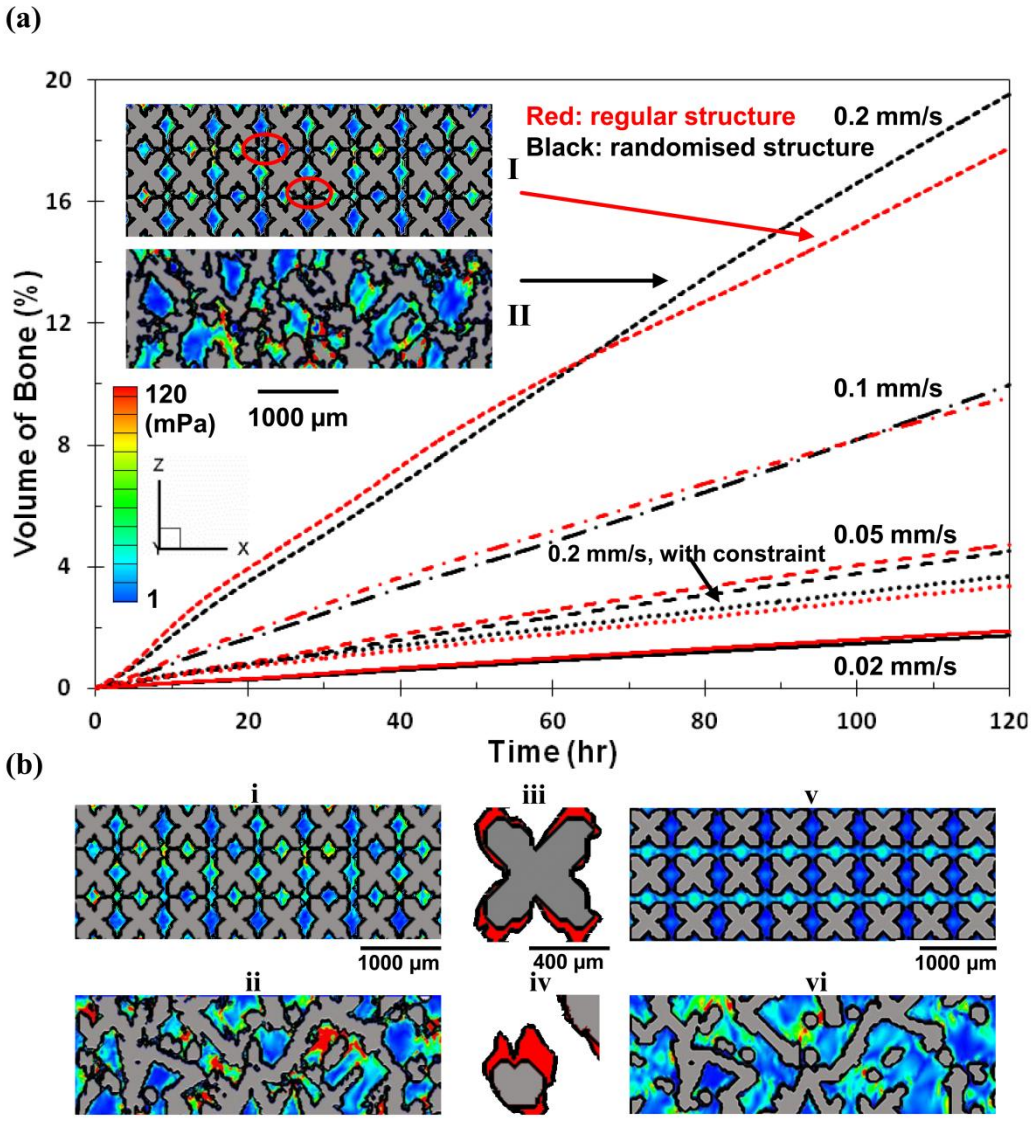

Figure 5-6 a) Comparative plot of bone ingrowth vs. time between the regular and 30% randomised structures at different inflow velocities. Insets: I showing the blockage of the channels in the regular structure at later time stage; II showing the concentration of shear stress in the randomised structure, where indicates more ingrowth at later stage of growth after 70 hrs. (b) Effect of maximum shear constraint on bone ingrowth at inflow velocity of 0.2 mm/s in the regular and 30% randomised structures. (i) & (ii) showing the final growth at 120 hrs without capping the shear stress. (iii) & (iv) showing zoomed in features of bone growth (coloured red). (v) & (vi) showing the final growth at 120 hrs with the shear constraint. Contour coloured by shear stress.

The comparison of the total volume fraction of bone ingrowth without constraints in both structures is shown in Figure 5-7 as a function of the average local shear stress (volume and time averaged). Both regular and 30% randomised structures show similar ingrowth at inflow velocities less than 0.1 mm/s; however by looking at the shear distributions in the 3D structures, factors which may hinder the ingrowth in the regular and randomised structure appear differently, and are discussed in the following section.

At an inflow velocity of 0.2 mm/s, the regular structure experiences higher average shear stress due to channels being blocked by fast deposited cells and therefore shows less increase in bone volume fraction at late stage when compared to the randomised structure.

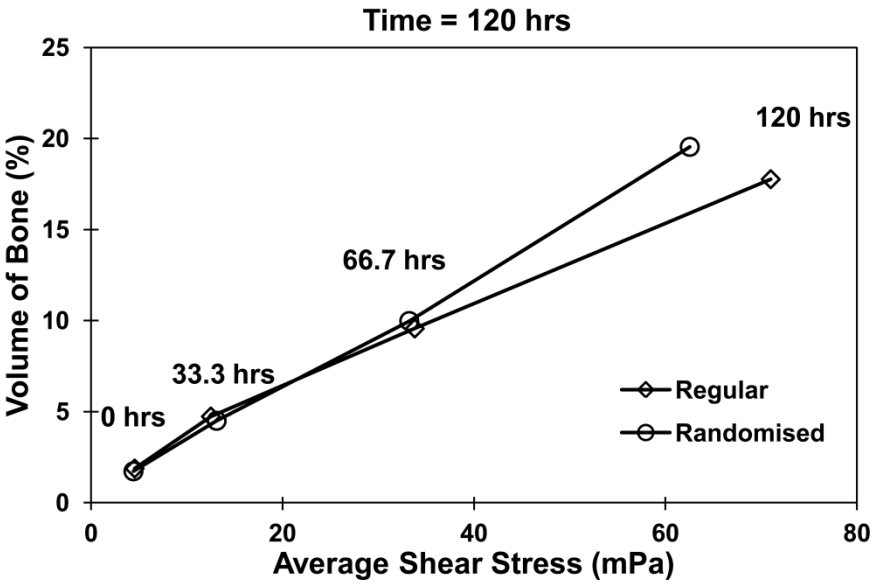

Figure 5-7 Comparison between the regular and 30% randomised structures at final stage of growth: volume fraction of bone ingrowth vs. average shear stress at different flow inlet velocities (without shear constraint).

Figure 5-8 shows the comparison of average shear stress and average growth rate at different time points between the regular and 30% randomised structures with increasing inflow velocities. At all velocities, the 30% randomised structure was found to have more stabilised growth rate at larger time points (typically > 40 hours) compared to the regular structure. A maximum of 19% of the variation in growth rate after 40 hours was found in the randomised structure while a decrease of 20 – 44% in growth rate was predicted in the regular model.

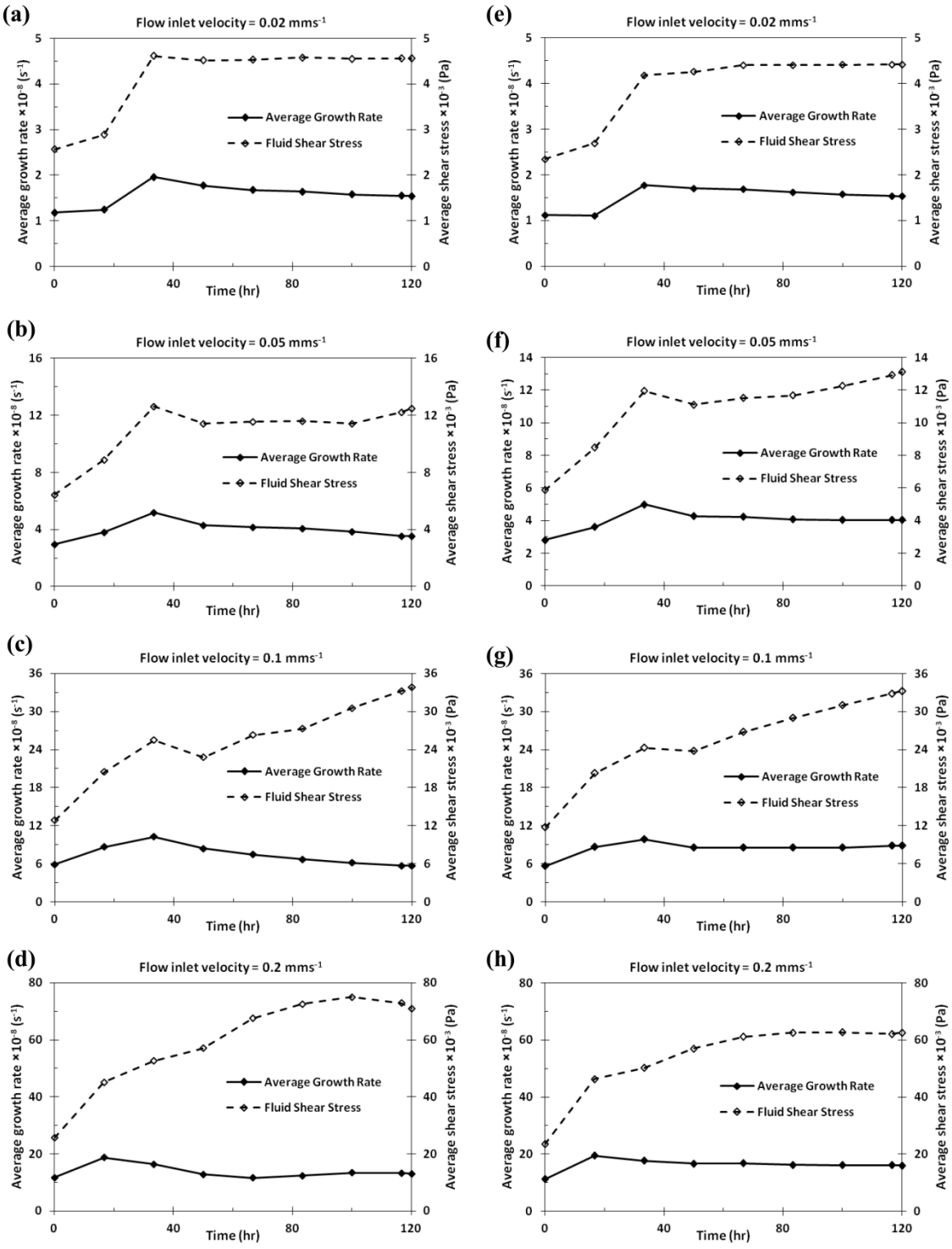

Figure 5-8 Comparison of average shear stress and average growth rate at different time points between the regular and 30% randomised structures (without shear constraint): (a)-(d), regular structure with increasing inflow velocities; (e)-(h), 30% randomised structure with increasing inflow velocities.

The comparison of overall growth rate (calculated by averaging the growth rates at all the time points) for regular and randomised structures is shown in Figure 5-9. It suggests that at velocities greater than 0.5 mm/s, the randomised structure would exhibit a generally better performance of bone ingrowth under the prevalence of the fluid flow induced shear stress.

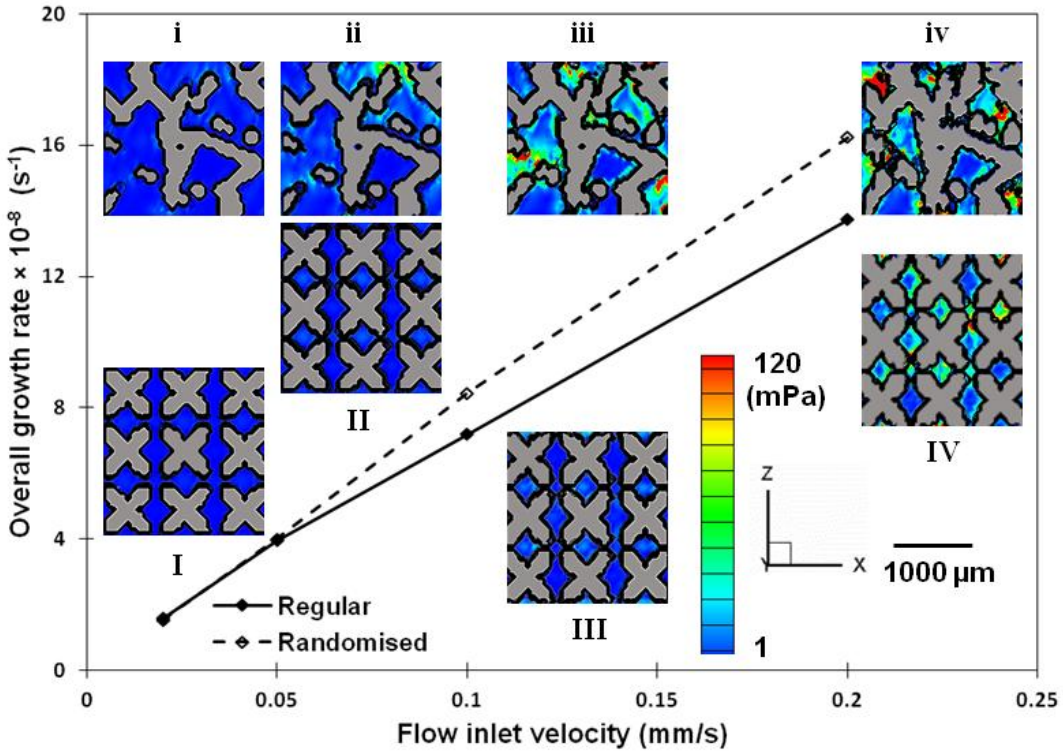

Figure 5-9 Comparison between the regular and 30% randomised structures: overall growth rate (average value at different time points) vs. inflow velocity (without maximum shear constraint). Inset: I, II, III & IV showing final growth in the regular structure; i, ii, iii & iv showing the final growth in the randomised structure. Contour coloured by shear stress.

5.4 Discussion

A numerical model is presented which simulates the microscopic flow shear stress and cell growth, reveals for the first time their complex inter relationship as osteogenesis occurs, especially at a microscopic level. Although a few prior computational approaches have been proposed to evaluate the shear stress on porous scaffold surfaces (Chung *et al.* 2007; Cioffi *et al.* 2008; Maes *et al.* 2010; Raimondi *et al.* 2006), and after imposed bone deposition (Lesman *et al.* 2010), the time dependent changes in flows and distribution of bone ingrowth have not, to our knowledge, been previously simulated. This model is applied to study complex 3D AM structures, allowing

quantitative prediction of the effect of shear stress distribution within the real implant structure on cellular growth, and locates the actual areas where the cellular response takes place.

5.4.1 Model Validation

The numerical model was compared with the FLUENT CFD model in Chapter 3 (Figure 5-10). The results from the current model match well with the FLUENT prediction of velocity components and permeability.

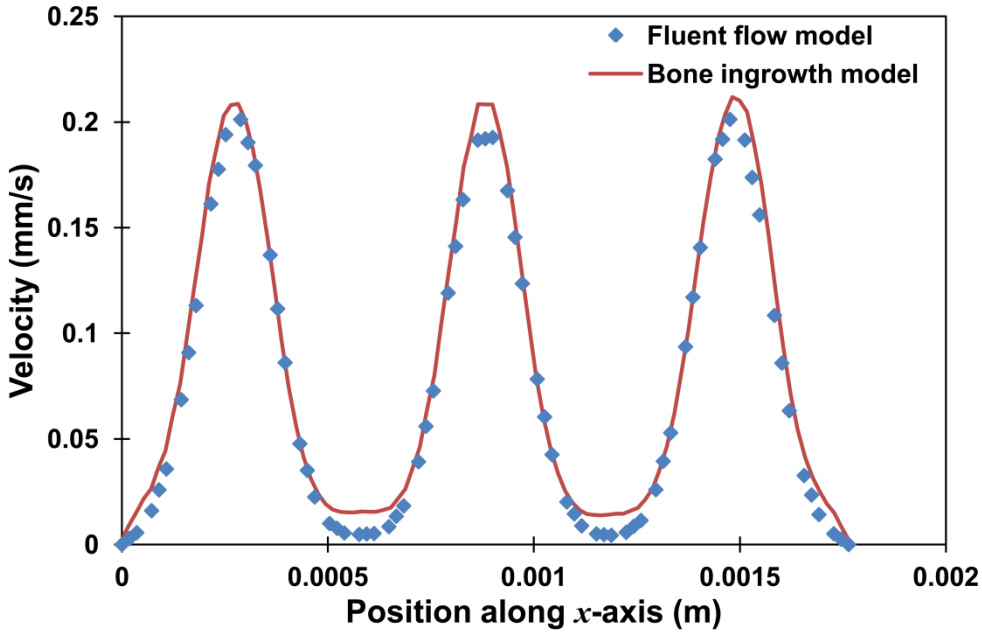

Figure 5-10 Plot of the velocity components in flow direction (*x*-direction) through the central line of the domain in both FLUENT and numerical bone ingrowth model.

Comparison with the literature is not straightforward since the shear stress estimation will be greatly affected by the choice of simulation parameters and the porosity/microstructure of the structure being tested. Our predicted levels of shear stress agree reasonably well with Raimondi *et al.*'s work (mean shear stress of 16 mPa at an inlet velocity of 0.22 mm/s) (Raimondi *et al.* 2006). Compared to Maes *et al.*'s work (Maes *et al.* 2009) at similar inflow velocity (0.03 mm/s), the average stresses were the same order of magnitude (1.4 mPa). The amount of ingrowth at five days agrees with Raimondi *et al.*'s prediction but a direct comparison is not possible as the void fraction and shear stress levels were not given in that publication. Note that although simulation was performed up to an inflow velocity of 0.2 mm/s for comparison, at velocity above

0.1 mm/s the shear stress predicted will be too high for cell attachment (Raimondi *et al.* 2006).

5.4.2 Local Shear Stress Distribution and its Impact on Bone Ingrowth

The model was applied to investigate the local shear stress distribution within two types of implant structures, regular and 30% randomised with four different fluid inflow velocities. As shown in Figure 5-4 (c) and (d), the randomised structure had a much broader range of shear stress (maximum shear is > 4 times that of the regular structure). The distribution of the shear stress in the regular structure showed a regular pattern with relatively high local stress concentration in strut channels, but little shear in areas within pores. This promotes bone growth in the narrow channels, but not across the bulk of the regular structure. In the randomised structure, the fluid flow was more evenly distributed (Figure 5-4 (b)).

Analysis of shear stress histograms at various time points reveals that in the regular structure, the distribution of shear varied more significantly than in the randomised structure, especially at later stages of growth (see Figure 5-5 (c) and (d)). At lower inflow velocities (0.02 mm/s and 0.05 mm/s), there was a two-fold increase in the mode of the shear stress with increasing time during early stage of growth. At higher inflow velocities (0.1 mm/s and 0.2 mm/s), a three-fold increase in the mode of the shear stress took place in the middle stage of the growth. However, after about 9% bone ingrowth, the growth rate (mode) dropped and the distribution narrowed. As the bone ingrowth continues, high stress regions were formed (regions with shear greater than 1000 mPa). This indicates that in the regular structure, the cellular growth which results in a greater bone layer thickness, may cause constrictions in the interconnect regions, which further reduces shear in the bulk regions (pores).

In the randomised structure, at all inflow velocity magnitudes, the shear stress distributions showed a similar skew trend at all time points. This demonstrates that in this particular structure arrangement, the cellular growth followed similar paths in the naturally formed preferential flow channels. Generally, the magnitude of shear stress increased as the bone grows. The average growth rate decreased as bone volume accumulates, indicating that the impact of shear on cellular growth diminishes as the shear experienced by cells decreases. The results indicate that the internal structural difference may be useful for the bespoke design of implants. For example, at earlier

stages of implantation, the structural flow-channels need to be formed to serve as a 3D template for guiding the desired bone ingrowth. More uniformly distributed shear with a stable average magnitude may be required during later treatment period.

The total amount of bone ingrowth in both types of structures is compared at different inflow velocities (Figure 5-6). In general, the amount of cellular ingrowth is directly proportional to the inflow velocity. In the regular structure, the growth increased almost three-fold from 1.8 to 4.7%, at inflow speed from 0.02 to 0.05 mm/s. For the randomised design, the result showed similar volume fraction of bone ingrowth as the regular structure for inflow velocities < 0.1 mm/s. However, at high flow velocities and longer times, the rate of ingrowth in random structures increased by 11% over the regular strut architecture. This finding can be explained by the fact that in the regular structure, due to the ordered design, there are channels where there is little flow in contact with the struts wall and therefore less shear, resulting less amount of bone ingrowth in those areas. Also at later stage of the growth, the prevalence of equally constricted channels in the regular design, due to the localised growth of bone, can hinder the subsequent growth more noticeably. The presence of narrowed channels causes large amounts of flow media to be forced to pass through a relatively small part of the entire void space. This implies that narrow flow channels may result in less vascularisation and transportation of oxygen and nutrients in the implant so that part of the desired ingrowth amount is compromised in this case.

Raimondi *et al.*(Raimondi *et al.* 2006) suggested that beyond a certain shear stress magnitude, cells would be washed out hence the growth might be hindered. In order to examine the potential of excessive shear stress on cellular growth, our numerical model with maximum shear constraint provides a quantitative result on the effect of its cell wash out effect. The simulation with the highest inflow velocity was picked to examine the impact of the maximum shear on cellular growth. It was found that with the maximum shear stress constraint, the amount of ingrowth decreases significantly in both designs (by more than a factor of 5). This suggests that the high inflow velocity (0.2 mm/s) simulation results might be unrealistic. The impact of maximum shear on bone ingrowth is still unclear, and further experiments need to be performed to understand the relationships, that can be used to find the best perfusion inlet velocity and correlate this finding to the bone growth rate.

The relationship between the volume fraction of bone ingrowth and the shear stress is shown in Figure 5-7. Local shear stress increases with the amount of new bone grown into the structure, which in turn blocks part of the flow channel, causing fluid to pass through narrower space, resulting in the increase of the fluid velocity in the porous structure and consequently the shear applied on surface cells. It is interesting to see that for the highest inflow velocity case, regular structures shows a higher local shear profile than the randomised structures for less bone ingrowth. This agrees with the observation that at high velocity, regular channels become blocked by fast deposited ingrowth, which results in a less optimal environment for later stage bone growth.

The comparison of average growth rate at different time points between the two structures in Figure 5-8 further confirmed the previous observation that the internal strut morphology of 30% randomised structure may have positive influence on later stage bone ingrowth.

From Figure 5-9, which shows the plot of average values of growth rate at different time points with different inflow velocities, it can be concluded that the overall growth rate depends, to a large extent, on the flow inlet velocity. Comparing the performance of the two types of structure, greater overall growth rate may occur at higher flow velocities in a randomised structure. However, the shear stress and the location of the ingrowth depend greatly on the internal structure at a micro level. Further simulations are required on a statistical basis to test the model on structures with different internal strut and pore morphology.

5.4.3 Limitations of the Model

Although the proposed linear cell growth function depending on shear stress has been used in the simulation, this function can be easily altered in the model as more data become available, such as dependency on local nutrient concentration, mechanical shear, etc. Also, the growth coefficient will depend on the choices of the culture fluid and cells. For the study of quantifying shear constraint effect on bone ingrowth, more appropriate growth function may be needed to avoid possible artefacts in flow behaviour caused by sharp drop of growth factor. For example, a nonlinear term for shear based removal of cells can be incorporated into the current linear function to accommodate the diminishing effect.

Further modification should be made to this microscopic model to include the nutrition and oxygen transport in order to provide more accurate results of bone ingrowth with local shear stress distribution once this data becomes available. Improvements such as a statistical analysis can be performed to further test the accuracy of the model by applying the model on different samples with same level of randomisation and also samples with different levels of randomisation, or only completely different structures, such as apatite foams (Jones and Hench 2003) or bioglass foams (Jones *et al.* 2006). In addition, the current model assumes laminar fluid flow inside the implant. However, modifications can be made to simulate pulsating flow inside body, which should more closely mimic the *in-vivo* situation.

Another limitation is a paucity of quantitative experimental validation data for these dependencies. At present, it is only possible to compare the average values of shear stress provided by macroscopic computational modelling results.

In summary, this study provides a microscopic evaluation of shear stress within the implant structure, and reveals direct quantitative results of cellular growth related to shear stress distribution. By simulating the flow in implants with different internal structures, the model provides potential guidelines to optimise the implant construction for stimulating bone ingrowth.

5.5 Conclusions

A microscale numerical model, based on the N-S equations, was developed to study the time dependent bone ingrowth and flow shear stress under two proposed AM Ti scaffold structures. The bone ingrowth as a function of time and shear was simulated in 3D structures on a microscopic scale for the first time and its subsequent influence on the flow was determined.

The influence of local fluid shear stress on bone ingrowth as a function of increasing inflow velocities, implant structures and time was investigated. The increasing inflow velocity enlarges the range of shear stress and has a positive relationship to the overall growth rate. The results indicate that the 30% randomised structure produces a much higher variation in flow shear than the regular structure. During initial stages of growth, this may not affect osteogenesis significantly; but interestingly as bone ingrowth progresses, the randomised structure sustains high growth rates due to preferential flow

channels forming. In the regular structure, localised growth may hinder the bone ingrowth at later stage which reduces the overall growth rate. Quantitative effect of excessive shear stress predicted that higher inflow velocities, greater than those shown in experiments, can be used as guidelines for designing the optimal perfusion rates in the cell culturing study. The model provided a viable tool that can be used to determine the influence of hierarchical structure design in AM Ti implants.

The CFD approach developed in this study can be used as another modelling tool in addition to the flow property and the FEA models reported in previous chapters to characterise porous orthopaedic implant materials. Combination of the three models and study on the interaction of flow, mechanical properties and bone ingrowth are expected to have a profound effect on the optimal design of implant in the medical research field.

6 Conclusions and Future Work

6.1 Conclusions

In this thesis, three computational models of porous titanium (Ti) foams produced by additive manufacturing (AM) were developed based on X-ray microtomography (μCT) imaging to characterise: (1). flow properties; (2). mechanical properties and (3). bone ingrowth. The applications of these models provided viable pathways to help predict the performance of the implant prior to manufacturing, making the evaluation of individual design factors on overall performance in the implant design process possible.

Firstly, using the μCT based in-house quantification technique and commercial computational fluid dynamics (CFD) model developed to simulate the flow inside the porous Ti implant, the following conclusions were made:

- The pore size of AM Ti implants made via the UC approach was found to be in the range 200 – 500 μm, which satisfies the requirements for transport and subsequent ingrowth. The pore size modal value increases as the randomisation level increases.
- The Navier-Stokes equations (N-S equations) based CFD method was combined with 3D non-destructive μCT imaging technique to characterise flow properties of the porous structure. The model, which was validated against experimental measurement, demonstrated its suitability to quantify the permeability of the Ti implants. Four structures of different levels of randomisation between 0 and 30% and a nominal porosity of 65% were tested. The CFD predicted permeability values ranging from 6.9×10^{-10} to 1.0×10^{-9} m^2 compare well with the previous studies of permeability of human trabecular bone.
- By comparing flows in both regular and 30% randomised structures, it was observed that structure variation has a profound effect on local flows. Preferential flow channels form much more readily in the randomised structure due to greater variations in channel width and pore size compared to the uniform channel size in the regular structure, giving a much greater range of local shear in the flow, which was later shown to stimulate bone ingrowth.

- Using the technique developed to voxelise the foam structure and to alter the design of the strut thickness / surface morphology, a computational tool has been developed to allow implant designers to independently vary the overall porosity and strut surface roughness, each having a separate effect on the permeability. This approach, combined with the AM technique, allows an engineered design, hierarchically tailored for producing desired flows in implants.

Secondly, a finite element analysis (FEA) model was developed to characterise the compressive properties of the implant. The following points were concluded:

- The model was applied on three different structures (regular, 30% randomised, mixed regular-randomised). The predictions of both the strength and modulus properties by FEA simulation agreed well with experimental measured and the literature values. This confirms that the viability of this computational approach to characterise the highly porous Ti structure used for orthopaedic implants.
- The regular structure has an effective elastic modulus of 1.7 GPa and a yield stress of 28 MPa. The 30% randomised structure has an effective elastic modulus of 2.1 GPa and a yield stress of 39 MPa. The implant with a mixed design exhibits an elastic modulus of 2.2 GPa and a yield stress of 30 MPa. The properties of these structures satisfy the typical requirement for implant used for orthopaedic applications.
- The comparison results showed that the randomised structure has better mechanical performance as compared to the regular structure. The failure mechanism of the regular structure followed the model suggested by Gibson and Ashby (Gibson and Ashby 1999) in a layer-wise manner, whereas the randomised structures showed a more localised stress concentration and therefore the local failure of struts were more isolated.

Lastly, building on Chapters 3 & 4, a novel model of the time dependant, microscopic flow-induced shear driven, bone ingrowth model was developed. The bone ingrowth as a function of time (up to 120 hrs) and shear stress was simulated in 3D on a microscopic scale for the first time and the model takes the subsequent influence of ingrowth on the flow into consideration.

- The first microscale CFD model, based on N-S equations, was developed to study time dependent bone ingrowth and flow-induced shear stress within the porous AM Ti structures. The model was applied to regular and 30% randomised structures with four different inflow velocities (0.02, 0.05, 0.1 and 0.2 mm/s).
- The range of shear stress, overall growth rate and the total amount of bone ingrowth largely depends on the inflow velocity. The growth increased from 1.8 to 4.7% at inflow velocity from 0.02 to 0.05 mm/s in both types of structures.
- At higher flow velocities, rate of ingrowth in randomised structures increased by 11% over the regular structure. It is suggested that a greater overall growth rate may occur at higher flow velocities in a randomised structure.
- Regular and 30% randomised structures showed different distributions of shear especially towards the later stage of the growth. In the regular structure, the overall growth rate dropped after about 9% of bone ingrowth at higher inflow velocities (0.1 and 0.2 mm/s). Constrictions in the interconnect regions in the regular structure were found due to the formation of high stress regions with shear greater than 1000 mPa. While in the randomised structure, the growth followed pre-designed preferential channels so that it facilitated better ingrowth at later time points. This finding indicates that the internal structure difference may be useful for designing the implants to be used in different defect places in the body where localised bone ingrowth may be required.
- The quantitative effect of excessive shear stress greater than 56 mPa predicted that higher inflow velocities, greater than those shown in experiments, can be used as guidelines for designing the optimal perfusion rates in the cell culturing study.

In summary, the thesis demonstrates that the CFD and FEA models are able to quantify the flow and mechanical properties of various Ti porous implant structures. Combining the effects of different structural factors on the performance of implant, bespoke design of the optimal implant with a combination of the regular and randomised structures may be recommended. For example, depending on the shape of the defect area, randomised structure that has better mechanical performance can be used in stress bearing location with partial volume of the regular structure with added strut roughness to enhance fast early stage bone ingrowth to fix the implant at the defect site. Furthermore, as the

porosity and the randomisation level of the structure have separate influences on the bulk and localised flow respectively, one should consider the interactive effect of altering the overall porosity and the randomisation level. To further provide a quantitative recommendation for implant design, a study combining the three models will be essential to investigate the complex interactions between loading, fluid flow and porosity changes due to ingrowth.

6.2 Future Work

In Chapter 5, the model of predicting the bone ingrowth was based solely on the shear stress induced by the flow within the structure. Further modification can be made to the microscopic model to include the nutrition and oxygen transport in order to provide more accurate results of bone ingrowth with local shear stress distribution.

Statistical analysis is recommended to further test the accuracy of the model by applying each model to more types of scaffolds such as bioglass and polymer foams.

The predicted amount of bone ingrowth from this model is recommended to be compared to *in vivo* samples with implanted foams to further confirm the finding of the study.

The three models developed in this thesis simulate the flow, bone ingrowth and the mechanical behaviour separately. Combination of the three models and study on the complex interaction of flow, mechanical properties and bone ingrowth are recommended.

7 References

TKR implant. http://www.orthopale.com/total-knee-arthroplasty.php 22/04/2013.

X-Ray microtomography. http://serc.carleton.edu/research_education/geochemsheets/techniques/CT.html 22/04/2013.

Al-Rawahi, N. and Tryggvason, G. (2002). "Numerical simulation of dendritic solidification with convection: two-dimensional geometry." J Comput Phys **180**(2): 471-496.

Alvarez, K. and Nakajima, H. (2009). "Metallic scaffolds for bone regeneration." Materials **2**(3): 790-832.

Anderson, J. D. (1995). Computational fluid dynamics, McGraw-Hill.

Andrews, E., Sanders, W. and Gibson, L. (1999). "Compressive and tensile behaviour of aluminum foams." Mat Sci Eng A-Struct **270**(2): 113-124.

Anguy, Y., Bernard, D. and Ehrlich, R. (1994). "The local change of scale method for modelling flow in natural porous media (I): Numerical tools." Adv Water Res **17**(6): 337-351.

Atwood, R. C. and Lee, P. D. (2003). "Simulation of the three-dimensional morphology of solidification porosity in an aluminium-silicon alloy." Acta Mater **51**(18): 5447-5466.

Atwood, R. C., Jones, J. R., Lee, P. D. and Hench, L. L. (2004). "Analysis of pore interconnectivity in bioactive glass foams using X-ray microtomography." Scr Mater **51**(11): 1029-1033.

Ayers, D. C., Dennis, D. A., Johanson, N. A. and Pellegrini Jr, V. D. (1997). "Common complications of total knee arthroplasty." J Bone Joint Surg **79**(2): 278-311.

Babout, L., Ludwig, W., Maire, E. and Buffiere, J. (2003). "Damage assessment in metallic structural materials using high resolution synchrotron X-ray tomography." Nucl Instrum Methods Phys Res, Sect B **200**: 303-307.

Balla, V., Bose, S. and Bandyopadhyay, A. (2010). "Understanding compressive deformation in porous titanium." Phylos Mag **90**(22): 3081-3094.

Balto, K., Muller, R., Carrington, D., Dobeck, J. and Stashenko, P. (2000). "Quantification of periapical bone destruction in mice by micro-computed tomography." J Dent Res **79**(1): 35-40.

Banhart, J. and Baumeister, J. (1998). "Deformation characteristics of metal foams." J Mater Sci **33**(6): 1431-1440.

Bauer, T. W. and Schils, J. (1999). "The pathology of total joint arthroplasty." Skeletal Radiol **28**(9): 483-497.

Bayraktar, H. H., Morgan, E. F., Niebur, G. L., Morris, G. E., Wong, E. K. and Keaveny, T. M. (2004). "Comparison of the elastic and yield properties of human femoral trabecular and cortical bone tissue." J Biomech **37**(1): 27-35.

Bear, J. (1988). Dynamics of fluids in porous media, Dover Publications.

Belteridge, W. (1982). Cobaly and its alloys, SAMPE Journal, Society for Advancement of Material and Process Engineering, P. O. Box 2459, Covina, CA 91722.

Bernard, D., Nielsen, Ø., Salvo, L. and Cloetens, P. (2005). "Permeability assessment by 3D interdendritic flow simulations on microtomography mappings of Al-Cu alloys." Mat Sci Eng A-Struct **392**(1-2): 112-120.

Bobyn, J., Stackpool, G., Hacking, S., Tanzer, M. and Krygier, J. (1999). "Characteristics of bone ingrowth and interface mechanics of a new porous tantalum biomaterial." J Bone Joint Surg Br **81**(5): 907-914.

Botchwey, E. A., Pollack, S. R., El-Amin, S., Levine, E. M., Tuan, R. S. and Laurencin, C. T. (2003). "Human osteoblast-like cells in three-dimensional culture with fluid flow." Biorheology **40**(1-3): 299-306.

Boyan, B. D., Hummert, T. W., Dean, D. D. and Schwartz, Z. (1996). "Role of material surfaces in regulating bone and cartilage cell response." Biomaterials **17**(2): 137-146.

Cahill, S., Lohfeld, S. and McHugh, P. (2009). "Finite element predictions compared to experimental results for the effective modulus of bone tissue engineering scaffolds fabricated by selective laser sintering." J Mater Sci-Mater M **20**(6): 1255-1262.

Cartmell, S. H., Porter, B. D., Garcia, A. J. and Guldberg, R. E. (2003). "Effects of medium perfusion rate on cell-seeded three-dimensional bone constructs in vitro." Tissue Eng **9**(6): 1197-1203.

Carvalho, D. C. L., Carvalho, M. M. and Cliquet Jr, A. (2001). "Disuse ostoporosis: its relationship to spine cord injuried patient rehabilitation." Acta Ortop Bras **9**(3): 34-43.

Chen, C. T., Malkus, D. S. and Vanderby Jr, R. (1998). "A fiber matrix model for interstitial fluid flow and permeability in ligaments and tendons." Biorheology **35**(2): 103-118.

Chen, Y. J., Feng, B., Zhu, Y. P., Weng, J., Wang, J. X. and Lu, X. (2009). "Fabrication of porous titanium implants with biomechanical compatibility." Mater Lett **63**(30): 2659-2661.

Chorin, A. J. (1968). "Numerical solution of the Navier-Stokes equations." Math Comp **22**(104): 745-762.

Chung, C., Chen, C., Chen, C. and Tseng, C. (2007). "Enhancement of cell growth in tissue-engineering constructs under direct perfusion: Modeling and simulation." Biotechnol Bioeng **97**(6): 1603-1616.

Chung, T. (2010). Computational fluid dynamics, Cambridge University Press.

Cioffi, M., Boschetti, F., Raimondi, M. T. and Dubini, G. (2006). "Modeling evaluation of the fluid-dynamic microenvironment in tissue-engineered constructs: A micro-CT based model." Biotechnol Bioeng **93**(3): 500-510.

Cioffi, M., Küffer, J., Ströbel, S., Dubini, G., Martin, I. and Wendt, D. (2008). "Computational evaluation of oxygen and shear stress distributions in 3D perfusion culture systems: Macro-scale and micro-structured models." J Biomech **41**(14): 2918-2925.

Coletti, F., Macchietto, S. and Elvassore, N. (2006). "Mathematical modeling of three-dimensional cell cultures in perfusion bioreactors." Ind Eng Chem Res **45**(24): 8158-8169.

Davies, G. J. and Zhen, S. (1983). "Metallic foams: their production, properties and applications." J Mater Sci **18**(7): 1899-1911.

Depalle, B., Chapurlat, R., Walter-Le-Berre, H., Bou-Saïd, B. and Follet, H. (2013). "Finite element dependence of stress evaluation for human trabecular bone." J Mech Behav Biomed **18**(0): 200-212.

Despois, J. F. and Mortensen, A. (2005). "Permeability of open-pore microcellular materials." Acta Mater **53**(5): 1381-1388.

Dillaman, R. M., Roer, R. D. and Gay, D. M. (1991). "Fluid movement in bone: theoretical and empirical." J Biomech **24**: 163-177.

Dillard, T., N'guyen, F., Maire, E., Salvo, L., Forest, S., Bienvenu, Y., Bartout, J., Croset, M., Dendievel, R. and Cloetens, P. (2005). "3D quantitative image analysis of open-cell nickel foams under tension and compression loading using X-ray microtomography." Phylos Mag **85**(19): 2147-2175.

Dixon, T., Shaw, M., Ebrahim, S. and Dieppe, P. (2004). "Trends in hip and knee joint replacement: socioeconomic inequalities and projecions of need." Ann Rheum Dis **63**: 825-830.

Dong, H. and Lee, P. (2005). "Simulation of the columnar-to-equiaxed transition in directionally solidified Al–Cu alloys." Acta Mater **53**(3): 659-668.

Duerig, T. W., Tolomeo, D. E. and Wholey, M. (2000). "An overview of superelastic stent design." Minim Invasiv Ther **9**(3): 235 - 246.

Elliott, J., Windle, A., Hobdell, J., Eeckhaut, G., Oldman, R., Ludwig, W., Boller, E., Cloetens, P., Baruchel, J. (2002). "In-situ deformation of an open-cell flexible polyurethane foam characterised by 3D computed microtomography." J Mater Sci **37**(8).

Eshraghi, S. and Das, S. (2010). "Mechanical and microstructural properties of polycaprolactone scaffolds with one-dimensional, two-dimensional, and three-dimensional orthogonally oriented porous architectures produced by selective laser sintering." Acta Biomater **6**(7): 2467-2476.

Feldkamp, L. A., Goldstein, S. A., Parfitt, M. A., Jesion, G. and Kleerekoper, M. (1989). "The direct examination of three‐dimensional bone architecture in vitro by computed tomography." J Bone Miner Res **4**(1): 3-11.

Feldkamp, L. A. D., L. C.; Kress, J. W. (1984). "Practical cone-beam algorithm." J Opt Soc Am A **1**(6).

Fourie, W., Said, R., Young, P. and Barnes, D. L. (2007). The simulation of pore scale fluid flow with real world geometries obtained from X-ray computed tomography. COMSOL Conference Boston.

Freed, L. E., Marquis, J. C., Langer, R. and Vunjak-Novakovic, G. (1994). "Kinetics of chondrocyte growth in cell-polymer implants." Biotechnol Bioeng **43**(7): 597-604.

Freed, L. E. and Vunjak-Novakovic, G. (2000). "Tissue engineering bioreactors." Principles of tissue engineering **2**: 143-156.

Freyman, T., Yannas, I. and Gibson, L. (2001). "Cellular materials as porous scaffolds for tissue engineering." Prog Mater Sci **46**(3): 273-282.

Fujibayashi, S., Neo, M., Kim, H.-M., Kokubo, T. and Nakamura, T. (2004). "Osteoinduction of porous bioactive titanium metal." Biomaterials **25**(3): 443-450.

Fukuda, A., Takemoto, M., Saito, T., Fujibayashi, S., Neo, M., Pattanayak, D. K., Matsushita, T., Sasaki, K., Nishida, N. and Kokubo, T. (2011). "Osteoinduction of porous Ti implants with a channel structure fabricated by selective laser melting." Acta Biomater **7**(5): 2327-2336.

Fuloria, D., Lee, P. D. and Bernard, D. (2008). "Microtomographic characterization of columnar Al–Cu dendrites for fluid flow and flow stress determination." Mat Sci Eng A-Struct **494**(1–2): 3-9.

Galante, J., Rostoker, W., Lueck, R. and Ray, R. D. (1971). "Sintered Fiber Metal Composites as a Basis for Attachment of Implants to Bone." J Bone Joint Surg Am **53**(1): 101-114.

Galante, J. O., Lemons, J., Spector, M., Wilson, P. D. and Wright, T. M. (1991). "The biologic effects of implant materials." J Orthopaed res **9**(5): 760-775.

Galante, J. O. and Jacobs, J. (1992). "Clinical Performances of Ingrowth Surfaces." Clin Orthop Relat R **276**: 41-49.

Geetha, M., Singh, A. K., Asokamani, R. and Gogia, A. K. (2009). "Ti based biomaterials, the ultimate choice for orthopaedic implants - A review." Prog Mater Sci **54**(3): 397-425.

Gibson, L. and Ashby, M. (1999). Cellular solids: structure and properties, Cambridge University Press.

Gibson, L. J., Ashby, M. F. and Harley, B. A. (2010). Cellular materials in nature and medicine. Cambridge, Cambridge University Press.

Gitman, I. M., Askes, H. and Sluys, L. J. (2007). "Representative volume: Existence and size determination." Eng Fract Mech **74**(16): 2518-2534.

Gorny, B., Niendorf, T., Lackmann, J., Thoene, M., Troester, T. and Maier, H. J. (2011). "In situ characterization of the deformation and failure behavior of non-stochastic porous structures processed by selective laser melting." Mat Sci Eng A-Struct **528**(27): 7962-7967.

Granger, R. A. (1995). Fluid mechanics. New York, Dover.

Greenfield, E. J. (1909). Mounting of artificial teeth. U. P. Office. **478360**.

Grimm, M. J. and Williams, J. L. (1997). "Measurements of permeability in human calcaneal trabecular bone." J Biomech **30**(7): 743-745.

Grotle, M., Hagen, K. B., Natvig, B., Dahl, F. A. and Kvien, T. K. (2008). "Prevalence and burden of osteoarthritis: results from a population survey in Norway." J Rheumatol **35**(4): 677-684.

Haddad, R., Cook, S. and Thomas, K. (1987). "Biological fixation of porous-coated implants." J Bone Joint Surg Am **69**(9): 1459.

Hara, T., Tanck, E., Homminga, J. and Huiskes, R. (2002). "The influence of microcomputed tomography threshold variations on the assessment of structural and mechanical trabecular bone properties." Bone **31**(1): 107-109.

Harris, W. H. and Sledge, C. B. (1990). "Total hip and total knee replacement." New Engl J Med **323**(11): 725-731.

Hatano, K., Inoue, H., Kojo, T., Matsunaga, T., Tsujisawa, T., Uchiyama, C. and Uchida, Y. (1999). "Effect of surface roughness on proliferation and alkaline phosphatase expression of rat calvarial cells cultured on polystyrene." Bone **25**(4): 439-445.

Head, W. C., Bauk, D. J. and Emerson, R. H. J. (1995). "Titanium As the Material of Choice for Cementless Femoral Components in Total Hip Arthroplasty." Clin Orthop Relat R **311**: 85-90.

Herman, G. T. (1995). "Image Reconstruction From Projections." Real-Time Imaging **1**(1): 3-18.

Hillsley, M. V. and Frangos, J. A. (1994). "Review: Bone tissue engineering: The role of interstitial fluid flow." Biotechnol Bioeng **43**(7): 573-581.

Holdich, R. G. (2002). Fundamentals of particle technology, Midland Information Technology and Publishing.

Hollister, S. (2005). "Porous scaffold design for tissue engineering." Nat Mater **4**(7): 518-524.

Hollister, S. J., Maddox, R. D. and Taboas, J. M. (2002). "Optimal design and fabrication of scaffolds to mimic tissue properties and satisfy biological constraints." Biomaterials **23**(20): 4095-4103.

Holtorf, H. L., Jansen, J. A. and Mikos, A. G. (2005). "Flow perfusion culture induces the osteoblastic differentiation of marrow stromal cell ‐ scaffold constructs in the absence of dexamethasone." J Biomed Mater Res Part A **72**(3): 326-334.

Homminga, J., Huiskes, R., Van Rietbergen, B., Rüegsegger, P. and Weinans, H. (2001). "Introduction and evaluation of a gray-value voxel conversion technique." J Biomech **34**(4): 513-517.

Huang, C.-H., Lee, Y.-M., Lai, J.-H., Liau, J.-J. and Cheng, C.-K. (1999). "Failure of the all-polyethylene patellar component after total knee arthroplasty." J Arthroplasty **14**(8): 940-944.

Hui, P. W., Leung, P. C. and Sher, A. (1996). "Fluid conductance of cancellous bone graft as a predictor for graft-host interface healing." J Biomech **29**(1): 123-132.

Hutmacher, D. W., Sittinger, M. and Risbud, M. V. (2004). "Scaffold-based tissue engineering: rationale for computer-aided design and solid free-form fabrication systems." Trends Biotechnol **22**(7): 354-362.

Imwinkelried, T. (2007). "Mechanical properties of open‐pore titanium foam." J Biomed Mater Res Part A **81**(4): 964-970.

Jacobs, C., Davis, B., Rieger, C., Francis, J., Saad, M. and Fyhrie, D. (1999). "The impact of boundary conditions and mesh size on the accuracy of cancellous bone tissue modulus determination using large-scale finite-element modeling." J Biomech **32**(11): 1159-1164.

Johnson, D. L., McAllister, T. N. and Frangos, J. A. (1996). "Fluid flow stimulates rapid and continuous release of nitric oxide in osteoblasts." Am J Physiol-Endoc M **271**(1): E205-E208.

Jones, A. C. and Wilcox, R. K. (2008). "Finite element analysis of the spine: Towards a framework of verification, validation and sensitivity analysis." Med Eng Phys **30**(10): 1287-1304.

Jones, A. C., Arns, C. H., Hutmacher, D. W., Milthorpe, B. K., Sheppard, A. P. and Knackstedt, M. A. (2009). "The correlation of pore morphology, interconnectivity and physical properties of 3D ceramic scaffolds with bone ingrowth." Biomaterials **30**(7): 1440-1451.

Jones, J., Atwood, R., Poologasundarampillai, G., Yue, S. and Lee, P. (2009). "Quantifying the 3D macrostructure of tissue scaffolds." J Mater Sci-Mater M **20**(2): 463-471.

Jones, J. R. and Hench, L. L. (2003). "Regeneration of trabecular bone using porous ceramics." Curr Opin Solid St M **7**(4-5): 301-307.

Jones, J. R., Ehrenfried, L. M. and Hench, L. L. (2006). "Optimising bioactive glass scaffolds for bone tissue engineering." Biomaterials **27**(7): 964-973.

Jones, J. R., Lee, P. D. and Hench, L. L. (2006). "Hierarchical porous materials for tissue engineering." Philost T Roy Soc A **364**(1838): 263-281.

Jones, J. R., Gentleman, E. and Polak, J. (2007). "Bioactive Glass Scaffolds for Bone Regeneration." Elements **3**(6): 393-399.

Jones, J. R., Poologasundarampillai, G., Atwood, R. C., Bernard, D. and Lee, P. D. (2007). "Non-destructive quantitative 3D analysis for the optimisation of tissue scaffolds." Biomaterials **28**(7): 1404-1413.

Kalisvaart, M. M., Pagnano, M. W., Trousdale, R. T., Stuart, M. J. and Hanssen, A. D. (2012). "Randomized Clinical Trial of Rotating-Platform and Fixed-Bearing Total Knee Arthroplasty: No Clinically Detectable Differences at Five Years." J Bone Joint Surg **94**(6): 481-489.

Kapur, S., Baylink, D. J. and William Lau, K. H. (2003). "Fluid flow shear stress stimulates human osteoblast proliferation and differentiation through multiple interacting and competing signal transduction pathways." Bone **32**(3): 241-251.

Khajeh, E. and Maijer, D. M. (2012). "Permeability evolution during equiaxed dendritic solidification of Al–4.5 wt% Cu." Model Simul Mater Sc **20**(3): 035004.

Kienapfel, H., Sprey, C., Wilke, A. and Griss, P. (1999). "Implant fixation by bone ingrowth." J Arthroplasty **14**(3): 355-368.

Kim, J. and Moin, P. (1985). "Application of a fractional-step method to incompressible Navier-Stokes equations." J Comput Phys **59**(2): 308-323.

Knothe Tate, M. L., Knothe, U. and Niederer, P. (1998). "Experimental elucidation of mechanical load-induced fluid flow and its potential role in bone metabolism and functional adaptation." Am J Med Sci **316**(3): 189.

Kohles, S. S., Roberts, J. B., Upton, M. L., Wilson, C. G., Bonassar, L. J. and Schlichting, A. L. (2001). "Direct perfusion measurements of cancellous bone anisotropic permeability." J Biomech **34**(9): 1197-1202.

Kokubo, T. (1996). "Formation of biologically active bone-like apatite on metals and polymers by a biomimetic process." Thermochim Acta **280**: 479-490.

Kramer, J. S., Yelin, E. H. and Epstein, W. V. (2005). "Social and economic impacts of four musculoskeletal conditions." Arthritis Rheum **26**(7): 901-907.

Krishna, B. V., Bose, S. and Bandyopadhyay, A. (2007). "Low stiffness porous Ti structures for load-bearing implants." Acta Biomater **3**(6): 997-1006.

Kufahl, R. H. and Saha, S. (1990). "A theoretical model for stress-generated fluid flow in the canaliculi-lacunae network in bone tissue." J Biomech **23**(2): 171-180.

Kuhn, J., Goldstein, S., Feldkamp, L., Goulet, R. and Jesion, G. (2005). "Evaluation of a microcomputed tomography system to study trabecular bone structure." J Orthopaed res **8**(6): 833-842.

Kurtz, S., Mowat, F., Ong, K., Chan, N., Lau, E. and Halpern, M. (2005). "Prevalence of Primary and Revision Total Hip and Knee Arthroplasty in the United States From 1990 Through 2002." J Bone Joint Surg **87**(7): 1487-1497.

Lacroix, D., Chateau, A., Ginebra, M.-P. and Planell, J. A. (2006). "Micro-finite element models of bone tissue-engineering scaffolds." Biomaterials **27**(30): 5326-5334.

Le Guéhennec, L., Soueidan, A., Layrolle, P. and Amouriq, Y. (2007). "Surface treatments of titanium dental implants for rapid osseointegration." Dent Mater **23**(7): 844-854.

Lee, K. and Goodman, S. B. (2008). "Current state and future of joint replacements in the hip and knee." Expert Rev Med Devices **5**: 383-393.

Lee, P., Atwood, R., Dashwood, R. and Nagaumi, H. (2002). "Modeling of porosity formation in direct chill cast aluminum–magnesium alloys." Mat Sci Eng A-Struct **328**(1): 213-222.

Lee, P. D., Chirazi, A., Atwood, R. and Wang, W. (2004). "Multiscale modelling of solidification microstructures, including microsegregation and microporosity, in an Al–Si–Cu alloy." Mat Sci Eng A-Struct **365**(1): 57-65.

Lefebvre, L.-P., Banhart, J. and Dunand, D. (2008). "Porous metals and metallic foams: current status and recent developments." Adv Eng Mater **10**(9): 775-787.

Leopold, S. S., Silverton, C. D., Barden, R. M. and Rosenberg, A. G. (2003). "Isolated revision of the patellar component in total knee arthroplasty." J Bone Joint Surg **85**(1): 41-47.

Lesman, A., Blinder, Y. and Levenberg, S. (2010). "Modeling of flow-induced shear stress applied on 3D cellular scaffolds: Implications for vascular tissue engineering." Biotechnol Bioeng **105**(3): 645-654.

Levine, B. (2008). "A new era in porous metals: Applications in orthopaedics." Adv Eng Mater **10**(9): 788-792.

Leyens, C. and Peters, M., Eds. (2003). Titanium and titanium alloys: Fundamentals and applications, Wiley-VCH.

Li, G., Bronk, J. T., An, K.-N. and Kelly, P. J. (1987). "Permeability of cortical bone of canine tibiae." Microvasc Res **34**(3): 302-310.

Lindquist, W. B., Venkatarangan, A., Dunsmuir, J. and Wong, T.-f. (2000). "Pore and throat size distributions measured from synchrotron X-ray tomographic images of Fontainebleau sandstones." J Geophys Res **105**.

Liu, D., Chua, C. K. and Leong, K. F. (2012). "A mathematical model for fluid shear-sensitive 3D tissue construct development." Biomech Model Mechanobiol: 1-13.

Lu, J., Flautre, B., Anselme, K., Hardouin, P., Gallur, A., Descamps, M. and Thierry, B. (1999). "Role of interconnections in porous bioceramics on bone recolonization in vitro and in vivo." J Mater Sci-Mater M **10**(2): 111-120.

Macedo, A., Vaz, C. M. P., Naime, J. M., Cruvinel, P. E. and Crestana, S. (1999). "X-ray microtomography to characterize the physical properties of soil and particulate systems." Powder Technol **101**(2): 178-182.

Maes, F., Van Ransbeeck, P., Van Oosterwyck, H. and Verdonck, P. (2009). "Modeling fluid flow through irregular scaffolds for perfusion bioreactors." Biotechnol Bioeng **103**(3): 621-630.

Maes, F., Van Baelen, B., Van Ransbeeck, P., Moesen, M., Van Oosterwyck, H. and Verdonck, P. (2010). CFD models for wallshear stress estimation; a comparitive study of two complete scaffold geometries.

Maire, E., Buffière, J. Y., Salvom, L., Blandin, J. J., Ludwig, W. and Létang, J. M. (2001). "On the application of X-ray microtomography in the field of materials science." Adv Eng Mater **3**(8): 539-546.

Maire, E., Elmoutaouakkil, A., Fazekas, A. and Salvo, L. (2003). "In situ X-ray tomography measurements of deformation in cellular solids." MRS Bull **28**(4): 284-289.

Maire, E., Fazekas, A., Salvo, L., Dendievel, R., Youssef, S., Cloetens, P. and Letang, J. M. (2003). "X-ray tomography applied to the characterization of cellular materials. Related finite element modeling problems." Compos Sci Technol **63**(16): 2431-2443.

Migliavacca, F., Petrini, L., Colombo, M., Auricchio, F. and Pietrabissa, R. (2002). "Mechanical behavior of coronary stents investigated through the finite element method." J Biomech **35**(6): 803-811.

Moazen, M., Jones, A. C., Jin, Z., Wilcox, R. K. and Tsiridis, E. (2011). "Periprosthetic fracture fixation of the femur following total hip arthroplasty: A review of biomechanical testing." Clin Biomech **26**(1): 13-22.

Moore, M. J., Jabbari, E., Ritman, E. L., Lu, L., Currier, B. L., Windebank, A. J. and Yaszemski, M. J. (2004). "Quantitative analysis of interconnectivity of porous biodegradable scaffolds with micro computed tomography." J Biomed Mater Res Part A **71**(2): 258-267.

Mullen, L., Stamp, R. C., Brooks, W. K., Jones, E. and Sutcliffe, C. J. (2009). "Selective Laser Melting: A regular unit cell approach for the manufacture of porous, titanium, bone in-growth constructs, suitable for orthopedic applications." J Biomed Mater Res Part B **89B**(2): 325-334.

Mullen, L., Stamp, R. C., Fox, P., Jones, E., Ngo, C. and Sutcliffe, C. J. (2010). "Selective laser melting: A unit cell approach for the manufacture of porous, titanium, bone in-growth constructs, suitable for orthopedic applications. II. Randomized structures." J Biomed Mater Res Part B **92B**(1): 178-188.

Müller, R., Gerber, S. and Hayes, W. (1998). "Micro-compression: a novel technique for the nondestructive assessment of local bone failure." Technol Health Care **6**(5): 433-444.

Müller, R. and Harry van Lenthe, G. (2006). "Trabecular bone failure at the microstructural level." Curr Osteoporos Rep **4**(2): 80-86.

Müller, U., Imwinkelried, T., Horst, M., Sievers, M. and Graf-Hausner, U. (2006). "Do human osteoblasts grow into open-porous titanium." Eur Cells Mater **11**: 8-15.

Müllner, H. W., Fritsch, A., Kohlhauser, C., Reihsner, R., Hellmich, C., Godlinski, D., Rota, A., Slesinski, R. and Eberhardsteiner, J. (2008). "Acoustical and poromechanical characterisation of titanium scaffolds for biomedical applications." Strain **44**(2): 153-163.

Nagaraja, S., Couse, T. L. and Guldberg, R. E. (2005). "Trabecular bone microdamage and microstructural stresses under uniaxial compression." J Biomech **38**(4): 707-716.

Nagelhout, D., Bhat, M. S., Heinrich, J. C. and Poirier, D. R. (1995). "Permeability for flow normal to a sparse array of fibres." Mat Sci Eng A-Struct **191**(1-2): 203-208.

Nauman, E. A., Fong, K. E. and Keaveny, T. M. (1999). "Dependence of intertrabecular permeability on flow direction and anatomic site." Ann Biomed Eng **27**(4): 517-524.

Niebur, G., Feldstein, M., Yuen, J., Chen, T. and Keaveny, T. (2000). "High-resolution finite element models with tissue strength asymmetry accurately predict failure of trabecular bone." J Biomech **33**(12): 1575-1583.

Niinomi, M. (2003). "Recent research and development in titanium alloys for biomedical applications and healthcare goods." Sci Tech Adv Mater **4**(5): 445-454.

Ochoa, I., Sanz-Herrera, J. A., Garcia-Aznar, J. M., Doblare, M., Yunos, D. M. and Boccaccini, A. R. (2009). "Permeability evaluation of 45S5 Bioglass-based scaffolds for bone tissue engineering." J Biomech **42**(3): 257-260.

Ochoa, I., Sanz-Herrera, J. A., García-Aznar, J. M., Doblaré, M., Yunos, D. M. and Boccaccini, A. R. (2009). "Permeability evaluation of 45S5 Bioglass® based scaffolds for bone tissue engineering." J Biomech **42**(3): 257-260.

Oh, I.-H., Nomura, N., Masahashi, N. and Hanada, S. (2003). "Mechanical properties of porous titanium compacts prepared by powder sintering." Scr Mater **49**(12): 1197-1202.

Ohgaki, T., Toda, H., Kobayashi, M., Uesugi, K., Niinomi, M., Akahori, T., Kobayash, T., Makii, K. and Aruga, Y. (2006). "In situ observations of compressive behaviour of aluminium foams by local tomography using high-resolution X-rays." Phylos Mag **86**(28): 4417-4438.

Okii, N., Nishimura, S., Kurisu, K., Takeshima, Y. and Uozumi, T. (2001). "In vivo histological changes occurring in hydroxyapatite cranial reconstruction -Case Report-." Neurol Med-chir **41**(2): 100-104.

Otsuki, B., Takemoto, M., Fujibayashi, S., Neo, M., Kokubo, T. and Nakamura, T. (2006). "Pore throat size and connectivity determine bone and tissue ingrowth into porous implants:

Three-dimensional micro-CT based structural analyses of porous bioactive titanium implants." Biomaterials **27**(35): 5892-5900.

Owan, I., Burr, D. B., Turner, C. H., Qiu, J., Tu, Y., Onyia, J. E. and Duncan, R. L. (1997). "Mechanotransduction in bone: osteoblasts are more responsive to fluid forces than mechanical strain." Am J Physiol-Cell Ph **273**(3): C810-C815.

Papathanasiou, T. D. and Lee, P. D. (1997). "Morphological effects on the transverse permeability of arrays of aligned fibers." Polym Composite **18**(2): 242-253.

Park, J. and Bronzino, J. (2003). Biomaterials: principles and applications, CRC press Boca Raton, FL.

Parker, D. A., Dunbar, M. J. and Rorabeck, C. H. (2003). "Extensor mechanism failure associated with total knee arthroplasty: prevention and management." J Am Acad Orthop Surg **11**(4): 238-247.

Patankar, S. (1980). Numerical Heat Transfer and Fluid Flow. Hemisphere, New York, Taylor & Francis.

Pelissier, P., Villars, F., Mathoulin-Pelissier, S., Bareille, R., Lafage-Proust, M.-H. and Vilamitjana-Amedee, J. (2003). "Influences of vascularization and osteogenic cells on heterotopic bone formation within a madreporic ceramic in rats." Plast Reconstr Surg **111**(6): 1932-1941

Piekarski, K. (1977). "Transport mechanism operating between blood supply and osteocytes in long bones." Nature **269**: 80-82.

Pilliar, R. (1987). "Porous-surfaced metallic implants for orthopedic applications." J Biomed Mater Res **21**(A1 Suppl): 1.

Pilliar, R. M., Cameron, H. U., Welsh, R. P. and Binnington, A. G. (1981). "Radiographic and morphologic studies of load-bearing porous-surfaced structured implants." Clin Orthop Relat R **156**: 249-257.

Pilliar, R. M. (1983). "Powder metal-made orthopedic implants with porous surface for fixation by tissue ingrowth." Clin Orthop Relat R **176**: 42-51.

Porter, B., Zauel, R., Stockman, H., Guldberg, R. and Fyhrie, D. (2005). "3-D computational modeling of media flow through scaffolds in a perfusion bioreactor." J Biomech **38**(3): 543-549.

Poss, R., Walker, P., Spector, M., Reilly, D. T., Robertson, D. D. and Sledge, C. B. (1988). "Strategies for improving fixation of femoral components in total hip arthroplasty." Clin Orthop Relat R **235**: 181-194.

Raimondi, M., Boschetti, F., Falcone, L., Fiore, G., Remuzzi, A., Marinoni, E., Marazzi, M. and Pietrabissa, R. (2002). "Mechanobiology of engineered cartilage cultured under a quantified fluid-dynamic environment." Biomech Model Mechanobiol **1**(1): 69-82.

Raimondi, M., Boschetti, F., Migliavacca, F., Cioffi, M. and Dubini, G. (2005). "Micro fluid dynamics in three-dimensional engineered cell systems in bioreactors." Topics In Tissue Engineering **2**.

Raimondi, M., Causin, P., Mara, A., Nava, M., Laganà, M. and Sacco, R. (2011). "Breakthroughs in computational modeling of cartilage regeneration in perfused bioreactors." IEEE T Bio-med Eng(99): 1-1.

Raimondi, M. T., Boschetti, F., Falcone, L., Migliavacca, F., Remuzzi, A. and Dubini, G. (2004). "The effect of media perfusion on three-dimensional cultures of human chondrocytes: integration of experimental and computational approaches." Biorheology **41**(3-4): 401-410.

Raimondi, M. T., Moretti, M., Cioffi, M., Giordano, C., Boschetti, F., Laganà, K. and Pietrabissa, R. (2006). "The effect of hydrodynamic shear on 3D engineered chondrocyte systems subject to direct perfusion." Biorheology **43**(3): 215-222.

Reich, K. M., Gay, C. V. and Frangos, J. A. (1990). "Fluid shear stress as a mediator of osteoblast cyclic adenosine monophosphate production." J Cell Physiol **143**(1): 100-104.

Rho, J. Y., Ashman, R. B. and Turner, C. H. (1993). "Young's modulus of trabecular and cortical bone material: ultrasonic and microtensile measurements." J Biomech **26**(2): 111-119.

Röntgen, W. (1895). "Über eine neue art von strahlen." Sitzungsberichte der Physikalisch-Medicinisch Gesellschaft zu Würzburg: 132-141.

Ryan, G., Pandit, A. and Apatsidis, D. P. (2006). "Fabrication methods of porous metals for use in orthopaedic applications." Biomaterials **27**(13): 2651-2670.

Ryan, G., McGarry, P., Pandit, A. and Apatsidis, D. (2009). "Analysis of the mechanical behavior of a titanium scaffold with a repeating unit-cell substructure." J Biomed Mater Res Part B **90B**(2): 894-906.

Ryan, G. E., Pandit, A. S. and Apatsidis, D. P. (2008). "Porous titanium scaffolds fabricated using a rapid prototyping and powder metallurgy technique." Biomaterials **29**(27): 3625-3635.

Sahimi, M. (1995). Flows in porous media and fractured rock: From classical models to modern approaches. New York, Wiley.

Schmalzried, T. P. and Callaghan, J. J. (1999). "Current concepts review - Wear in total hip and knee replacements." J Bone Joint Surg Am **81**(1): 115-136.

Sharkey, P. F., Hozack, W. J., Rothman, R. H., Shastri, S. and Jacoby, S. M. (2002). "Why are total knee arthroplasties failing today?" Clin Orthop Relat R **404**: 7-13.

Shimko, D. A., Shimko, V. F., Sander, E. A., Dickson, K. F. and Nauman, E. A. (2005). "Effect of porosity on the fluid flow characteristics and mechanical properties of tantalum scaffolds." J Biomed Mater Res B Appl Biomater **73**(2): 315-324.

Sikavitsas, V. I., Bancroft, G. N., Holtorf, H. L., Jansen, J. A. and Mikos, A. G. (2003). "Mineralized matrix deposition by marrow stromal osteoblasts in 3D perfusion culture increases with increasing fluid shear forces." P Natl Acad Sci USA **100**(25): 14683.

Simmons, D. J. (1979). Skeletal research: an experimental approach, Academic Press.

Singh, R., Lee, P. D., Lindley, T. C., Dashwood, R. J., Ferrie, E. and Imwinkelried, T. (2009). "Characterization of the structure and permeability of titanium foams for spinal fusion devices." Acta Biomater **5**(1): 477-487.

Singh, R., Lee, P., Lindley, T., Kohlhauser, C., Hellmich, C., Bram, M., Imwinkelried, T. and Dashwood, R. (2010). "Characterization of the deformation behavior of intermediate porosity interconnected Ti foams using micro-computed tomography and direct finite element modeling." Acta Biomater **6**(6): 2342-2351.

Singh, R., Lee, P. D., Dashwood, R. J. and Lindley, T. C. (2010). "Titanium foams for biomedical applications: a review." Mater Technol **25**: 127-136.

Solheim, E., Pinholt, E. M., Talsnes, O., Larsen, T. B. and Kirkeby, O. J. (2001). "The Relationship between Revascularisation and Osteogenesis in Fresh or Demineralised Bone Grafts." Eur Surg Res **33**(1): 42-46.

Spoerke, E. D., Murray, N. G., Li, H., Brinson, L. C., Dunand, D. C. and Stupp, S. I. (2005). "A bioactive titanium foam scaffold for bone repair." Acta Biomater **1**(5): 523-533.

Spriggs, R. M. (1961). "Expression for Effect of Porosity on Elastic Modulus of Polycrystalline Refractory Materials, Particularly Aluminum Oxide." J Am Ceram Soc **44**(12): 628-629.

Stauber, M. and Muller, R., Eds. (2008). Osteoporosis: Methods and protocols. Method Mol Cell Biol, Humana Press, Totowa, NJ.

Stock, S. R. (1999). "X-ray microtomography of materials." Int Mater Rev **44**: 141-164.

Sumner, D., Turner, T., Igloria, R., Urban, R. and Galante, J. (1998). "Functional adaptation and ingrowth of bone vary as a function of hip implant stiffness." J Biomech **31**(10): 909-917.

Tannehill, J., Anderson, D. and Pletcher, R. (1997). Computational fluid mechanics and heat transfer, Taylor & Francis Group.

Thelen, S., Barthelat, F. and Brinson, L. C. (2004). "Mechanics considerations for microporous titanium as an orthopedic implant material." J Biomed Mater Res Part A **69A**(4): 601-610.

Thurner, P., Wyss, P., Voide, R., Stauber, M., Stampanoni, M., Sennhauser, U. and Müller, R. (2006). "Time-lapsed investigation of three-dimensional failure and damage accumulation in trabecular bone using synchrotron light." Bone **39**(2): 289-299.

Ulrich, D., Van Rietbergen, B., Weinans, H. and Rüegsegger, P. (1998). "Finite element analysis of trabecular bone structure: a comparison of image-based meshing techniques." J Biomech **31**(12): 1187-1192.

Van de Casteele, E., Van Dyck, D., Sijbers, J. and Raman, E. (2002). "An energy-based beam hardening model in tomography." Phys Med Biol **47**(23): 4181.

Van Grieken, R. and Markowicz, A. (2001). Handbook of X-ray Spectrometry. New York, CRC Press.

Van Manen, M. D., Nace, J. and Mont, M. A. (2012). "Management of primary knee osteoarthritis and indications for total knee arthroplasty for general practitioners." J Am Osteopath Assoc **112**(11): 709-715.

Vezeridis, P. S., Semeins, C. M., Chen, Q. and Klein-Nulend, J. (2006). "Osteocytes subjected to pulsating fluid flow regulate osteoblast proliferation and differentiation." Biochem Bioph Res Co **348**(3): 1082-1088.

Walker, P. S., Hirano, S. K., Zhou, X. M., Granholm, J. W. and Poss, R. (1988). "Improving the fit of press-fit hip stems." Clin Orthop Relat R **228**: 134-140.

Walker, P. S. and Robertson, D. D. (1988). "Design and fabrication of cementless hip stems." Clin Orthop Relat R **235**: 25-34.

Wang, H., Pieper, J., Péters, F., Blitterswijk, C. A. v. and Lamme, E. N. (2005). "Synthetic scaffold morphology controls human dermal connective tissue formation." J Biomed Mater Res Part A **74A**(4): 523-532.

Wang, W., Lee, P. and McLean, M. (2003). "A model of solidification microstructures in nickel-based superalloys: predicting primary dendrite spacing selection." Acta Mater **51**(10): 2971-2987.

Wang, Y., Shen, Y., Wang, Z., Yang, J., Liu, N. and Huang, W. (2010). "Development of highly porous titanium scaffolds by selective laser melting." Mater Lett **64**(6): 674-676.

Warnke, P. H., Douglas, T., Wollny, P., Sherry, E., Steiner, M., Galonska, S., Becker, S. T., Springer, I. N., Wiltfang, J. and Sivananthan, S. (2008). "Rapid prototyping: porous titanium alloy scaffolds produced by selective laser melting for bone tissue engineering." Tissue Eng - Part C **15**(2): 115-124.

Wehmöller, M., Warnke, P., Zilian, C. and Eufinger, H. (2005). Implant design and production—a new approach by selective laser melting. International Congress Series, Elsevier.

Weinbaum, S., Cowin, S. and Zeng, Y. (1994). "A model for the excitation of osteocytes by mechanical loading-induced bone fluid shear stresses." J Biomech **27**(3): 339-360.

Wen, C., Mabuchi, M., Yamada, Y., Shimojima, K., Chino, Y. and Asahina, T. (2001). "Processing of biocompatible porous Ti and Mg." Scr Mater **45**(10): 1147-1153.

Wen, C. E., Yamada, Y., Shimojima, K., Chino, Y., Hosokawa, H. and Mabuchi, M. (2002). "Novel titanium foam for bone tissue engineering." J Mater Res **17**(10): 2633-2639.

Wolff, J. (1892). The law of bone remodeling. New York, Springer-Verlag.

Wolfram, S. (1986). "Theory and applications of cellular automata."

Wolfram, S. (1998). Cellular automata as models of complexity, World Scientific Publishing Co. Pte. Ltd.

Woods, J. K., Spelt, P. D. M., Lee, P. D., Selerland, T. and Lawrence, C. J. (2003). "Creeping flows of power-law fluids through periodic arrays of elliptical cylinders." J Non-Newtonian Fluid Mech **111**(2-3): 211-228.

Wray, J. B. and Lynch, C. J. (1959). "The vascular response to fracture of the tibia in the rat." J Bone Joint Surg **41**(6): 1143-1148.

Xu, C., Chu, X. and Wu, H. (2007). "Effects of patellar resurfacing on contact area and contact stress in total knee arthroplasty." The Knee **14**(3): 183-187.

Xue, W., Krishna, B. V., Bandyopadhyay, A. and Bose, S. (2007). "Processing and biocompatibility evaluation of laser processed porous titanium." Acta Biomater **3**(6): 1007-1018.

Yang, S., Leong, K.-F., Du, Z. and Chua, C.-K. (2001). "The design of scaffolds for use in tissue engineering. Part I. Traditional factors." Tissue Eng **7**(6): 679-689.

Yeni, Y. N., Christopherson, G. T., Neil Dong, X., Kim, D.-G. and Fyhrie, D. P. (2005). "Effect of microcomputed tomography voxel size on the finite element model accuracy for human cancellous bone." J Biomech Eng **127**(1): 1-8.

Yuan, L., Lee, P. D., Djambazov, G. and Pericleous, K. (2009). "Numerical simulation of the effect of fluid flow on solute distribution and dendritic morphology." Int J Cast Metal Res **22**(1-2): 204-207.

Yuan, L. and Lee, P. D. (2010). "Dendritic solidification under natural and forced convection in binary alloys: 2D versus 3D simulation." Model Simul Mater Sc **18**(5): 055008.

Yuan, L. and Lee, P. D. (2012). "A new mechanism for freckle initiation based on microstructural level simulation." Acta Mater **60**(12): 4917-4926.

Yue, S. (2011). Non-destructive quantification of tissue scaffolds and augmentation implants using X-ray microtomography. Materials. London, Imperial College London. **Doctor of Philosophy:** 126.

Yue, S., Lee, P. D., Poologasundarampillai, G. and Jones, J. R. (2011). "Evaluation of 3-D bioactive glass scaffolds dissolution in a perfusion flow system with X-ray microtomography." Acta Biomater **7**(6): 2637-2643.

Zhang, E. and Wang, B. (2005). "On the compressive behaviour of sintered porous coppers with low to medium porosities—Part I: Experimental study." Int J Mech Sci **47**(4–5): 744-756.

Zhang, Z., Jones, D., Yue, S., Lee, P. D., Jones, J. R., Sutcliffe, C. J. and Jones, E. (2013). "Hierarchical tailoring of strut architecture to control permeability of additive manufactured titanium implants." Mat Sci Eng C.

Ziółkowska, I. and Ziółkowski, D. (1988). "Fluid flow inside packed beds." Chem Eng Process **23**(3): 137-164.